From the holdings of the Department of Special Collections , Princeton University Library, Princeton, NJ

These documents are either in the public domain, or can only be used for educational and research purposes (Fair use) as per U.S. Copyright law (text below). By accessing this file, all users agree that their use falls in the public domain or within fair use as defined by the copyrightlaw. We do not charge any permission or usage fees for the publication of images of material inour collections, including those provided by Princeton University Library, via our website, catalog, or directly from staff.For more information regarding copyright, credit, and citation please review the information onthe Copyright, Credit and Citation Guidelines page of our website.
https://library.princeton.edu/special-collections/policies/copyright-credit-and-citation-guidelines. If you have any questions, including how to order higher-quality images from the collection, contact Special Collections Public Services via our Ask Us! Form. https://library.princeton.edu/special-collections/ask-us

---

Doctoral Dissertations, 2011-2026 Atmospheric and Oceanic Sciences

2011

Processes controlling the distribution of biogeochemical tracers in the ocean

Bianchi, Daniele

Princeton, NJ : Princeton University

---

http://arks.princeton.edu/ark:/88435/dsp018049g507g

U.S. Copyright law: The copyright law of the United States (Title 17, §108, United States Code) governs the making of photocopies or other reproductions of copyrighted material. Under certain conditions specified in the law, libraries and archives are authorized to furnish a photocopy or other reproduction. One of these specified conditions is that the photocopy or reproduction is not to be used for any purpose other than private study, scholarship, or research. If a user makes a request for, or later uses, a photocopy or reproduction for purposes in excess of fair use that user may be liable for copyright infringement. This institution reserves the right to refuse to accept a copying order if, in its judgment, fulfillment of the order would involve a violation of copyright law. https://www.copyright.gov/title17/title17.pdf

PROCESSES CONTROLLING THE DISTRIBUTION OF BIOGEOCHEMICAL TRACERS IN THE OCEAN

DANIELE BIANCHI

A DISSERTATION

PRESENTED TO THE FACULTY

OF PRINCETON UNIVERSITY

IN CANDIDACY FOR THE DEGREE

OF DOCTOR OF PHILOSOPHY

RECOMMENDED FOR ACCEPTANCE

BY THE PROGRAM IN

ATMOSPHERIC AND OCEANIC SCIENCES

ADVISER: JORGE L. SARMIENTO

NOVEMBER 2011

© Copyright by Daniele Bianchi, 2011.

All Rights Reserved

Abstract

This thesis investigates the mechanisms controlling ocean biogeochemical tracers, including ocean circulation, nutrient and carbon cycles, and the marine ecosystem.

In Chapter 2, I focus on the distribution of helium isotopes in the ocean. The high $^{3}He/^{4}He$ ratio of oceanic helium relative to the atmosphere is a signature of mantle ^{3}He outgassing from the Earth's interior. This flux is commonly used to estimates chemical fluxes of elements from the solid Earth, and to constrain models of mantle dynamics. Here, I use a suite of ocean general circulation models and helium isotope data from the World Ocean Circulation Experiment to revise the flux of helium from the mantle to the oceans. I show that a flux of 527±102 mol $year^{-1}$, approximately 2 times smaller than previous estimates, is required to match observed helium in ocean general circulation models calibrated against observations of ventilation tracers. This new estimate calls for a revision of the element fluxes that are currently linked to helium outgassing, including noble gases and carbon dioxide.

In Chapter 3, I investigate the distribution and biogeochemical processes that characterize open ocean Oxygen Minimum Zones (OMZs). OMZs are major sites of fixed nitrogen removal from the ocean, and a net source of nitrous oxide, a powerful greenhouse gas. First, I provide a revised estimate of OMZ distribution based on analysis and synthesis of in situ measurements. The resulting suboxic volumes (O_2<5-10 $mmol\ m^{-3}$) are a factor 3 larger than commonly used datasets. Second, I combine the new oxygen data sets with estimates of global export and simple models of remineralization to estimate global denitrification and N_2O production. The results (1) reconcile water

column denitrification rates with existing estimates based on nitrogen isotopes, (2) revise previous estimates of sediment denitrification down by 1/3, and (3) independently support a historically-balanced oceanic nitrogen cycle. I explore the sensitivity of the estimates to the model parameters and quantify the effects of ocean deoxygenation, an expected response to anthropogenic climate change.

In Chapter 4, I investigate the controls and impacts of diel vertical migration (DVM) of zooplankton and fish on water column ecosystem and biogeochemistry. DVM is a fundamental component of the biological pump, but is generally overlooked in global models of the Earth System. I develop a representation of DVM in a size-structured NPZD model and evaluate it against data from three major biomes in the Pacific Ocean. The model includes: (1) a realistic parameterization of migration dynamics, (2) a representation of the processes that decouple zooplankton feeding and respiration in the water column, and (3) a consistent parameterization of visual predation. The model captures to first order the biomass and nutrient flux partitioning between different trophic levels, and the proportion of migrating zooplankton. I show that realistic migratory populations sustain active fluxes of between 20 and 40 % of the particle export to the mesopelagic zone, and contribute up to 50 % of the total respiration within the layers affected by migration. This has consequences for oxygen, nutrient, and carbon cycling. I highlight the importance of allowing zooplankton feeding and excretion to vary independently with depth – a process that should be included in global parameterizations of DVM.

Acknowledgements

Being part of Jorge Sarmiento's group for the duration of my PhD was an incredible privilege. I am thankful to Jorge for granting me total support and freedom to pursue my scientific interests, for generously sharing ideas, and for the constant encouragement to push my own boundaries. I greatly enjoyed discussions with Jorge on oceanography and science, on politics, travel and food, and I will miss being part of his group.

I thank Anand Gnanadesikan for his encouragement and guidance both at the beginning and throughout the course of my PhD. His advise and insights have been invaluable in shaping my research.

These years at Princeton I had the luck of working closely to many great scientists, from whom I learned more than I could imagine. John Dunne and Charlie Stock generously shared models and data, helped with numerous and insightful discussions, and carefully read my manuscripts. I am grateful to the AOS faculty and to the GFDL scientists for their mentoring and dedication.

Many of the researchers and post-docs in Jorge's group became good friends throughout the years. I will especially miss working two doors away from Keith Rodgers, the innumerable discussions with him on science and life, the anti-conformist views, and the escapades to Coney Island. I look forward to working closely with Eric Galbraith, who taught me not be afraid of exploring uncharted territories.

Big thanks go to Bob Key for his patience in guiding me through the subtleties of ocean measurements, and to Rick Slater for helping me find a way through the intricacy of the models' code.

Many friends made my stay in Princeton extremely enjoyable. I especially thank my fellow graduate students, Yves, Kelly, Joe, Arno, Yuanyuan, for being helpful friends and office mates, and for sharing the joys and pains of graduate student life. Claudie, Allison, Thomas, Stephanie, Jaime, Sarah, Jennifer, Rym, Antoine, and many other friends contributed to make Sayre Hall a cheerful and fun place to work in. Last but not least my thanks go to Anna and Laura for their unlimited patience and help, and for cheering me up in the most stressful moments.

And outside of Princeton, my thoughts go to all the friends that I shared these years with… Marco, Sandrine, Adrian, Matthew, Alma, Orlando, Lee, and across the Atlantic, the old crew, Fra, Marghe, Corra, Teo, Paola, Filo, Marco, Laura, Albert, Mireia, Matte, Marchio, Caprix, Cicciuz. Thanks to all of you.

I dedicate this thesis to my parents, from whom I learned to love nature and the sea, and who encouraged me to follow this wonderful journey.

Table of Contents

Abstract ii

Acknowledgements iv

Table of Contents vi

List of Tables ix

List of Figures xii

CHAPTER 1: INTRODUCTION 1

1.1 Motivation 1
1.2 The meridional overturning circulation and the return path of dense waters 2
1.2.1 Helium-3 as a tracer of deep waters and its geochemical importance 3

1.3 Oxygen minimum zones and biogeochemical controls on the biological pump 5
1.3.1 Global distribution of OMZs and their impact on the nitrogen cycle 7

1.3.2 Diel vertical migration impacts on water column biogeochemistry and ecosystem 7

1.4 References 10

CHAPTER 2: LOW HELIUM FLUX FROM THE MANTLE INFERRED FROM SIMULATIONS OF OCEANIC HELIUM ISOTOPE DATA 16

2.1 Introduction 17
2.1.1 Geochemical importance of helium injection into the oceans 17

2.1.2 Estimates of helium injection 18

2.1.3 Previous modeling studies based on general circulation models 21

2.1.4 Outline of the chapter 21

2.2 Methods 22
2.2.1 Observations of mantle helium in the ocean 22

2.2.2 Models of helium isotpe distribution in the ocean 25

2.3 Results and discussion 28
2.4 Conclusions 31
2.5 References 34

CHAPTER 3: 47

CHAPTER 3: DATA-BASED ESTIMATES OF SUBOXIA, DENITRIFICATION AND N_2O PRODUCTION IN THE OCEAN, AND THEIR SENSITIVITIES TO CHANGE 47

3.1 Introduction 49
3.2 Data sets used in this study 52
3.3 Models of respiration, denitrification and N_2O production 58
3.4 Results 63
3.4.1 Global and regional estimates 63

3.4.2 Sensitivity and error estimates 67

3.4.3 Sensitivity to the oxygen state of the ocean 69

3.5 Discussion and conclusions 71
3.6 References 74

CHAPTER 4: ZOOPLANKTON DIEL VERTICAL MIGRATION: CONTROLS AND BIOGEOCHEMICAL IMPACTS IN AN OCEAN ECOSYSTEM MODEL 94

4.1 Introduction 96
4.1.1 Proximate and ultimate controls on DVM 96

4.1.2 DVM occurrence and patterns 97

4.1.3 Large-scale impacts of DVM 99

4.1.4 Modeling studies 102

4.1.5 Objectives and outline of the chapter 102

4.2 Modeling framework 103

4.2.1 Ecosystem model 104

4.2.2 Diel vertical migration model 105

4.2.3 Zooplankton internal pool dynamics and costs of swimming 107

4.2.4 Visual predation 111

4.3 Model set-up 115
4.3.1 One-dimensional model implementation 116

4.3.2 Overview of the study sites 117

4.4 Model results 119
4.4.1 Water column physics and general ecosystem properties 119

4.4.2 DVM patterns 121

4.4.3 Sensitivity of DVM to the model parameters 121

4.4.4 Biogeochemical impacts of DVM 123

4.5 Discussion and conclusions 127
4.6 References 131

List of Tables

Table 2.1 : Estimates based on analysis of observations and model results for mean $\Delta^{14}C$ in the North Pacific Deep Water, Indian Deep Water and gradients with Circumpolar Deep Waters; CFC-11 inventory in the deep Southern Ocean, inventory of mantle ^{3}He in the deep ocean, and ratio between the mantle ^{3}He inventory in the models and in the observational estimate. See Section 2.3 for a discussion 40

Table 3.1: Estimates of oceanic nitrogen budgets ($Tg\,N\,year^{-1}$) 82

Table 3.2: Volume ($10^{6}\ km^{3}$) of suboxic waters for the major OMZs in the Indian and Pacific Oceans for two oxygen limits (20 and 5 $mmol\,m^{-3}$). The data sets shown are: gridded WOA05; GLODAP data mapped using the procedure described in Gandin (1963); GLODAP data mapped using the procedure described in Barnes (1994); gridded WOA05 with an empirical linear correction based on GLODAP in situ measurements..... 83

Table 3.3: Regional and global estimates of POC flux to the sediments, pelagic denitrification, benthic denitrification (shelf values for z<150 m in parentheses) and N_2O production. Results are averages obtained by using three oxygen data sets discussed in Section 3.2. Errors were estimated with a Monte Carlo approach as described in Section 3.4..... 84

Table 3.4: Sensitivity of the globally integrated pelagic respiration, denitrification and N_2O production to the remineralization model parameters. Results are averages obtained by using the three oxygen data sets described in Section 3.2. 85

Table 4.1: Parameters controlling the processes associated with DVM in the model. See sections 4.2.2, 4.2.3 and 4.2.4 for details. 141

Table 4.2: Ecosystem diagnostics for the three model implementation sites. For each site the first column shows observational values, the second column model results. The variables shown are: Z_{EUPH}=euphotic zone depth, NPP=net primary production, CHL=chlorophyll, SP+LP=total phytoplankton biomass, LP:SP+LP=fraction of large phytoplankton, C:CHL=Carbon to chlorophyll ratio, SZ=microzooplankton biomass, LZ+LMZ=mesozooplankton biomass, LMZ:LZ+LMZ=fraction of diel vertical migrating mesozooplantkon, POC FLUX=particulate organic carbon export from the euphotic zone, PE-RATIO=ratio between POC export and NPP at the base of the euphotic zone. Values are integral over the euphotic zone. 142

Table 4.3: Net primary production (NPP), net community production (NCP), POC flux from the euphotic zone, export due to DVM, export due to other processes, *e-ratio* (NCP/NPP), *pe-ratio* (POC FLUX/NPP), *dvm-ratio* (DVM flux/NPP) and *dom-ratio* (Non-sinking biomass export/NPP). Units for production and fluxes are $mmol C\, m^{-2} d^{-1}$. 145

Table 4.4: Ratio between DVM and POC exports at 150 m depth. 1st row: model without the internal pool dynamics; 2nd row: model with gut pool dynamics only;

3d row: model with metabolic pool dynamics only; 4th row: model with both gut and metabolic pool dynamics; 5th row: model with both gut and metabolic pool dynamics and with migrating zooplankton fraction forced to match observations (see Table 1). 146

List of Figures

Figure 2.1: Observational dataset. (a) δ^3He at 2500 m depth from objective analysis of observations. Coloured circles are observed profiles interpolated to 2500 m depth. Units are percent. The white-hatched region indicates water masses with CFC-11 concentration higher than 0.1 pmol kg^{-1} from the GLODAP dateset (Key et al., 2004), indicating potential contamination due to tritiogenic ^{3}He (b) Vertical column inventories of non-atmospheric ^{3}He for depths greater than 1000 m. Units are nmol m^{-2}. 41

Figure 2.2: Schematic representation of the deep-water circulation for observational estimates and models. In each panel the upper cell (red) shows the maximum NADW overturning between 45°N and 48°N and deep to surface water conversion inside and outside the Southern Ocean at 30°S. The lower cell (blue) shows the dense water export from the Southern Ocean at 30°S. Layer boundaries are approximately 1200 m and 3000 m depth, corresponding to approximately 27.4 σ_θ and 45.86 σ_4 potential densities. Units are Sv ($1\,\mathrm{Sv} = 10^6\,\mathrm{m^3 s^{-1}}$). (a-c) Observationally based estimates. T2008 is the inverse estimate of hydrographic data from Talley (2008); LS2007 is the inverse estimate of hydrographic data from Lumpkin and Speer (2007); F2009 is the ocean state estimate from GCM assimilation of altimetry data, satellite SST and ARGO profiles from Forget (2009). (d-f) Models: HH, P2 and P2A. See section 2.2 for details on the models. 42

Figure 2.3: Scatter-plot of mantle ^{3}He (pmol m^{-3}) versus $\Delta^{14}C$ (permil) for the deep ocean. Black dots are observations, red squares, green triangles and blue triangles are HH, P2A and P2 models respectively. The dark shading highlights the envelope of observations. Each dot represents a large-scale average over a 20° by 20° region. Depths greater than 1000 m and water masses with observed CFC-11 concentration higher than 0.1 pmol kg^{-1} have been excluded to avoid potential contamination with tritiogenic ^{3}He. (a) Models with a helium injection of 1070 mol $years^{-1}$. (b) Models with helium injection reduced to match the observed deep ocean ^{3}He inventory.The ^{3}He injection is 599, 509 and 473 mol $years^{-1}$ for the HH, P2A and P2 models respectively. 43

Figure 2.4: $\delta^{3}He$ at 2500 m depth. Units are percent. (a) Observational dataset. Colored circles are observed profiles interpolated to 2500 m depth. (b-d) HH, P2A and P2 models with ^{3}He injection reduced to match the observed deep ocean ^{3}He inventory. The ^{3}He injection is 599, 509 and 473 mol $years^{-1}$ for the HH, P2A and P2 models respectively. The white-hatched region indicates water masses with CFC-11 concentration higher than 0.1 pmol kg^{-1} from the GLODAP dateset (Key et al., 2004), indicating potential contamination due to tritiogenic ^{3}He. The reduced zonal propagation of the ^{3}He signal in the Pacific Ocean for the models in (b-d) is discussed in section 2.3. Meridional sections for the Pacific Ocean indicating zonal compensation of the ^{3}He signal are shown in Figure 2.6. 44

Figure 2.5: Vertical column inventories for non atmospheric ^{3}He for depths greater than 1000 m. Units are nmol/m^{2}. (a) observational estimate. (b-d) HH, P2A and

P2 models. Model injection of ^{3}He has been reduced to match the observed deep ocean ^{3}He inventory. The ^{3}He injection is 599, 509 and 473 mol years^{-1} for the HH, P2A and P2 models respectively..... 45

Figure 2.6: Meridional sections of δ^3He distribution (%) in the Pacific Ocean (averaged between 140°E to 80°W). Units are percent. (a) observational dataset. (b-d) HH, P2A and P2 models with ^{3}He injection reduced to match the observed deep ocean ^{3}He inventory. The ^{3}He injection is 599, 509 and 473 mol years^{-1} for the HH, P2A and P2 models respectively. The white-hatched region indicates water masses with CFC-11 concentration higher than 0.1 pmol kg^{-1}, indicating potential contamination due to tritiogenic ^{3}He. The light blue line is the contour line for CFC-11 concentration of 0.1 pmol kg^{-1} from the GLODAP dateset (Key et al., 2004)..... 46

Figure 3.1: Scatter plot of in situ GLODAP vs. gridded oxygen data. The gridded data sets were sampled at the location and month of in situ measurements by using linear interpolation. Only values below 20 $\mathrm{mmol\,m^{-3}}$ are shown. The red line is the 1:1 line. The statistics shown are means and standard deviations of the oxygen biases (gridded minus in situ oxygen) in the hypoxic range ($O_2 < 60\ \mathrm{mmol\,m^{-3}}$), and f is the fraction of data points that fall above the 1:1 line (biases > 0). The data sets shown are: (a) WOA05; (b) objective analysis of GLODAP measurements following the mapping scheme by Gandin (1963); (c) objective analysis of GLODAP measurements following the mapping scheme by

Barnes (1964); (d) WOA05 with linear correction based on in situ GLODAP measurements. 87

Figure 3.2: Volumetric distribution of oceanic oxygen from different gridded data sets discussed in Section 3.2. Water volumes have been binned according to oxygen concentration in 5 $\mathrm{mmol\,m^{-3}}$ wide bins, starting from 0 $\mathrm{mmol\,m^{-3}}$. The data sets shown are: (a) WOA05; (b) objective analysis of GLODAP measurements following the mapping scheme by Gandin (1963); (c) objective analysis of GLODAP measurements following the mapping scheme by Barnes (1964); (d) WOA05 with linear correction based on in situ GLODAP measurements. 88

Figure 3.3: Thickness of the water column oxygen lower than 10 $\mathrm{mmol\,m^{-3}}$. The data sets shown are: (a) monthly WOA05; (b) objective analysis of GLODAP measurements following the mapping scheme by Gandin (1963); (c) objective analysis of GLODAP measurements following the mapping scheme by Barnes (1964); (d) monthly WOA05 with linear correction based on in situ GLODAP measurements. 89

Figure 3.4: (a) export from the euphotic zone from Dunne et al., (2007); (b) vertically integrated pelagic denitrification; (c) vertically integrated N_2O production; (d) benthic denitrification. Contouring is on a $\log_{10}$ scale. Averages from the three oxygen data set described in Section 3.2 are shown..... 90

Figure 3.5: Cumulative benthic denitrification integrated from the surface to a given depth, divided by basin. (a) depths between 0 and 250 m; (b) entire water column.....91

Figure 3.6: Relative sensitivity of pelagic denitrification, benthic denitrification and N_2O production to the model parameters. Sensitivities are calculated as fractional change in the global integrals for a change in each model parameter equal to one standard deviation (see Table 3.4). For example, the sensitivity of pelagic denitrification to changes in POC flux is calculated as: $\frac{\partial Denitr}{\partial \Phi_{POC}} \frac{\Delta \Phi_{POC}}{Denitr}$. Sensitivities equal to 0 indicate no change. 92

Figure 3.7: Sensitivity of (a) pelagic denitrification and (b) N_2O production to uniform changes (ΔO_2) in the ocean oxygen distribution. The solid line and the shading show the mean and standard deviation from a series of Monte Carlo simulations. 93

Figure 4.1: Ecosystem model structure. There are 10 main state variables (grey circles): SP= small phytoplankton, LP=large phytoplankton, SZ=small zooplankton, LZ=large zooplankton, LMZ= large migrating zooplankton, B=bacteria, SD_L=labile small detritus, SD_S=semilabile small detritus, N=limiting nutrient. HP=higher order predators that are not resolved explicitly. The dashed circle around small detritus components represents the combine small detrital pool. The circle around large zooplankton components rapresents the combined large zooplankton pool. Both LZ and LMZ groups are composed by three

internal pools as described in section 4.2.3, and schematized in Figure 4.2. Adapted from Stock and Dunne (2010). 147

Figure 4.2: Schematic of the three nutrient pools (rectangles) that compose large zooplankton (LZ) and vertically migrating zooplankton (LMZ) biomass, and the metabolic pathways that connect them (arrows). The numbers correspond to the following metabolic pathways: (1) ingestion, (2) egestion, (3) assimilation, (4) catabolism and (5) anabolism. See section 2.3 for details on the formulation of these fluxes 148

Figure 4.3: Example of (a) daily cycle in surface irradiance and (b) large migrating zooplankton (LMZ, colour) and depth of the $10^{-5}\,\mathrm{W\,m^{-2}}$ isolume (dot-dashed black line). Irradiance and model output are shown for January at station ALOHA in the subtropical Pacific Ocean (158°W, 22.5°). LMZ biomass has been rescaled between 0 and 1 for plotting reasons. 149

Figure 4.4: Light-dependent limitation factor for the ingestion rate of high order predators (f_{HP}^{Z}). The x-axis shows prey concentration ($\mathrm{mmolN\,m^{-3}}$). The left y-axis shows the local irradiance ($\mathrm{W\,m^{-2}}$). On the the right y-axis we converted the local irradiance to equivalent depth, assuming a surface irradiance of 200 $\mathrm{W\,m^{-2}}$ and water column conditions for the subtropical Pacific Ocean. The parameters used for the plot are: $K_Z = 1.0\,\mathrm{mmolN\,m^{-3}}$, $K_{irr} = 10^{-2}\,\mathrm{W\,m^{-2}}$, $\alpha^v = 0.9$. See section 2.4 for details. 150

Figure 4.5: Locations of model implementation. Station coordinates are: K2, 161°E, 47°N; ALOHA, 158°W, 22.5°; EQPAC, 140°W, 0°N. Contours show mean surface nitrate concentration from the World Ocean Atlas. 151

Figure 4.6: Surface forcings for the three locations of model implementations. (a) Surface air temperature (ºC); (b) daily mean shortwave irradiance at the surface ($\mathrm{W\ m^{-2}}$); (c) surface wind stress ($\mathrm{dyn\ cm^{-2}}$). 152

Figure 4.7: Upper panel: modeled annual cycle of temperature (colour), mixed layer depth (solid white line), euphotic zone depth (dashed white line), and depth of the $10^{-5}\,\mathrm{W m^{-2}}$ isolume (dot-dashed white line) for the three locations of model implementation. Lower panel: climatological annual cycle of temperature (colour) and mixed layer depth (solid white line) from the World Ocean Atlas, and mean euphotic zone depth (see Table 1 for references). Mixed layer depths are calculated with a $0.125\ \mathrm{kg m^{-3}}$ density difference criterion..... 153

Figure 4.8: Annual cycle of vertically integrated biomasses (0 - 600 m) for the three model locations. Biomasses have been converted to carbon units using a stoichiometric ratio of 106/16. Detritus biomasses indicated with a dashed line have been scaled to 10% of the original value to fit in the figure. 154

Figure 4.9: Sensitivity of the fraction of migrating zooplankton LMZ/(LMZ+LZ) to parameters controlling visual predation and DVM. Crosses indicate the values of the control runs. The parameters are: α^{v}, visual predation fraction; w^{ref}, velocity scale controlling the cost of swimming; irr^{DVM} preferred isolume, K_{irr}, half

saturation constant for the light response of visual predators. See sections 2.2-2.4 for details..... 155

Figure 4.10: Annual cycle of carbon fluxes ($\mathrm{mmol\,C\,m^{-2}d^{-1}}$) into the euphotic zone. Positive numbers indicate imports to the euphotic zone, negative number exports. Blue: N import due to physical processes and nutrient restoring, converted to carbon units by using a stoichiometric ratio equal to 106/16. Green: large sinking detritus (LD) export. Red: export due to DVM of large zooplankton (LMZ). Grey: all other sources of export, including downward diffusion of biomass for other functional groups. Black: net import/exports. 156

Figure 4.11: Annual mean respiratory/excretory fluxes and detritus production ($\mathrm{mmol\,C\,m^{-3}year^{-1}}$) in the mesopelagic zone. The green curve shows detritus respiration. The red curves show fluxes from the migrating zooplankton pool (LMZ) to the dissolved nutrient and small detritus (dark red) and large detritus (light red) pools. The blue curves show fluxes from all other state variables to the dissolved and small detritus (dark blue) and large detritus (light blue) pools... 157

Chapter 1: Introduction

1.1 Motivation

The distribution of biogeochemical tracers, chemicals dissolved in seawater that affect aspects as diverse as marine ecology and climate, lies at the intersection between ocean physics and biology.

For example, the availability of dissolved nutrients, including nitrate and phosphate, regulates productivity in the surface layers, from microscopic phytoplankton up to the level of fisheries. Dissolved oxygen supports the respiration and metabolism of the marine biosphere, and affects the distribution of organisms in the water column. The ocean stores a large and relatively mobile reservoir of carbon dioxide, and is a net source of nitrous oxide. Both are important greenhouse gases that affect the radiative budget of the Earth's atmosphere. Passive tracers such as noble gases, radiocarbon and anthropogenic chlorofluorocarbons have long provided valuable information on the pathways of water mass circulation and air-sea exchange.

The work presented in this thesis investigates the distribution and the processes controlling major biogeochemical tracers that are relevant for both ocean physics and biology. In particular, I focus on the distribution and controls on helium isotopes, oxygen and nitrogen. The implications of our work extend to the cycles of other nutrients and carbon.

1.2 The meridional overturning circulation and the return path of dense waters

The meridional overturning circulation of the ocean (MOC) transports mass, heat, salt and biogeochemical tracers from the surface high latitudes to the ocean interior (Ganachaud and Wunsch, 2000; Talley et al., 2003). Formation of deep dense water in the polar regions involves strong air-sea interactions and complex dynamics (Marshall and Schott, 1999). The return flow of the MOC requires the conversion of the dense waters back into light surface and intermediate waters. While the location, rates and processes that characterize the formation and sinking of dense waters are relatively well constrained, substantial uncertainty still exists on the return flow of the MOC and the physical mechanisms that drive it.

Observational estimates based on global inversion of hydrographical data imply significant upwelling of dense waters north of the Southern Ocean (Sloyan and Rinthoul, 2001; Talley et al., 2003; Lumpkin and Speer, 2007; Talley, 2008). By contrast, estimates based on coarse-resolution and eddy-permitting ocean general circulation models (GCMs; Gnanadesikan et al., 2004; Hallberg and Gnanadesikan, 2006), medium-resolution coupled GCMs (Gnanadesikan et al., 2006), and ocean state estimates from model assimilation of observations (Forget, 2009) suggest that most of the dense-to-light water transformation occurs within the Southern Ocean.

Broadly distributed upwelling throughout the mid- and low-latitude thermocline, driven by downward diffusion of heat, has long been proposed to drive the return flow of

dense waters (Stommel and Aarons, 1960; Munk, 1966). The large levels of mixing required in this scenario are not supported by microstructure and tracer diffusion measurements (Gregg, 1987; Ledwell et al., 1993). However, high large-scale diffusion could arise from localized 'hot spots' of intense mixing dispersed in a quiescent oceanic background (Munk and Wunsch, 1998), for example driven by interactions between tides, internal waves and topography (Polzin et al, 1997; Naveira-Garabato et al., 2004).

An alternative scenario that does not require large homogeneous mixing calls into play the role of wind driven upwelling and surface freshening of Circumpolar Deep Waters along the Antarctic Circumpolar Current in the Southern Ocean (Toggweiler and Samuels, 1993 and 1998).

These two views of the MOC imply dramatically different sensitivities to climate change. In the first scenario the forcings that drive dense-to-light water transformation are relatively stable. In the second scenario, changes in winds and freshwater fluxes over the Southern Ocean can induce rapid changes on the MOC and on the associated heat and carbon transports. Which scenario explains the real ocean is a fundamental question in oceanography and a topic of current research.

1.2.1 Helium-3 as a tracer of deep waters and its geochemical importance

Tracer observations can elucidate the return pathways associated with the MOC. In particular, the noble gas helium, characterized by a unique isotopic signature in the

ocean interior, can help shed light on the mechanisms and locations of dense-to-light water transformation.

^{3}He-enriched waters enter the ocean through hydrothermal vents at mid-ocean spreading centers (Clarke et al., 1969; Lupton, 1977). The oceanic circulation carries the high ^{3}He/^{4}He signal from mid-depths to the surface, where equilibration with the atmosphere takes place. The distribution of ^{3}He is shaped by the patterns of injection at depth, and by circulation and upwelling towards the outcrops.

In Chapter 2 of this thesis, I describe a set of simulations of the ^{3}He distribution with a suite of coarse-resolution ocean GCMs that encompass a range of possible circulations, including upwelling mostly in the mid- and low-latitude ocean and within the Southern Ocean, and that produce realistic distribution of ventilation tracers such as radiocarbon and chlorofluorocarbons. The model results were compared with a new ^{3}He dataset that I synthesized from recent global oceanographic surveys that were part of the World Ocean Circulation Experiment.

Unfortunately, the differences between the model patterns of oceanic ^{3}He were too subtle to be interpreted accurately in favour or against specific patterns of MOC upwelling – the original motivation of this study. However, all models – despite being tuned to match observational constraints – produced ^{3}He inventories in the ocean interior approximately 2 times higher than observed. This model result suggested that the currently accepted source of hydrothermal ^{3}He is too high by approximately a factor 2.

The outgassing flux of ^{3}He from mid-ocean ridges forms the basis of powerful methods for estimating chemical fluxes from the Earth's interior (Elderfield and Schulz, 1996), and provides a constraint on models of mantle evolution and dynamics (Ballentine

et al., 2002). In a paper appeared in *Earth and Planetary Science Letters* (Bianchi et al., 2010), which forms Chapter 2 of this thesis, we used the model simulations, in conjunction with the new helium isotope dataset, to revise the ^{3}He source to the oceans. This revision has implications ranging from geochemistry to mantle geodynamics. The new source function implied by this study will serve as a basis for future model analyses with new-generation ocean GCMs, including high-resolution and coupled models.

1.3 Oxygen minimum zones and biogeochemical controls on the biological pump

A tight interaction between ocean circulation and biogeochemistry regulates the distribution of oceanic oxygen. Oxygen dissolved in seawater ranges between super-saturation in well-mixed and productive surface layers, to undetectable within the so-called Oxygen Minimum Zones (OMZs).

Open ocean OMZs are subsurface features observed in oceanographic provinces characterized by high productivity and reduced water mass circulation and ventilation. Examples are the so-called "shadow zones" of the wind-driven thermocline (Karstensen et al., 2008). Oxygen minima are associated with stress and death of important macro organisms including fish (Gray et al., 2002). Suboxic and anoxic waters at the core of OMZs host microbial communities responsible for denitrification – the removal of fixed nitrogen from seawater – and for the production of nitrous oxide (Codispoti and Christensen, 1985).

Modeling studies predict an expansion of OMZs in response to climate change due to ocean warming and increased stratification (Sarmiento et al., 1998; Keeling et al., 2010), a result compatible with recent observational syntheses (Stramma et al., 2008).

A complex and fine balance is required to maintain OMZs, yet understanding the full extent of the controls and feedbacks on OMZ distribution is a current challenge for the oceanographic community. In our experience, global GCMs with different circulations and biogeochemical representations appear to overestimate the extent of anoxia compared to commonly-used global gridded datasets such as the World Ocean Atlas. This feature is common to low, intermediate and high-resolution models.

This model-data discrepancy led me to investigate two fundamental questions:

(1) What is the observed distribution of suboxic and anoxic water within the major OMZs?

(2) What is the impact of biological mechanisms generally overlooked by state-of art models on water column oxygen and biogeochemistry?

The answer to question (1) allows to establish a point of reference against which models of the oxygen distribution can be evaluated. Question (2) arises from the possibility that biogeochemical mechanisms are responsible for the mismatch between observations and models with variable physics and resolutions.

Answering these questions required synthesizing and analyzing existing observations, and developing a hierarchy of models of ecosystem and biogeochemistry to be used on a global scale. My work on these problems forms Chapter 3 and 4 of this thesis.

1.3.1 Global distribution of OMZs and their impact on the nitrogen cycle

In Chapter 3, which is part of a manuscript submitted to *Global Biogeochemical Cycles*, I show that the gridded World Ocean Atlas dataset overestimates oxygen in the core of OMZs compared to in situ measurements. This causes an underestimate of the global dstribution of suboxic and anoxic waters. I evaluate the distribution of the OMZs by mapping high-quality oxygen measurements from the WOCE program, and by applying an empirical correction to the gridded WOA based on in situ observations. The resulting suboxic volumes are a factor 3 larger than in the uncorrected gridded WOA.

By combining the new oxygen data sets with estimates of global export and simple models of remineralization I proceeded to explore the consequences of the revised OMZ distribution on denitrification and the nitrogen cycle.

1.3.2 Diel vertical migration impacts on water column biogeochemistry and ecosystem

Recent studies focusing on the interdependency between the biological pump and the carbon cycle (e.g. Kwon et al., 2009) have highlighted the importance of particle export and remineralization in the water column. However, particle cycling is only one aspect of the complex web of chemical, biological and ecological interactions that control export from the surface layers to the ocean interior.

Chapter 4 is devoted to the study of diel vertical migration (DVM) of zooplankton and fish – the largest migration on Earth in term of biomass. DVM has recently gained

consideration as a fundamental component of the biological pump on a global scale (Longhurst and Harrison, 1988; Steinberg et al., 2000; Hannides et al., 2009; Buesseler and Boyd, 2009).

DVM appears to be widespread in the ocean, where it alters the vertical fluxes of nutrients, oxygen and carbon. Excretion, fecal pellet production, and mortality of DVM organisms at depth form the active component of the biological pump, and contribute up to 30 % of particle export (Longhurst and Harrison 1988; Al-Mutairi and Landry, 2001; Steinberg et al., 2000; Hannides et al., 2009).

By controlling the inventory of respired nutrients in the ocean, the biological pump – including the active DVM component – regulates the air-sea carbon balance (Ito and Follows, 2005). This role depends not only on the amount of export, but also on the location in the water column where remineralization occurs (Kwon et al. 2009). While particle respiration decreases monotonically with depth (Martin et al., 1987), DVM transport is enhanced within the layers where migrating organisms reside during the day. Therefore, the response of carbon, nutrients and oxygen cycling to DVM is fundamentally different from the response to particle remineralization.

In addition to nutrients and carbon, oxygen can be affected by DVM. The daytime migration depth is associated at several locations with oxygen minima – an indication that low oxygen layers could serve as a refuge from large predators (Steinberg et al., 2008). However, it is not clear to what extent respiration by DVM organisms further enhances oxygen depletion. The possibility that migrating organisms contribute to maintaining low oxygen conditions, further inhibiting predatory losses, needs to be explored in detail.

In the manuscript that forms Chapter 4, I develop a representation of DVM in a size-structured NPZD model that shares a common structure with more complex models currently run at global scales. This study addresses two questions:

(1) What processes are required to produce a robust and consistent representation of DVM on a global scale?

(2) What are the impacts of DVM on the water column ecosystem, biogeochemistry, and biological pump?

To tackle these problems, I propose a consistent parameterization of visual predation, and a representation of the processes that decouple zooplankton feeding and respiration in the water column. I test the robustness and sensitivity of the model by evaluating it against data from three major biomes in the Pacific Ocean, and quantify the contributions of DVM to export and respiration at various locations in the water column. This study serves as a basis for global investigations of DVM effects on carbon, nutrient and oxygen cycling in the Earth System.

1.4 References

Al-Mutairi, H., Landry, M. R., 2001. Active export of carbon and nitrogen by diel migrant zooplankton at Station ALOHA. *Deep-Sea Research II,* 48, 2083–2103.

Ballentine, B. J., van Keken, P. E., Porcelli, D., Hauri, E. H., 2002. Numerical models, geochemistry and the zero-paradox noble gas mantle. *Phil. Trans. R. Soc. Lond. A*, 360, 2611–2631.

Bianchi D., Samiento, J. L., Gnanadesikan, A., Key, R. M., Schlosser, P., Newton, R., 2010. Low helium flux from the mantle inferred from simulations of oceanic helium isotope data. *Earth Planet. Sci. Lett.,*297, 379-386.

Buesseler, K. O., Boyd, P. W., 2009. Shedding light on processes that control particle export and flux attenuation in the twilight zone of the open ocean. *Limnol. Oceanogr.*, 54(4), 1210–1232.

Clarke, W. B., Beg, M. A., Craig, H., 1969. Excess 3He in the sea: evidence for terrestrial primordial helium. *Earth Planet. Sci. Lett.,* 6, 213-220.

Codispoti, L. A., and Christensen, J. P., 1985. Nitrification, denitrification and nitrous oxide cycling in the eastern tropical South Pacific Ocean, *Mar. Chem.,* 16, 277–300.

Elderfield, H., Schultz A., 1996. Mid-Ocean ridge hydrothermal fluxes and the chemical composition of the ocean. *Annu. Rev. Earth Planet. Sci.,* 24, 191–224.

Forget, G., 2009. Mapping ocean observations in a dynamical framework: a 2004-2006 ocean atlas. *J. Phys. Ocean.,*40, 1201-1221.

Ganachaud A., Wunsch, C., Improved estimates of global ocean circulation, heat transport and mixing from hydrographic data, 2000. *Nature*, 408, 453-458.

Gnanadesikan, A., Dunne, J. P., Key, R. M., Matsumoto, K., Sarmiento, J. L., Slater, R. D., Swathi, P. S., 2004. Oceanic ventilation and biogeochemical cycling: Understanding the physical mechanisms that produce realistic distributions of tracers and productivity. *Global Biogeochem. Cycles,* 18, GB4010.

Gnanadesikan, A., Dixon, K. W., Griffies, S. M., Balaji, V., Beesley, J. A., Cooke, W. F., Delworth, T. L., Gerdes, R., Harrison, M. J., Held, I. M., Hurlin, W. J., Lee, H.-C., Liang, Z., Nong, G., Pacanowski, R. C., Rosati, A., Russell, J., Samuels, B. L., Song, S. M., Spelman, M. J., Stouffer, R. J., Sweeney, C.O., Vecchi, G., Winton, M., Wittenberg, A.T., Zeng, F., Zhang, R., 2006. GFDL's CM2 global coupled climate models-part 2: the baseline ocean simulation. *J. Clim*. 19, 675–697.

Gray, J. S., Wu, R. S., Or, Y. Y., 2002. Effects of hypoxia and organic enrichment on the coastal marine environment. *Mar. Ecol. Prog. Ser*. 238, 249–279.

Gregg, M. C., 1987. Diapycnal mixing in the thermocline: a review. *J. Geophys. Res.,* 92, 5249-5286.

Hallberg, R.W. and Gnanadesikan, A., 2001. An exploration of the role of transient eddies in determining the transport of a zonally re-entrant current, *J. Phys. Oceanogr.*, 31, 3312-3330.

Hannides, C. C. S., Landry, M.R., Benitez-Nelson, C. R., Styles, R. M., Montoya, J. P., Karl, D. M., 2009. Export stoichiometry and migrant-mediated flux of phosphorus in the North Pacific Subtropical Gyre. Deep-Sea Research I, 56, 73–88.

Ito, T., Follows, M. J., Boyle, E. A., 2004. Is AOU a good measure of respiration in the oceans?, *Geophys. Res. Lett*., 31, L17305, doi:10.1029/ 2004GL020900.

Keeling, R. F., Kortzinger, A., Gruber, N., 2010. Ocean deoxygenation in a warming world, Annu. Rev. Mar. Sci., 2, 463–493.

Karstensen J., Stramma L., Visbeck M., 2008. Oxygen minimum zones in the eastern tropical Atlantic and Pacific oceans. *Prog. Oceanogr.*, 77, 331–50.

Kwon, E. Y., Primeau, F., Sarmiento, J., 2009. The impact of remineralization depth on the air–sea carbon balance. *Nature Geoscience*, 2, 630-635.

Ledwell, J. R., Watson, A. J., Law, C. S., 1993. Evidence for slow mixing across the pycnocline from an open-ocean tracer-release experiment. *Nature,* 364, 701–703.

Longhurst, A. R., Harrison, W.G., 1988. Vertical nitrogen flux from the oceanic photic zone by diel migrant zooplankton and nekton. *Deep-Sea Research I,* 35, 881–889.

Lumpkin, R., and Speer, K., 2007. Global Ocean Meridional Overturning. *J. Phys. Oceanogr.*, 37, 2550–2562.

Lupton, J. 1977. Mantle helium in hydrothermal plumes in Galapagos Rift. *Nature*, 267, 603-604.

Marshall, J., Schott, F., 1999. Open-ocean convection: observations, theory and models. *Rev. Geophys*., 37, 1-64.

Martin, J. H., Knauer, G. A., Karl, D. M., Broenkow, W. W., 1987. VERTEX: carbon cycling in the northeast Pacific. *Deep-Sea research*, 34, 267-285.

Munk, W., 1966. Abyssal recipes. *Deep-Sea research,* 13, 707-730.

Munk, W., and Wunsch, C., 1998. Abyssal recipes II: energetics of tidal and wind mixing. *Deep-Sea Res. I,* 145, 1977-2010.

Naveira-Garabato, A., Polzin, K. L., King, B. A., Heywood, K. J., Visbeck, M., 2004. Widespread intense turbulent mixing in the Southern Ocean. *Science*, 303, 210-213.

Polzin, K. L., Toole, J. M., Ledwell, J. R., Schmitt, R. W., Spatial variability of turbulent mixing in the abyssal ocean. *Science*, 276, 93-96.

Sarmiento J. L, Hughes, T. M. C., Stouffer, R. J., Manabe, S., 1998. Simulated response of the ocean carbon cycle to anthropogenic climate warming, *Nature,* 393:245–49.

Sloyan, B. M., and Rintoul, S. R., 2001. The Southern Ocean limb of the global deep overturning circulation. *J. Phys. Oceanogr*., 31, 143–173.

Steinberg, D. K, Carlson, C. A., Bates, N. R., Goldthwait, S. A., Madin, L. P., Michaels, A. F., 2000. Zooplankton vertical migration and the active transport of dissolved organic and inorganic carbon in the Sargasso Sea. *Deep-Sea Res. I,* 47: 137–158.

Steinberg, D. K., Cope, J. S., Wilson, S. E., Kobari, T., 2008. A comparison of mesopelagic zooplankton community structure in the subtropical and subarctic Pacific Ocean. Deep-Sea Research II, 55: 1594-1604.

Stommel, H., and Arons, A. B., 1960. On the abyssal circulation of the world ocean - I and II. *Deep-Sea Res*. 6, 140-154 and 217-233.

Stramma L., Johnson, G. C., Sprintall, J., Mohrholz, V. 2008. Expanding oxygen-minimum zones in the tropical oceans, *Science*, 320, 655–58.

Talley, L. D., 2003. Shallow, intermediate and deep overturning components of the global heat budget. *J. Phys. Ocean.*, 33, 530–560.

Talley, L. D., 2008. Freshwater transport estimates and the global overturning circulation: shallow, deep and throughflow components. *Prog. Ocean.*, 78, 257-303, doi:10.1016/j.pocean.2008.05.001.

Toggweiler, J. R., and Samuels, B., 1993. New radiocarbon constraints on the upwelling of abyssal water to the ocean's surface. The Global Carbon Cycle, M. Heimann, Ed., NATO ASI Series, Vol. I 15, Springer-Verlag, 334–366.

Chapter 2: Low helium flux from the mantle inferred from simulations of oceanic helium isotope data

Abstract

The high $^{3}He/^{4}He$ isotopic ratio of oceanic helium relative to the atmosphere has long been recognized as the signature of mantle ^{3}He outgassing from the Earth's interior. The outgassing flux of helium is frequently used to normalize estimates of chemical fluxes of elements from the solid Earth, and provides a strong constraint to models of mantle degassing. Here we use a suite of ocean general circulation models and helium isotope data obtained by the World Ocean Circulation Experiment to constrain the flux of helium from the mantle to the oceans. Our results suggest that the currently accepted flux is overestimated by a factor of 2. We show that a flux of 527±102 mol $year^{-1}$ is required for ocean general circulation models that produce distributions of ocean ventilation tracers such as radiocarbon and chlorofluorocarbons that match observations. This new estimate calls for a revision of the degassing fluxes of elements that are currently tied to the helium fluxes, including noble gases and carbon dioxide.

2.1 Introduction

The two stable helium isotopes found in the Earth System, ^{3}He and ^{4}He, have dramatically different origins. The more abundant ^{4}He is produced by radioactive decay of the natural uranium and thorium decay series, whereas most of the ^{3}He has a mantle origin and was trapped within the solid Earth during its accretion (Clarke et al., 1969). Helium is strongly incompatible with the minerals that form the Earth's mantle, and eventually escapes the solid phase during the processes that lead to crustal formation (Ballentine, 2007). Hydrothermal activity transfers helium with high $^{3}He/^{4}He$ isotopic ratios from new ocean crust to the ocean at active seafloor spreading centers (Lupton, 1977), hot-spots (Kurtz et al., 1982), and volcanic arcs (Poreda and Craig, 1989). Oceanic circulation eventually carries the high $^{3}He/^{4}He$ signal from the deep ocean towards the surface, where equilibration with the atmosphere takes place.

2.1.1 Geochemical importance of helium injection into the oceans

The injection of mantle ^{3}He from recently formed oceanic crust is perhaps the best-constrained chemical flux from the mantle and forms the basis of geochemical methods for estimating mantle fluxes of elements and heat to the oceans (Elderfield and Schultz, 1996). It also provides an important constraint for models of the structure and dynamics of the convecting mantle, and a boundary condition for the degassing history of the Earth through magmatism and crustal formation. For decades, several lines of

evidence related to the helium systematics supported the hypothesis of separate reservoirs of mantle material with limited mass transfer between them. These include ocean-island basalts that contain helium with high $^3He/^4He$ ratios if compared to mid-ocean ridges (Kurtz et al., 1982), the imbalance between ^4He and heat from the solid Earth (O'Nions and Oxburg, 1983), and the Earth's argon mass budget (Hart et al., 1979). Although the hypothesis of mantle layering with a transition at approximately 670 km depth is difficult to sustain in light of the geophysical and model-based evidence for whole-mantle convection (e.g. Van der Hilst et al., 1997, Van Keken and Ballentine, 1998), helium-based evidence for an undegassed reservoir remains. The three arguments for the layered mantle form part of the so-called helium paradox, and ultimately depend on the value of the ^3He concentration in the upper mantle (Ballentine et al., 2002). This ^3He concentration is estimated from the flux of mantle ^3He to the oceans and the average ocean-crust formation rate, under the assumption that helium is a highly incompatible element, and that most of it leaves the solid phase during mantle melting and crustal formation. Thus, the ^3He flux into the ocean is a crucial piece of information needed for resolving this paradox.

2.1.2 Estimates of helium injection

The flux of helium into the oceans could in principle be inferred from the concentration and removal processes in the atmosphere. However the variability in the atmospheric losses, and the existence of non-terrestrial sources with large uncertainty, such as auroral precipitation of solar wind, trapping of interstellar gases and cosmic ray interactions in the atmosphere (Torgersen, 1989), undermine this approach. A viable way

to quantify the flux of mantle ^{3}He is by inverting its large-scale distribution in the ocean. This method requires an estimate of the residence time of the oceanic water masses related to the large-scale circulation, together with the mean concentration of ^{3}He in the ocean determined from observations of the global ^{3}He field. The currently accepted value for the global flux of ^{3}He from mid-ocean ridge systems, $\Phi(^3\mathrm{He})=1070\pm270$ mol year^{-1}, results from early box-model calculations (Craig et al., 1975) that rely on a crude representation of the ocean circulation and gas exchange at the air/sea interface and were constrained by limited observations.

The box-model calculation of Craig et al. (1975) treats the deep ocean as a single well mixed reservoir, where hydrothermal injection produces an excess of helium with respect to atmospheric helium. ^{3}He-depleted bottom waters replace deep enriched waters, and the hydrothermal input of helium is balanced by upwelling out of the deep box. The equation resulting from the model is:

$$\Phi(^3\mathrm{He}) = \left[^3\mathrm{He}\right]^{eq} \cdot \left(\Delta^3\mathrm{He}^{deep} - \Delta^3\mathrm{He}^{0}\right) \cdot w_{upw} \cdot A^{oceans}$$

where $\left[^3\mathrm{He}\right]^{eq}$ is the equilibrium concentration, $\Delta^3\mathrm{He}^{deep}$ is the saturation anomaly in ^{3}He enriched deep water, $\Delta^3\mathrm{He}^{0}$ is the saturation anomaly in the new bottom waters flowing into the bottom box, w_{upw} is a large-scale upwelling velocity for the deep ocean, and A^{oceans} is the surface area of the world ocean.

Assuming, as in Craig et al. (1975), $\left[^3\mathrm{He}\right]^{eq} = 2.4\cdot10^{-12}\,\mathrm{mol\,m^{-3}}$, $\Delta^3\mathrm{He}^{deep} = 0.22$, $\Delta^3\mathrm{He}^{0} = 0.02$, $w_{upw} = 5\ \mathrm{m\,yr^{-1}} \approx 1.6\cdot10^{-7}\,\mathrm{m\,s^{-1}}$, $A^{oceans} = 3.61\cdot10^{14}\,\mathrm{m^2}$, gives a flux $\Phi(^3\mathrm{He}) = 866\ \mathrm{mol\,yr^{-1}} \approx 3.2\ \mathrm{atoms\,cm^{-2}_{earth}\,s^{-1}}$.

A similar calculation based on the ^{4}He flux and the ^{4}He to ^{3}He ratio of hydrothermal waters, gives $\Phi(^3\mathrm{He}) = 1282 \text{ mol yr}^{-1} \approx 4.8 \text{ atoms cm}^{-2}_{\text{earth}} \text{ s}^{-1}$. Altogether, the authors suggest $\Phi(^3\mathrm{He}) = 4 \pm 1 \text{ atoms cm}^{-2}_{\text{earth}} \text{ s}^{-1} \approx 1070 \pm 268 \text{ mol yr}^{-1}$ as a best estimate.

This calculation is based on qualitative and quantitative simplifications. First, a purely vertical advective balance for the ocean is a substantial oversimplification. In a vertical framework, turbulent vertical diffusion plays a non-negligible role, as acknowledged by the authors in earlier calculations (Craig and Clarke, 1970). Second, the fully three-dimensional pattern of advective and diffusive tracer fluxes should be considered, particularly eddy diffusion and advection along isopycnal surfaces. Finally, the large-scale upwelling velocity of 5 m year^{-1} used for the estimate, implies a global formation of about 60 Sv (1 Sv=10^6 m s^{-1}) of dense water. Other authors propose different, and substantially smaller estimates (e.g. Munk and Wunsch, 1998).

After the paper by Craig et al. (1975), other studies proposed a lower input of hydrothermal ^{3}He to the oceans. Jean Baptiste (1992) used a box-model of the three main ocean basins constrained by measurements of ^{3}He and radiocarbon to infer a hydrothermal ^{3}He input to the oceans of 267 – 534 mol year^{-1}. In addition to the box model calculations, indirect geochemical methods have been applied to suggest a low ^{3}He flux from mid-ocean ridge systems. Saal et al. (2002) used estimates of the abundance of CO_2 and ^{3}He to CO_2 ratios in undegassed mid-ocean ridge basalts, together with the rate of formation of new oceanic crust, to propose a flux of 422 ± 181 mol year^{-1}. However, the recent study by Cartigny et al. (2008) used a similar method and an extended dataset

to support the original estimate by Craig et al., (1975). Overall, geochemical methods appear to be restricted by uncertainties in the systematics of volatile elements in the Earth's mantle and on the formation rate of oceanic crust.

2.1.3 Previous modeling studies based on general circulation models

One way to address some of the issues raised by the Craig et al. (1975) and subsequent studies is to use ocean general circulation models (GCMs) to estimate the ocean inventory that results from a given helium source function. However, in a recent set of such simulations forced with a three-dimensional source of hydrothermal helium equal in magnitude to Craig et al.'s estimates (Farley et al., 1996; Dutay et al., 2004), the inventories of mantle helium were found to vary from model to model by more than a factor of three (Dutay et al., 2004). The use of these models to constrain the magnitude of the ^{3}He source would lead to an estimate with a similar uncertainty range. The large uncertainty originates from the sensitivity to model features such as the subgrid-scale parameterization of mixing processes and surface boundary conditions in regions where deep waters are formed.

2.1.4 Outline of the chapter

Such uncertainty calls for a consistent data-based model evaluation of the flux of primordial helium from the mid-ocean ridge system to the ocean. In this Chapter we take advantage of a new global dataset of helium isotopes and ocean transport tracers from the

World Ocean Circulation Experiment (WOCE) to update the existing estimates of the helium source, using a suite of ocean general circulation models (OGCMs) validated against the tracer observations. The rest of the Chapter is organized as follows. In section 2.2 we present our data based estimate of the mantle ^{3}He inventories and introduce the models used to constrain the ^{3}He oceanic source. In section 2.3 we discuss the model performance and revise the ^{3}He hydrothermal injection. In section 2.4 we discuss our result and its implications.

2.2 Methods

2.2.1 Observations of mantle helium in the ocean

We estimated mantle ^{3}He in the ocean from measurements of helium ([He]) and neon ([Ne]) concentration, as well as helium isotopic composition ($\delta^3\mathrm{He} = \left[\frac{^3\mathrm{He}/^4\mathrm{He}}{\left(^3\mathrm{He}/^4\mathrm{He}\right)_{\mathrm{Atmosphere}}} - 1\right] \cdot 100$). We combined available measurements produced during the World Ocean Circulation Experiment (WOCE), as well as previous cruises, into a synthetic gridded dataset for the world ocean. This dataset allows a large-scale inventory estimate and systematic model-observation comparison. Helium and neon measurements were converted to $\Delta\mathrm{He}$ and $\Delta\mathrm{Ne}$, the fractional deviations from the solubility equilibrium, using the equations of Weiss (1971). We corrected the data for intercalibration assuming a constant offset for each section. Published sections (Well and Roether, 2001; Hohmann et al., 2002, Well et al, 2003) were used as references with zero

offset, and profiles from regions where sections overlap were used to estimate the offsets. The intercalibrated measurements were interpolated on 25 depth surfaces and then mapped on a 1°x1° grid following the procedure described in Key et al. (2004).

Figure 2.1a shows a map of δ^3He interpolated to the 2500 m depth surface. Known features of the deep-ocean ^{3}He distribution are evident, such as small deviations from atmospheric equilibrium and contamination due to bomb tritium decay in the North Atlantic (Lupton, 1976; Top et al., 1987); values slightly above atmospheric equilibrium in the South Atlantic and Southern Ocean (Ruth et al., 2000); intermediate values in the Indian Ocean with a localized maximum in the region of the Central Indian Ridge (Srinivasan et al., 2004) and high values in the Pacific Ocean with maxima in the region of the East Pacific Rise (Lupton and Craig, 1981; Lupton, 1998). The smoothing associated with the large-scale horizontal interpolation reduces the resolution of some of the well-known oceanographic features highlighted by δ^3He measurements, such as the westward propagating plumes of high ^{3}He and the local maxima at the injection sites (Lupton, 1998, Lupton and Craig, 1981). Nonetheless, the mapping method is suitable for large-scale estimates of tracer inventories, as discussed in Key et al. (2004).

We separated the ^{3}He concentration into atmospheric and non-atmospheric components:

$$[^3\mathrm{He}] = [^3\mathrm{He}]^{\mathrm{atm}} + [^3\mathrm{He}]^{\mathrm{non\ atm}}$$

Whereas the atmospheric component is determined by the atmospheric mixing ratio and by air-sea processes, the non-atmospheric component results from mantle hydrothermal injection and tritiogenic helium:

$$[^3He]^{non\ atm} = [^3He]^{mantle} + [^3He]^{tritium}$$

We determined the non-atmospheric component of ^3He following the procedure introduced by Roether et al. (1998):

$$[^3He]^{non\ atm} = \left[\frac{\delta^3He - \delta^3He^0}{1 + \delta^3He^0} (\Delta He + 1) + (\Delta He - \Delta Ne) - (\Delta He - \Delta Ne)_{Mixed\ Layer} \right] \cdot [^3He]^0$$

Here δ^3He^0 is the solubility equilibrium value of δ^3He, $[^3He]^0$ the solubility equilibrium concentration of ^3He, and $(\Delta He - \Delta Ne)_{Mixed\ Layer} = 0.0001 \cdot \theta$ is a correction for water mass conditions in the mixed layer (Ruth et al., 2000), where θ is the potential temperature.

Figure 2.1b shows a map of the resulting water column inventory of $[^3He]^{non\ atm}$ for depths greater than 1000 m. By integrating the $[^3He]^{non\ atm}$ field in the deep ocean, we obtained a mantle ^3He inventory of 392 kmol. To avoid areas with potential contamination due to tritiogenic ^3He, we excluded in our analysis water-masses shallower than 1000 m, and water-masses with chlorofluorocarbon CFC-11 concentrations greater than 0.1 $pmol\,kg^{-1}$ in the GLODAP dataset (Key et al., 2004), and we assumed $[^3He]^{mantle} \cong [^3He]^{non\ atm}$. This reduces the volume of the deep-ocean domain to $7.3 \cdot 10^{17}$ m^3. The water masses excluded from the inventory calculation are recently ventilated and contain a small fraction of mantle helium. Therefore the exclusion of such water masses does not alter the results of our study.

The uncertainties associated with [He], [Ne] and δ^3He measurements are on average less than 1 %. A higher degree of uncertainty is introduced by the correction of ΔHe and ΔNe for intercalibration, which we estimate to be generally less than 1 % in deviation from solubility equilibrium. The bulk of the uncertainty on the inventory

estimate is mainly related to the objective mapping procedure and to the global integration. Following Key et al. (2004) we estimate an error on the $[^3He]^{mantle}$ inventory of approximately 15 %.

2.2.2 Models of helium isotpe distribution in the ocean

We included helium isotopes in three of the Princeton/GFDL ocean biogeochemistry model series (Gnanadesikan et al., 2004). The injection of mantle helium in the models follows the protocol specified by the Ocean Carbon Model Intercomparison Project phase 2 (OCMIP-2, Dutay et al., 2004), built upon the work by Farley et al. (1995). Mid-ocean ridges dominate the input of mantle helium to the ocean (Torgersen, 1989). The rate of injection is assumed to be proportional to the ridge spreading rate, and the injection is prescribed approximately 300 m above the ridge axis, where observations indicate that hydrothermal vents typically achieve neutral buoyancy. A constant rate of hydrothermal injection is assumed. This is equivalent to neglecting any fluctuations of hydrothermal injection on timescales longer than those associated with deep-water renewal. As noted by Farley et al. (1995), our knowledge of the time variability of hydrothermal venting and eruptions is too limited to explore time-varying inputs. No temperature anomaly is associated with the helium injection in the models. This temperature anomaly is thought to be a contributing cause of the westward propagating δ^3He plumes observed in the Pacific Ocean (Lupton, 1998) and their exclusion here limits the ability of the models to simulate such plumes.

The Pacific Ocean dominates ^{3}He injection (41 % of the total), followed by the Southern Ocean (33 %), the Indian Ocean (14 %) and the Atlantic Ocean (12 %). The

globally integrated flux $\Phi(^3\mathrm{He})$ in our first set of simulations is the canonical value of 1070 mol year^{-1} from Craig et al. (1975) and the isotopic ratio of the injected helium is 8 times the atmospheric ratio (R^{atm}), in agreement with observations of mid-ocean ridge basalts and hydrothermal vents. The dissolved helium pools exchange with atmospheric pools having a fixed mixing ratio of $x_{^4\mathrm{He}} = 5.24 \cdot 10^{-6}$ and isotopic ratio $R^{atm} = \frac{x_{^3\mathrm{He}}}{x_{^4\mathrm{He}}} = 1.384 \cdot 10^{-6}$.

The general circulation models used in this study are coarse-resolution, 4° versions of the GFDL Modular Ocean Model 3.0 (MOM3). Here we use the HH, P2 and P2A configurations documented in Gnanadesikan et al. (2004). The model suite is built around the theory of Gnanadesikan (1999) who showed how model aspects such as diapycnal diffusivity and Southern Ocean winds and eddies control the large-scale ocean circulation. Our models have, by construction, a realistic density structure and North Atlantic Deep Water (NADW) formation rate within the observed range, but differ in the mechanisms and pathways by which the dense water is brought back to the surface and converted to light water (see Figure 2.2d-f, upper circulation cell). A first pathway is the transformation by broad-scale upwelling through the main thermocline, mostly in the tropical regions, which is dominant in the high-mixing model (HH, Figure 2.2d). An alternative pathway is by wind-driven upwelling in the Southern Ocean as in the low-mixing high-wind model (P2A, Figure 2.2f). Both pathways are important in the intermediate-mixing low-wind model (P2, Figure 2.2e). The relative importance of these two pathways is a subject of active debate. Uniform high mixing in the thermocline is not supported by direct observations (Ledwell et al., 1993); however, upwelling focused in

regions of intense mixing could allow for dense-to-light water mass transformation outside the Southern Ocean (Polzin et al., 1997). In this case the average mixing over the entire thermocline would be higher than what is directly measured. Although high mixing is not required to drive the meridional overturning circulation (Toggweiler and Samuels, 1998), we include the models with high and intermediate mixing to be consistent with recent estimates based on analyses of observations (e.g. Talley, 2008) that imply that a large fraction of the water transformation occurs outside the Southern Ocean (see Figure 2.2a). Despite the differences found in the upper ocean transports, all three models have a fairly realistic deep water circulation, as indicated by NADW and Antarctic Bottom Water (AABW) transports in agreement with observational estimates (Figure 2.2). Gnanadesikan et al. (2004) provide additional validation of the models and analyze the balance between advective and diffusive fluxes of tracers of the ocean ventilation, namely radiocarbon ($\Delta^{14}C$), oxygen and chlorofluorocarbons. They show that these three particular models achieve a reasonable ventilation of the deep ocean by different circulation pathways, and that the dependency of the circulation on the model parameters is complex, with changes in diffusivity giving rise to major changes in diffusive and advective fluxes. The model intercomparison study by Matsumoto et al. (2004) provides a supplementary discussion of the deep ocean ventilation, and shows that the models used in our study are among the best of all the models considered in terms of chlorofluorocarbon and radiocarbon diagnostics.

2.3 Results and discussion

We calculated the deep ocean inventory of mantle ^{3}He for each model (Table 2.1) for the region identified previously in section 2.2. The models HH, P2 and P2A produce inventories of 700, 886, 824 kmol respectively, compared with the observed inventory of 392 kmol. As shown in Table 2.1 the models overestimate the inventory of deep ^{3}He by approximately a factor of 2. This suggests that either the model ^{3}He injection is too high, or that the model circulation biases result in excessively slow deep-ventilation of ^{3}He.

The latter hypothesis can be evaluated by looking at simulations of radiocarbon $\Delta^{14}C$) and chlorofluorocarbons (CFCs) in the same models. Figure 2.3a shows a scatter-plot of mantle ^{3}He versus radiocarbon for the deep ocean, for both observations (black) and models using the hydrothermal injection of Craig et al. (1975) (colors). Overall, the models produce a radiocarbon range close to observations. Whereas PA and P2A underestimate the deep radiocarbon by less than 20 permil in localized regions, HH overestimates it by approximately the same amount. Considering the magnitude of the signal and the uncertainty in the observational dataset, the agreement with observations indicates that the models have a realistic representation of the residence time of deep waters on centennial time scales (as discussed in Gnanadesikan et al., 2004 and Matsumoto et al., 2004). Table 2.1 shows that the models reproduce to a good approximation the large-scale $\Delta^{14}C$ signal of the North Pacific Deep Water (NPDW), as well as the $\Delta^{14}C$ gradient between NPDW, Indian Deep Water (IDW) and Circumpolar Deep Water (CDW). This implies that the models move tracers between these basins and the Southern Ocean at a realistic rate.

Additionally, CFC inventories (Table 2.1, see also Matsumoto et al., 2004) show that the ventilation of CDW and AABW occurs at a realistic rate. CFCs have an equilibration timescale in the mixed layer of few weeks, similar to the ^{3}He equilibration timescale. A realistic uptake of CFCs implies that the models reasonably simulate the exchange between atmosphere, surface and deep waters for tracers with a rapid equilibration timescale. Taken together, analyses of the ventilation tracers in these particular models make it very unlikely that circulation is the principal cause of the model overestimate of the mantle ^{3}He inventory. Therefore, we conclude that the overestimate is most likely due to the previous estimates of the mantle ^{3}He source being too large.

Thus, we revise the flux of mantle ^{3}He to the oceans by fitting the model mantle ^{3}He inventories to the observed one. We force our models to match the observed deep ocean inventory by reducing the magnitude of the helium injection, while maintaining its three-dimensional structure. We reduce the ^{3}He source in each model by a factor given by the ratio between the modeled ^{3}He inventory (with the standard source of 1070 mol year^{-1}) and the observed mantle ^{3}He inventory. The resulting factors are 1.8, 2.3 and 2.1 for the model HH, P2 and P2A respectively, as shown in Table 2.1. Figure 2.3b shows the results of models with a helium injection reduced to match the observed deep ocean ^{3}He inventory. Whereas all models in Figure 2.3a overestimate mantle helium concentrations, the models in Figure 2.3b preserve the original fit to radiocarbon while producing by construction a distribution within the range of observations for mantle helium. Changes in the circulation alone would be able to reduce the model mantle helium in Figure 2.3a only by substantially increasing the deep ocean ventilation, increasing the radiocarbon content of deep waters to higher values than observed. In

contrast, Figure 2.3b shows that changes in the helium injection can reduce mantle helium without altering the radiocarbon distribution, allowing for a realistic simulation of both tracers simultaneously.

The models forced to reproduce the global deep mantle ^{3}He inventory produce global patterns of δ^3He (Figure 2.4) and inventories of mantle ^{3}He (Figure 2.5) that are in good agreement with observations. Compared to observations, the models show a reduced westward propagation of the helium signal from the source regions in the East Pacific rise, perhaps due to the lack of a thermal anomaly associated with the hydrothermal injection. This reduction in circulation translates into a simultaneous overestimate of ^{3}He and underestimate of radiocarbon at these locations, resulting in a few high-helium and low-radiocarbon points in Figure 2.3b. Nonetheless, as indicated by the zonal averages shown in Figure 2.6, there is a compensation between the δ^3He overestimate in the eastern side of the basin and the underestimate in the western side. Taken together, Figures 2.4 and 2.6 show that the large scale δ^3He signal of the models compares well with observations, including the observed maxima at mid depth, as well as the meridional and vertical gradients between such maxima and helium-depleted surface and bottom waters.

If the high-mixing model is representative of the ocean state, then a flux $\Phi(^3\text{He})= 599$ mol year^{-1} is consistent with the observed helium distribution. If either the low mixing or the intermediate mixing models are better approximations of the ocean state, then the estimates become $\Phi(^3\text{He})= 509$ and 473 mol year^{-1}, respectively. By combining the three model estimates, and considering the range of variability provided by the

models as well as the uncertainty on the observational dataset, we obtain a helium injection of 527±102 mol year^{-1}. This value is in agreement with the early box-model estimate by Jean-Baptiste (1992) and with the indirect estimate by Saal et al. (2002) based on the geochemistry of volatile elements in the upper mantle.

2.4 Conclusions

We used a suite of coarse resolution OGCMs forced to match the observed large-scale ^{3}He distribution to estimate the global flux of ^{3}He to the deep ocean. Our result implies that the currently accepted estimate of the ^{3}He degassing from the mantle is overestimated by approximately a factor of 2. A series of parameter sensitivity studies shows that this result is relatively robust to how individual models ventilate the deep ocean. We argue that such models, calibrated to provide a realistic density structure and ventilation timescale for the deep ocean, are suitable for estimating the integrated flux of helium from the mid-ocean ridge system. This does not mean that the mechanisms involved are necessarily correct: coarse models may be maintaining a realistic level of ventilation by using high lateral diffusivity coefficients to represent the effects of mesoscale eddies and poorly resolved boundary currents, shifting transport from advective to diffusive mechanisms. Unfortunately, it is at present impractical to carry out fully eddy resolving simulations for long enough time to equilibrate the deep mean radiocarbon and ^{3}He distributions. Nonetheless, a reduction of the hydrothermal helium injection is still required to match the relationship between radiocarbon and mantle ^{3}He shown in Figure 2.3. Finally, the use of a suite of models that bracket observations allows

us to estimate a range for the helium flux (425 – 629 mol year^{-1}) that reflects both the uncertainty in measurements, and the uncertainty in our ability to simulate the deep ocean ventilation.

The new estimate has important consequences for mantle geochemistry and requires reconsideration of the fluxes and budgets of elements that are directly derived from the ^{3}He degassing flux, including noble gases and carbon dioxide (Ballentine, 2007, Marty and Jambon, 1987). For example, combining our estimate of ^{3}He outgassing with estimates of $CO_2/^3He$ ratios in the mantle ($2.2 \pm 0.7 \cdot 10^9$, Saal et al., 2002) produces a flux of carbon from the mantle to the oceans equal to $1.2 \pm 0.4 \cdot 10^{12}$ mol year^{-1}, or 0.014 ± 0.005 Pg year^{-1}. This is on the lower range of existing estimates, and much lower than recently proposed values (e.g. $20 \pm 10 \cdot 10^{12}$ mol year^{-1}, or 0.24 ± 0.12 Pg year^{-1}, Helo et al., 2011).

Further implications involve the paradoxes placed by noble gas systematics on mantle chemical geodynamics. Recently, Ballentine et al. (2002) proposed that a concentration of ^{3}He in the convecting mantle which is higher than the currently accepted estimate by a factor of 3.5, the so-called 'zero paradox' concentration, would relax the arguments in favor of the layered mantle model, reconciling geochemical and geophysical evidence.

To the extent that the present-day ^{3}He flux from the mid-ocean ridge system can be extrapolated to the timescales of ocean-floor generation, its value can be used to calculate the average ^{3}He concentration in the upper mantle. Our estimate of the ^{3}He degassing flux implies that this concentration is 1/2 than previously assumed, and 1/7th

the ‘zero paradox’ concentration, thus reducing the likelihood that the paradox can be resolved in this way.

2.5 References

Ballentine, C. J., 2007. Earth holds its breath. *Nature*, 449, 294–296.

Ballentine, B. J., van Keken, P. E., Porcelli, D., Hauri, E. H., 2002. Numerical models, geochemistry and the zero-paradox noble gas mantle. *Phil. Trans. R. Soc. Lond. A* ,360, 2611–2631.

Cartigny, P., Pineau, F., Aubaud, C., Javoy, M., 2008. Towards a consistent mantle carbon flux estimate: insights from volatile systematics (H_2O/Ce, δD, CO_2/Nb) in the North Atlantic mantle (14°N and 34°N). *Earth Planet. Sci. Lett.,* 265, 672-685.

Clarke, W. B., Beg, M. A., Craig, H., 1969. Excess 3He in the sea: evidence for terrestrial primordial helium. *Earth Planet. Sci. Lett.,* 6, 213-220.

Craig, H., Clarke, W. B., 1970. Oceanic ^{3}He: Contributions from cosmogenic tritium. *Earth Planet. Sci. Lett.,* 9, 45-48.

Craig, H., Clarke, W. B., Beg, M. A., 1975. Excess ^{3}He in deep water on the East Pacific Rise. *Earth Planet. Sci. Lett.,* 26, 125–132.

Dutay, J.-C., P. Jean-Baptiste, J.-M. Campin, A. Ishida, E. Maier-Reimer, R. J. Matear, A. Mouchet, I. J. Totterdell, Y. Yamanaka, K. Rodgers, G. Madec, J. C. Orr,

2004. Evaluation of OCMIP-2 ocean models' deep circulation with mantle helium-3. *J. Mar. Systems,* 48/1-4, 15–36.

Elderfield, H., Schultz A., 1996. Mid-Ocean ridge hydrothermal fluxes and the chemical composition of the ocean. *Annu. Rev. Earth Planet. Sci.,* 24, 191–224.

Farley, K. A., Maier-Reimer E., Schlosser P., Broecker W. S., 1995. Constraints on mantle He-3 fluxes and deep-sea circulation from an ocean general circulation model. *J. Geophys. Res.,* 100, 3829–3839.

Forget, G., 2009. Mapping ocean observations in a dynamical framework: a 2004-2006 ocean atlas. *J. Phys. Ocean.,*40, 1201-1221.

Gnanadesikan, A., 1999. A simple predictive model for the structure of the oceanic pycnocline. *Science,* 283, 2077–2079.

Gnanadesikan, A., Dunne, J. P., Key, R. M., Matsumoto, K., Sarmiento, J. L., Slater, R. D., Swathi, P. S., 2004. Oceanic ventilation and biogeochemical cycling: Understanding the physical mechanisms that produce realistic distributions of tracers and productivity. *Global Biogeochem. Cycles,* 18, GB4010.

Hart R., Dymond, J., Hogan, L., 1979. Preferential formation of the atmosphere-sialic crust system from the upper mantle. *Nature* 278, 156-159.

Helo , C., M.-A. Longpré, N. Shimizu, D. A. David A. Clague, J. Stix, 2011. Explosive eruptions at mid-ocean ridges driven by CO_2-rich magmas. *Nat Geosci*, 4, 10.1038/NGEO1104

Hohmann, R., Schlosser, P., Jacobs, S., Ludin, A., Weppernig, R., 2002. Excess helium and neon in southeast Pacific: Tracers of glacial meltwater. *J. Geophys. Res.,* 107, NO. C11, 3198, doi:10.1029/2000JC000378.

Jean-Baptiste, P., 1992. Helium-3 distribution in the deep world ocean. In: Rozanski, K. (Ed.), Isotopes of Noble Gases as Tracers in Environmental Studies. International Atomic Energy Agency, Vienna, pp. 219–240.

Key, Robert M., Kozyr, A. , Sabine, C. L., Lee, K., Wanninkhof, R., Bullister, J. L., Feely, R. A., Millero, F. J., Mordy, C., Peng, T.-H., 2004. A global ocean carbon climatology: Results from Global Data Analysis Project (GLODAP), *Global Biogeochem. Cycles*, 18, GB4031, doi:10.1029/2004GB002247.

Kurz, M. D., Jenkins, W. J., Hart, S. R., 1982. Helium isotope systematics of oceanic islands and mantle heterogeneity. *Nature,* 297, 42–46.

Ledwell, J. R., Watson, A. J., Law, C. S., 1993. Evidence for slow mixing across the pycnocline from an open-ocean tracer-release experiment. *Nature,* 364, 701–703.

Lumpkin, R., and Speer, K., 2007. Global Ocean Meridional Overturning. *J. Phys. Oceanogr.*, 37, 2550–2562.

Lupton, J., 1976. The ^{3}He distribution in deep water over the mid-atlantic ridge. *Earth Planet. Sci. Lett*., 32, 371–374.

Lupton, J. 1977. Mantle helium in hydrothermal plumes in Galapagos Rift. *Nature*, 267, 603-604.

Lupton, J. and Craig, H., 1981. A major helium-3 source at 15°S on the East Pacific Rise. *Science,* 214, 13-18.

Lupton, J., 1998. J. Hydrothermal helium plumes in the Pacific Ocean. *J Geophys. Res.,* 103 (C8), 15853–15868.

Lupton, J.E., Weiss, R.F., Craig, H., 1977. Mantle helium in hydrothermal plumes in the Galapagos Rift. *Nature,* 267, 603.

Marty, B. and Jambon, A., 1987. C/^{3}He in volatile fluxes from the solid Earth: Implication for carbon geodynamics. *Earth Planet. Sci. Lett*., 83,16–26.

Matsumoto, K., Sarmiento, J. L., Key, R. M., Aumont, O., Bullister, J. L., Caldeira, K., Campin, J-M., Doney, S. C., Drange, H., Dutay, J-C., Follows, M., Gao, Y., Gnanadesikan, A., Gruber, N., Ishida, A., Joos, F., Lindsay, K., Maier-Reimer, E., Marshall, J., Matear, R., Monfray, P., Mouchet, A., Najjar, R. G., Plattner, G-K., Schlitzer, R., Slater, R. D., Swathi, P. S., Totterdell, I. J., Weirig, M-F., Yamanaka, Y., Yool, A., Orr, J. C., 2004. Evaluation of ocean carbon cycle models with data-based metrics. *Geophys. Res. Lett*., 31, L07303.

Munk, W., and Wunsch, C., 1998. Abyssal recipes II: energetics of tidal and wind mixing. *Deep-Sea Res. I,* 145, 1977-2010.

O'Nions, R. K., and Oxburg, E. R., 1983. Heat and helium in the earth. *Nature,* 306, 429–431.

Polzin, K. L., Toole, J. M., Ledwell, J. R., Schmitt, R. W. 1997. Spatial variability of turbulent mixing in the abyssal ocean. *Science,* 276, 93–96.

Poreda, R., and Craig, H., 1989. Helium isotope ratios in circum-Pacific volcanic arcs. *Nature,* 338, 473–477.

Roether, W., Well, R., Putzka, A., Ruth, C., 1998. Component separation of oceanic helium. *J. Geophys. Res.,* 103(C2), 27931–27946.

Ruth, C., Well, R., Roether, W., 2000. Primordial ^{3}He in South Atlantic deep waters from sources on the Mid-Atlantic Ridge. *Deep-Sea Res. I,* 47, 1059–1075.

Saal, A. L., Hauri, E. H., Langmuir, C. H., Perfit, M. R., 2002. Vapour undersaturation in primitive mid-ocean-ridge basalt and the volatile content of Earth's upper mantle. *Nature*, 419, 451–455.

Srinivasan, A., Top, Z., Schlosser, P., Hohmann, R., Iskandarani, M., Olson, D. B., Lupton, J. E., Jenkins, W., 2004. Mantle ^{3}He distribution and deep circulation in the Indian Ocean. *J. Geophys. Res,* 109, C06012.

Talley, L. D., 2008. Freshwater transport estimates and the global overturning circulation: shallow, deep and throughflow components. *Prog. Ocean.*, 78, 257-303, doi:10.1016/j.pocean.2008.05.001.

Toggweiler, J. R., and Samuels, B., 1998. On the ocean's large-scale circulation near the limit of no vertical mixing. *J. Phys. Ocean.*, 28(9), 1832–1852.

Top, Z., Clarke, W. B., Jenkins, W. J., 1987. Tritium and primordial SHe in the North Atlantic: a study in the region of Charlie-Gibbs Fracture Zone. *Deep-Sea Res.,* 34, 287-298.

Torgersen, T., 1989. Terrestrial helium degassing fluxes and the atmospheric helium budget: Implications with respect to the degassing processes of continental crust. *Chemical Geology*, 79, 1–14

Van der Hilst, R. D., Widiyantoro, D. S., Engdahl, E. R., 1997. Evidence for deep mantle circulation from global tomography. *Nature,* 386, 578–584.

Van Keken, P. E., and Ballentine, C. J., 1998. Whole-mantle versus layered mantle convection and the role of a high-viscosity lower mantle in terrestrial volatile evolution. *Earth Planet. Sci. Lett*., 156, 19–32.

Weiss, R. F., 1971. Solubility of Helium and Neon in Water and Seawater. *J. of Chem. and Engin. Data*, 16, 235-241.

Well, R., and Roether, W., 2001. Neon distribution in South Atlantic and South Pacific waters. *Deep-Sea Res. I,* 50, 721-735.

Well, R., Lupton, J., Roether, W., 2003. Crustal helium in deep Pacific waters. *J. Geophys. Res,* 106, C7, 14165-14177.

Table 2.1 : Estimates based on analysis of observations and model results for mean $\Delta^{14}C$ in the North Pacific Deep Water, Indian Deep Water and gradients with Circumpolar Deep Waters; CFC-11 inventory in the deep Southern Ocean, inventory of mantle ^{3}He in the deep ocean, and ratio between the mantle ^{3}He inventory in the models and in the observational estimate. See Section 2.3 for a discussion

	NPDW $\Delta^{14}C$[(a)] (permil)	NPDW to CDW $\Delta^{14}C$ gradient[(b)] (permil)	IDW to CDW $\Delta^{14}C$ gradient[(c)] (permil)	CDW and AABW CFC-11 inventory[(d)] (10^{6} mol)	Deep Ocean ($7.3 \cdot 10^{17}$ m^{3}) mantle ^{3}He inventory [(e)] (10^{3} mol)	Ratio between model and observationally estimated mantle ^{3}He
Observations	-216	-64	-43	23	392	-
HH	-194	-48	-21	24	700	1.8
P2	-226	-62	-37	17	886	2.3
P2A	-223	-52	-33	33	824	2.1

(a) NPDW average $\Delta^{14}C$ for latitudes between the equator and 60°N, longitudes between 150°E and 110°W and depths greater than 1000 m. The observational estimate is from the GLODAP dataset (Key et al., 2004)

(b) CDW average $\Delta^{14}C$ for latitudes between 70°S and 40°S, longitudes between 150°E and 110°W and depths greater than 1000 m.

(c) IDW average $\Delta^{14}C$ for latitudes between 20°S and 30°N, longitudes between 40°E and 100°E and depths greater than 1000 m. CDW average $\Delta^{14}C$ for latitudes between 70°S and 40°S, longitudes between 40°E and 100°E and depths greater than 1000 m.

(d) Inventory for depths greater than 1500 m, south of 40°S. The observational estimate is from the GLODAP dataset (Key et al., 2004).

(e) Inventory for depths greater than 1000 m, excluding water masses where observational estimates (Key et al., 2004) show CFC-11 concentrations higher than 0.1 pmol kg^{-1}, to avoid potential contamination with tritiogenic ^{3}He. The resulting deep ocean volume is $7.3 \cdot 10^{17}$ m^{3}. Model results are shown for a global injection of mantle ^{3}He equal to 1070 mol $year^{-1}$.

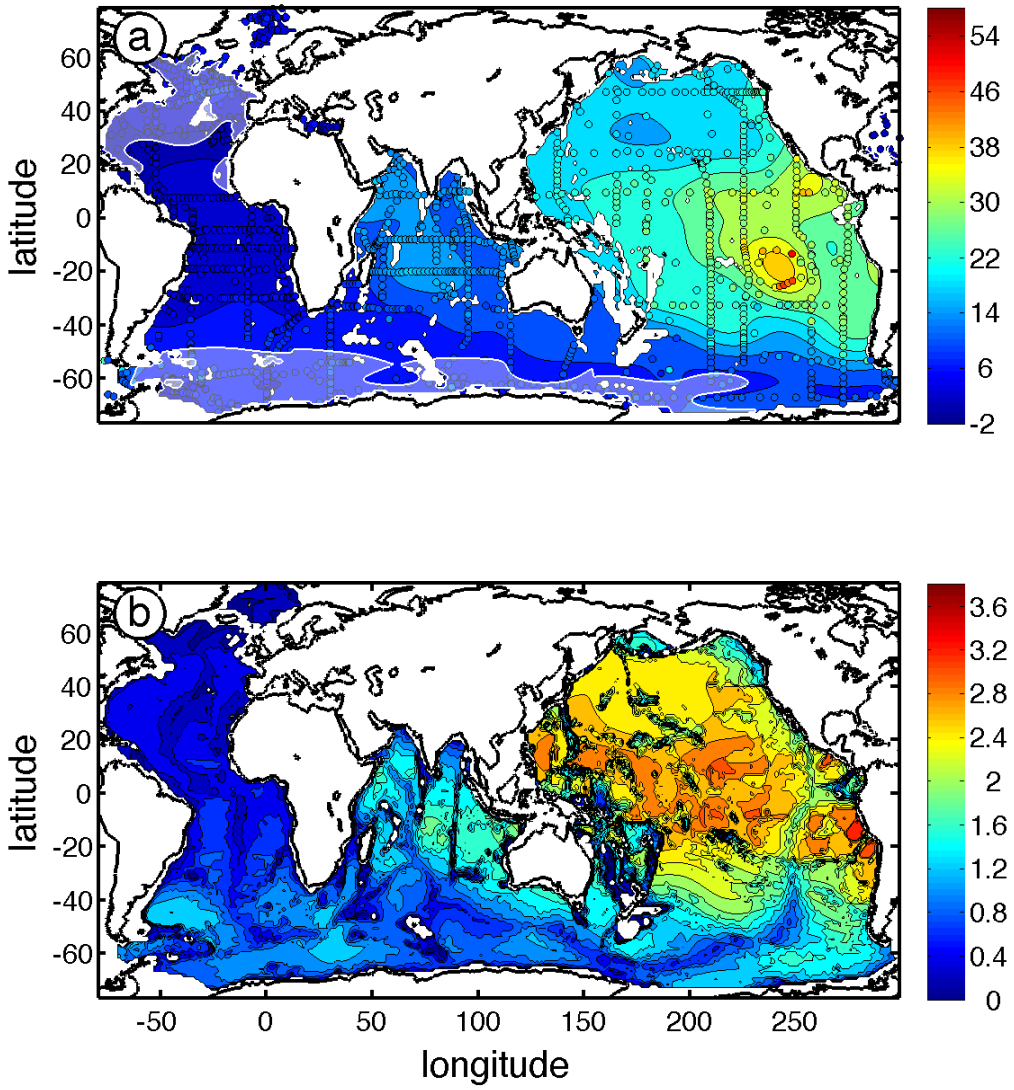


Figure 2.1: Observational dataset. (a) δ^3He at 2500 m depth from objective analysis of observations. Coloured circles are observed profiles interpolated to 2500 m depth. Units are percent. The white-hatched region indicates water masses with CFC-11 concentration higher than 0.1 pmol kg^{-1} from the GLODAP dateset (Key et al., 2004), indicating potential contamination due to tritiogenic ^{3}He (b) Vertical column inventories of non-atmospheric ^{3}He for depths greater than 1000 m. Units are nmol m^{-2}.

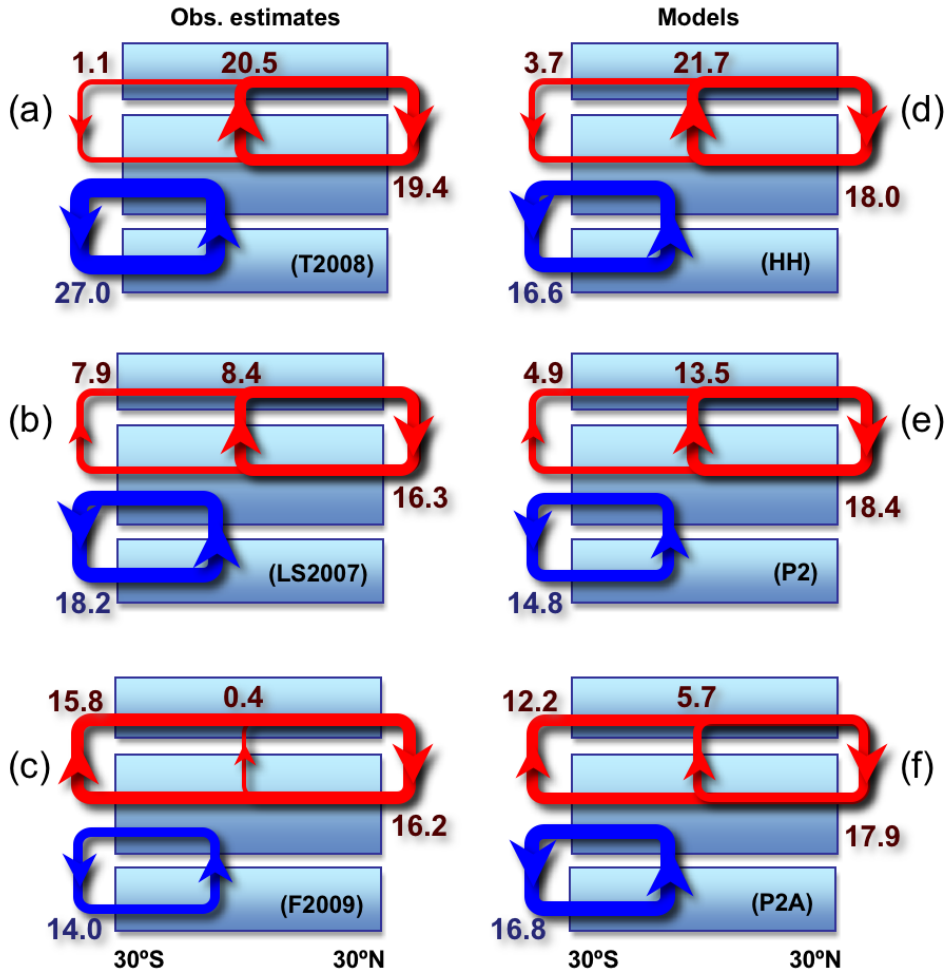


Figure 2.2: Schematic representation of the deep-water circulation for observational estimates and models. In each panel the upper cell (red) shows the maximum NADW overturning between 45°N and 48°N and deep to surface water conversion inside and outside the Southern Ocean at 30°S. The lower cell (blue) shows the dense water export from the Southern Ocean at 30°S. Layer boundaries are approximately 1200 m and 3000 m depth, corresponding to approximately 27.4 σ_θ and 45.86 σ_4 potential densities. Units are Sv ($1\,\mathrm{Sv} = 10^6\,\mathrm{m}^3\mathrm{s}^{-1}$). (a-c) Observationally based estimates. T2008 is the inverse estimate of hydrographic data from Talley (2008); LS2007 is the inverse estimate of hydrographic data from Lumpkin and Speer (2007); F2009 is the ocean state estimate from GCM assimilation of altimetry data, satellite SST and ARGO profiles from Forget (2009). (d-f) Models: HH, P2 and P2A. See section 2.2 for details on the models.

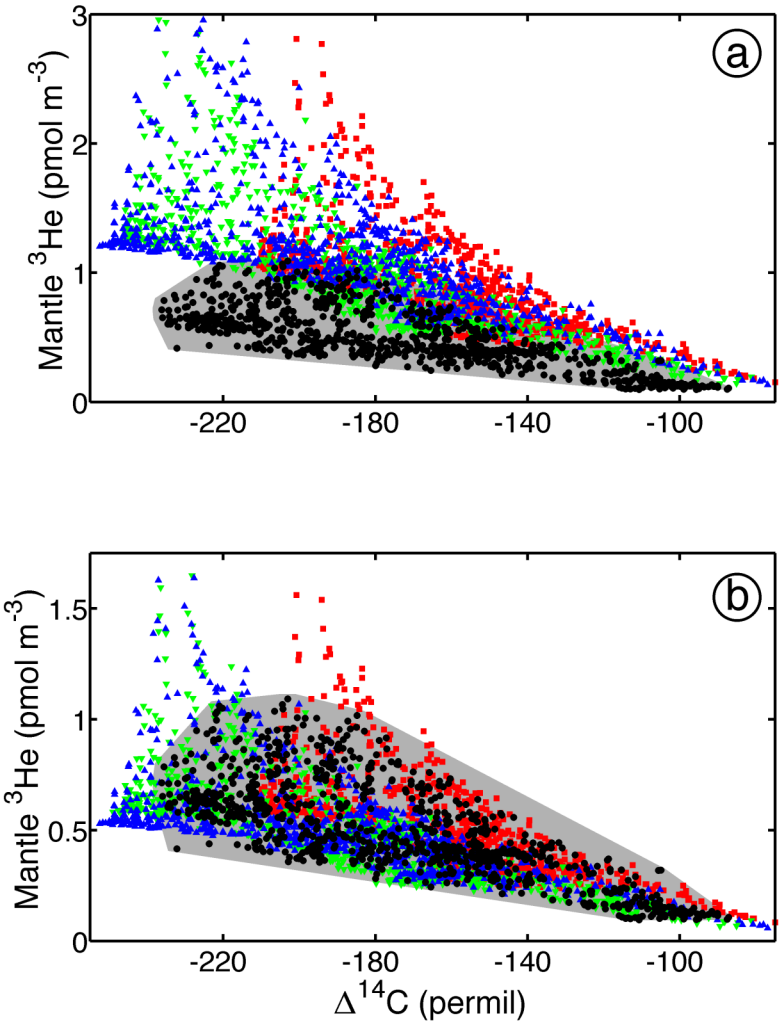


Figure 2.3: Scatter-plot of mantle ^{3}He (pmol m^{-3}) versus Δ^{14}C (permil) for the deep ocean. Black dots are observations, red squares, green triangles and blue triangles are HH, P2A and P2 models respectively. The dark shading highlights the envelope of observations. Each dot represents a large-scale average over a 20° by 20° region. Depths greater than 1000 m and water masses with observed CFC-11 concentration higher than 0.1 pmol kg^{-1} have been excluded to avoid potential contamination with tritiogenic ^{3}He. (a) Models with a helium injection of 1070 mol years^{-1}. (b) Models with helium injection reduced to match the observed deep ocean ^{3}He inventory.The ^{3}He injection is 599, 509 and 473 mol years^{-1} for the HH, P2A and P2 models respectively.

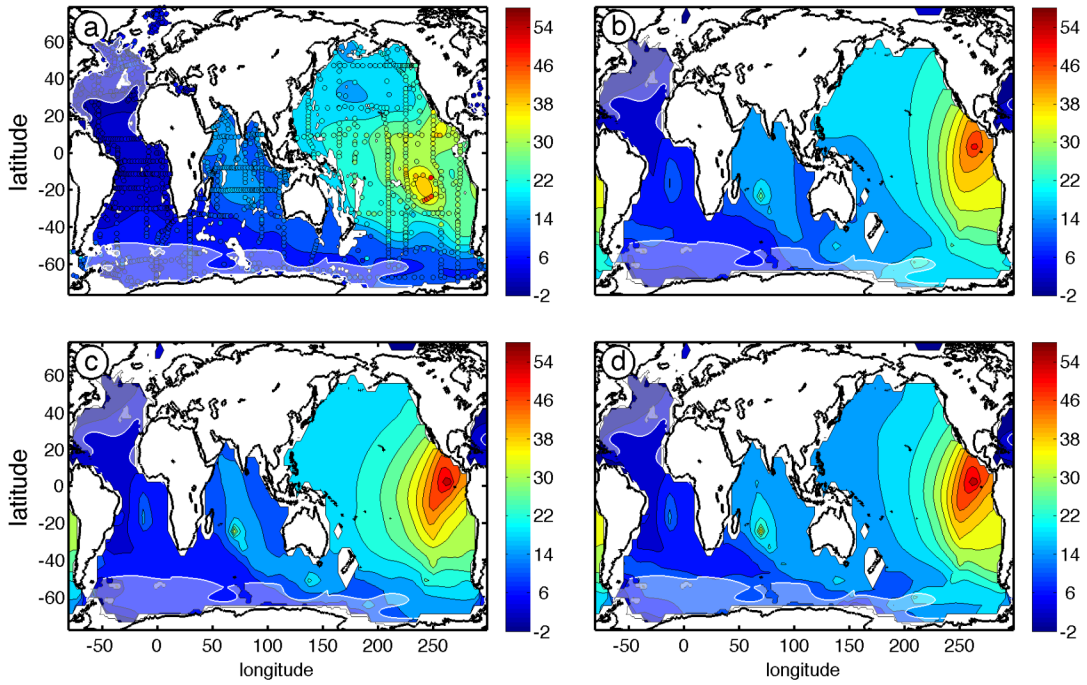


Figure 2.4: δ^3He at 2500 m depth. Units are percent. (a) Observational dataset. Colored circles are observed profiles interpolated to 2500 m depth. (b-d) HH, P2A and P2 models with ^{3}He injection reduced to match the observed deep ocean ^{3}He inventory. The ^{3}He injection is 599, 509 and 473 mol years^{-1} for the HH, P2A and P2 models respectively. The white-hatched region indicates water masses with CFC-11 concentration higher than 0.1 pmol kg^{-1} from the GLODAP dateset (Key et al., 2004), indicating potential contamination due to tritiogenic ^{3}He. The reduced zonal propagation of the ^{3}He signal in the Pacific Ocean for the models in (b-d) is discussed in section 2.3. Meridional sections for the Pacific Ocean indicating zonal compensation of the ^{3}He signal are shown in Figure 2.6.

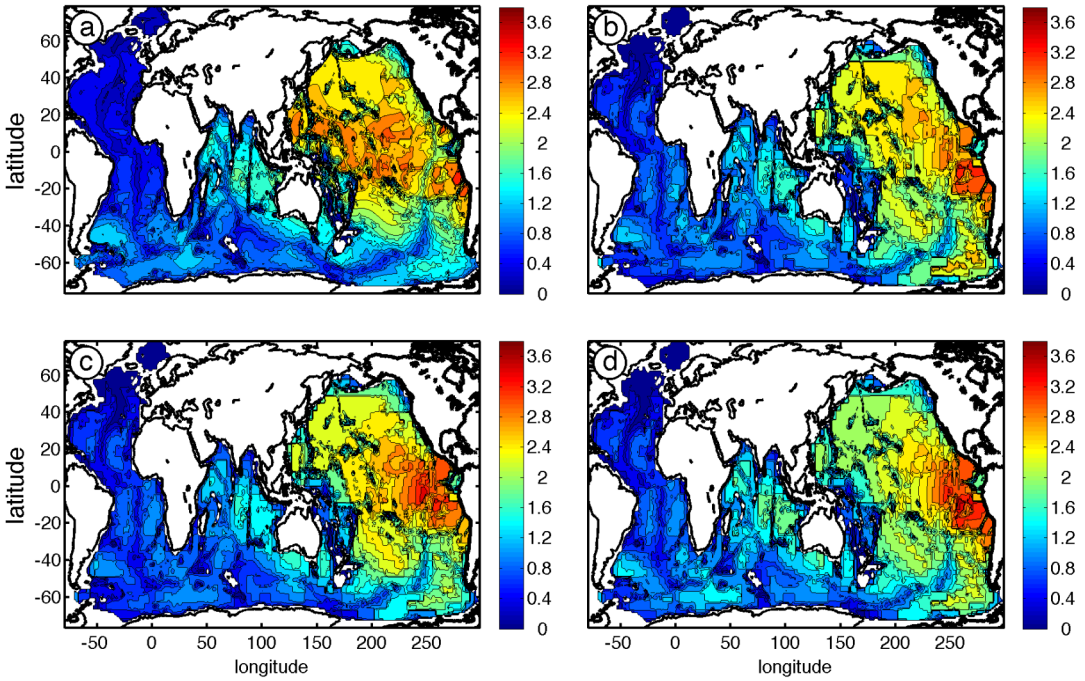


Figure 2.5: Vertical column inventories for non atmospheric ^{3}He for depths greater than 1000 m. Units are nmol/m^{2}. (a) observational estimate. (b-d) HH, P2A and P2 models. Model injection of ^{3}He has been reduced to match the observed deep ocean ^{3}He inventory. The ^{3}He injection is 599, 509 and 473 mol years^{-1} for the HH, P2A and P2 models respectively.

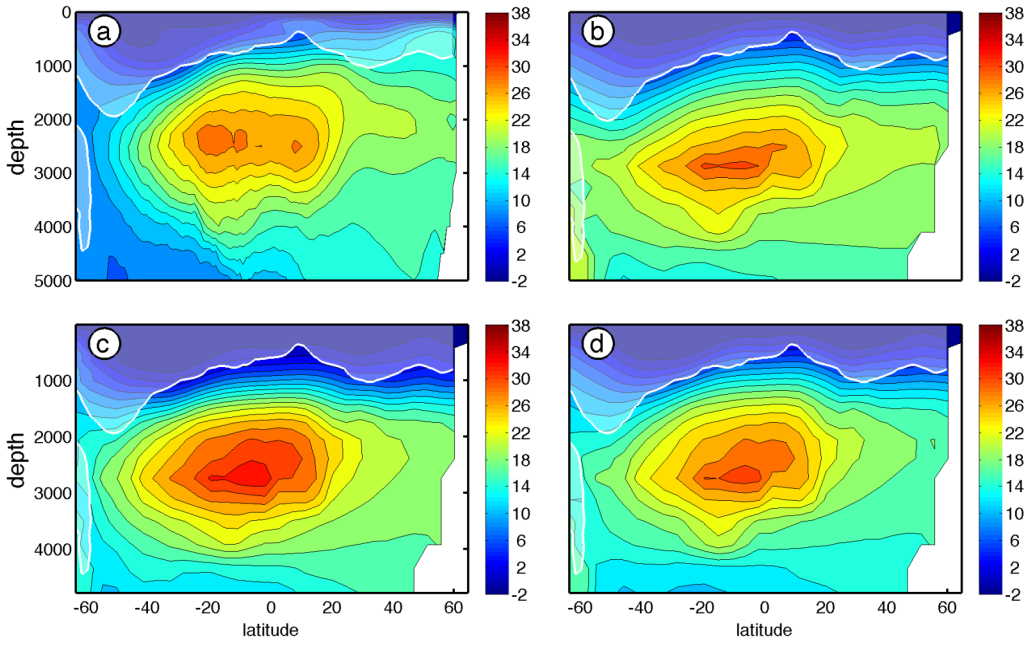


Figure 2.6: Meridional sections of δ^3He distribution (%) in the Pacific Ocean (averaged between 140°E to 80°W). Units are percent. (a) observational dataset. (b-d) HH, P2A and P2 models with ^{3}He injection reduced to match the observed deep ocean ^{3}He inventory. The ^{3}He injection is 599, 509 and 473 mol years^{-1} for the HH, P2A and P2 models respectively. The white-hatched region indicates water masses with CFC-11 concentration higher than 0.1 pmol kg^{-1}, indicating potential contamination due to tritiogenic ^{3}He. The light blue line is the contour line for CFC-11 concentration of 0.1 pmol kg^{-1} from the GLODAP dateset (Key et al., 2004).

Chapter 3: Data-based estimates of suboxia, denitrification and N_2O production in the ocean, and their sensitivities to change

Abstract

Oxygen minimum zones (OMZs) are major sites of fixed nitrogen removal from the open ocean. However, commonly-used gridded data sets such as the World Ocean Atlas (WOA) overestimate oxygen in the suboxic range (O_2<5-10 $mmol\,m^{-3}$) compared to measurements, underestimating OMZs. We evaluate the distribution of the OMZs by (1) mapping high-quality oxygen measurements from the WOCE program, and (2) by applying an empirical correction to the gridded WOA based on in situ observations. The resulting suboxic volumes are a factor 3 larger than in the uncorrected gridded WOA. We combine the new oxygen data sets with estimates of global export and simple models of remineralization to estimate global denitrification and N_2O production. We obtain a removal of fixed nitrogen of 70 ± 50 Tg $year^{-1}$ in the open ocean and 198 ± 64 Tg $year^{-1}$

in the sediments, and a global N_2O production of 6.2 ± 3.2 Tg year^{-1}. Our results (1) reconcile water column denitrification rates based on global oxygen distributions with previous estimates based on nitrogen isotopes, (2) revise existing estimates of sediment denitrification down by 1/3 through the use of spatially-explicit fluxes, and (3) provide independent evidence supporting the idea of a historically-balanced oceanic nitrogen cycle. These estimates are most sensitive to uncertainties in the global export production, the oxygen threshold for suboxic processes, and the efficiency of particle respiration under suboxic conditions. Ocean deoxygenation, an expected response to anthropogenic climate change, could increase denitrification by 14 Tg year^{-1} of nitrogen per 1 mmol m^{-3} of oxygen reduction if uniformly distributed, while leaving N_2O production relatively unchanged.

3.1 Introduction

Nitrogen is a major constituent of living organisms, and a limiting macronutrient over vast regions of the surface ocean. Molecular nitrogen (N_2) is not readily usable by most marine organisms, and must be fixed by specialized prokaryotes before being incorporated into biomass. Nitrogen fixation by autotrophic diazotroph communities is the major oceanic source of biologically available nitrogen in the open ocean. Conversely, denitrification processes in the water column and sediments, including canonical denitrification and annamox, represent the main sink of nitrogen from fixed forms to N_2 (Brandes et al., 2007). The removal of fixed nitrogen in the open ocean is tightly linked to the oceanic oxygen distribution. The activity of denitrifying bacterial communities is strongly inhibited by oxygen concentrations at even a few percent of saturation levels (Codispoti et al, 2001). As a consequence, fixed N losses are observed only in the most oxygen-depleted regions of the open ocean, in the suboxic core of the major oxygen minimum zones (OMZs).

The oxygen distribution further affects the cycling of nitrogen by modulating the production of oceanic nitrous oxide (N_2O). A byproduct of nitrification and denitrification pathways, N_2O is a powerful greenhouse gas that affects the Earth's energy balance and climate. The ocean is responsible for approximately a quarter to a third of the preindustrial flux of N_2O to the atmosphere (Galloway et al., 2004), with estimates between 4 and 10 Tg $year^{-1}$ (Codispoti et al., 2001; Nevison et al., 2003; Galloway et al., 2004,). The production of N_2O during nitrification occurs across a wide

range of oxygen concentrations, and is enhanced at low oxygen levels (Nevison et al., 2003). Additionally, denitrification processes consume N_2O in oxygen-deficient waters. As a result of enhanced production under hypoxic conditions, generally assumed to occur at $O_2 < 60 - 120\ \mathrm{mmol\,m^{-3}}$ (Stramma et al. 2008), and consumption under suboxia ($O_2 < 5 - 10\ \mathrm{mmol\,m^{-3}}$), local minima of N_2O appear at the core of intense OMZs, accompanied by local maxima in the surrounding oxycline regions (Codispoti and Christensen, 1985). Overall, N_2O sources appear to dominate over sinks in low-oxygen waters. As a consequence, open ocean OMZs account for a large share of the oceanic N_2O production (Nevison et al., 2003).

Despite recent developments in our understanding of the quality and magnitude of the pathways that make-up the oceanic nitrogen cycle (see Table 3.1), a number of open questions still remain (Brandes et al., 2007). In particular, disagreement exists as to how close the marine nitrogen cycle is to a balance between N_2 fixation and denitrification, and whether any imbalance can be detected (Codispoti and Christensen, 1985; Gruber and Sarmiento, 1997; Codispoti et al., 2001; Gruber et al., 2004; Codispoti 2007). The major processes that must be considered are the removal of fixed nitrogen due to denitrification and burial in sediments and inputs from N_2 fixation, river run-off and atmospheric deposition. While river runoff and atmospheric deposition are relatively well constrained, major sources of uncertainty center on the magnitude of sedimentary and pelagic denitrification and nitrogen fixation. Some modeling studies suggest sedimentary denitrification as high as 285 to $300\ \mathrm{Tg\,N\,year^{-1}}$ (Middelburg, 1996; Codispoti, 2001; Codispoti, 2007). Other studies propose a sedimentary sink of approximately 180-190

$\mathrm{Tg\,N\,year^{-1}}$ (Galloway et al., 2004; Gruber et al., 2004; Deutsch et al., 2004). Most estimates of pelagic denitrification rely on the biogeochemical interpretation of excess dissolved phosphate (PO_4^{3-}) relative to nitrate (NO_3^-) in the ocean. The range of estimates varies between 65-70 $\mathrm{Tg\,N\,year^{-1}}$ (Gruber, 2004; Deutsch et al., 2004) up to approximately 150 $\mathrm{Tg\,N\,year^{-1}}$ (Codispoti et al., 2001, Codispoti 2007). Major sources of disagreement involve the interpretation of water column N_2 excess measurements, as well as the lack of consensus on the stoichiometry of denitrification reactions (Codispoti et al., 2001). Global nitrogen fixation rates of between 85 and 141 $\mathrm{Tg\,N\,year^{-1}}$ have been proposed based on extrapolation of in situ fixation rates (Galloway et al., 2004), interpretation of observed excess of NO_3^- over PO_4^{3-} and water mass age (Gruber and Sarmiento, 1997; Bange et al., 2000, Deutsch et al., 2001), and combinations of nutrient observations and ocean circulation models (Deutsch et al., 2007). Unfortunately, the large uncertainty associated with the major pelagic sources and sinks of fixed nitrogen seems to hinder any clear conclusion on the balance of the marine nitrogen budget.

In this study we combine global syntheses of organic matter export (Dunne et al., 2007) and new oxygen data sets with simple models for water column and benthic remineralization (Martin et al., 1987; Nevison et al., 2003; Middelburg et al., 1996) to provide an independent estimate of the pelagic and sedimentary denitrification and N_2O production. We place particular emphasis on reducing the uncertainties related to (1) the low-oxygen range of the global oxygen distribution, and (2) the value and range of the parameters that are thought to regulate remineralization processes. Our approach relies on applying a set of algorithms of biogeochemical activity to geographically explicit export

fluxes and oxygen fields, which is similar to what is commonly done in global models of ocean biogeochemistry. Therefore our results have implications for ongoing efforts to develop comprehensive models of the Earth system.

The rest of the chapter is organized as follows. Section 3.2 discusses the particle export and oxygen data sets used for the calculations. Section 3.3 describes the rationale used to parameterize remineralization processes in the water column and sediments. Section 3.4 presents the results of the calculations and the analysis of the sensitivity and errors associated with the data sets and parameters. Section 3.5 discusses the implication of our results and concludes the chapter.

3.2 Data sets used in this study

We employ the global estimate of particulate organic carbon (POC) export from the analysis of Dunne et al., (2007). The flux of POC that sinks out of the euphotic zone is obtained by combining estimates of primary production with an empirical equation for the ratio of POC export to primary production developed by Dunne et al., (2005). Primary production is estimated from the algorithms of Behrenfeld and Falkowski (1997), Carr (2002) and Marra et al., (2003).

We use in situ oxygen measurements from the GLODAP data set (Key et al., 2004) as well as the gridded global oxygen data set of the World Ocean Atlas 2005 (WOA05, Garcia et al., 2006). The GLODAP data set consists of a compilation of high-quality measurements collected mostly during the 1990s by the World Ocean Circulation Experiment. The WOA05 is a gridded data set obtained by merging and interpolating a

large number of measurements from a variety of observational programs from the last decades, including WOCE. WOA05 provides a climatological view of the ocean oxygen distribution, and is extremely valuable for estimating global and basin scale integrated properties and for model-data intercomparisons. However, growing evidence suggests that WOA05 underestimates the volume of suboxic waters in the major OMZs (Fuenzalida et al., 2009). Suboxic processes are generally assumed to dominate at oxygen concentrations below 5 $\mathrm{mmol\,m^{-3}}$ (Morrison et al., 1999; Codispoti et al., 2001; Bange et al., 2004). This is unfortunately near the level of detection, and oxygen biases of the order of just a few $\mathrm{mmol\,m^{-3}}$ have the potential to significantly affect our interpretation of the distribution of suboxic conditions.

We assess the accuracy of the distribution of low-oxygen waters in the gridded WOA05 product by sampling the WOA05 at the location and month of GLODAP measurements. Figure 3.1a shows a scatterplot of all GLODAP measurements versus the sampled WOA05. A scatter of the data around the 1:1 line would be expected due to the interpolation procedure and the larger data set used in the WOA05. However, we find that the gridded data appear to consistently overestimate in situ measurements at low oxygen. This is evident in measurement from all major OMZs. The mean of the oxygen residuals (calculated as difference between gridded and in situ oxygen) is approximately 6.4 $\mathrm{mmol\,m^{-3}}$ in the hypoxic range (0-60 $\mathrm{mmol\,m^{-3}}$), and around 80% of the sampled gridded dataset values overestimate in situ oxygen.

The disagreement between WOA05 and GLODAP may arise from a combination of factors such as: positive biases in early measurements, interpolation artefacts, smoothing during objective mapping, and the effects of variability in ocean circulation.

The measurements included in the WOA05 were obtained with different analytical methods. It is known that early measurements from suboxic waters can be biased high by up to 5 $\mathrm{mmol\,m^{-3}}$ (Codispoti et al., 1985, Naqvi et al., 2010). On the other hand, analytical methods adopted in recent years appear to have biases and precision better than approximately 2 $\mathrm{mmol\,m^{-3}}$ in the suboxic range (Morrison et al., 1999).

In addition to the analytical biases, interpolation techniques can introduce artefacts that can be particularly relevant in low oxygen regions. An interpolated value between undetectable (zero) and detectable (nonzero) will have nonzero oxygen at all intermediate values, whereas contiguous anoxic regions in the ocean can have zero oxygen over significant volumes. Objective mapping procedures tend to further truncate extrema. Therefore, interpolated values may overestimate oxygen near the zero-oxygen limit. Biases can also be related to variability in oxygen records. Observational and model-based studies documented substantial variability in the oxygen content of the ocean on interannual to multi-decadal timescales, resulting from a combination of circulation and biological changes (Garcia et al., 2005; Deutsch et al., 2011). In addition, variability on shorter timescales, for example due to internal wave and eddy activity, can affect the oxygen distribution particularly in the upper ocean. Vertical displacements of isopycnal surfaces in regions of strong oxygen gradients can result in large changes in the oxygen concentrations at a given depth. Variability in regions with large oxygen curvature, for example around oxygen minima, would tend to produce positive biases when averaged to obtain climatological means at fixed depth levels.

To address the biases in the gridded WOA05 in the suboxic and hypoxic ranges, we produced three additional gridded oxygen data sets focusing on the consistency

between mapped and in situ oxygen within the major OMZs. All three methods implicitly assume that temporal variability over the measurement period (recent decades) has been small, and that all data represent a steady mean state. We generated the first two data sets (referred to as *objmap-1* and *objmap-2*) from the in situ GLODAP measurements by using a mapping procedure similar to the one described in Key et al., (2004). We first interpolated the oxygen profiles to 60 neutral density levels between 20 and 28.5 $kg\,m^{-3}$. We followed with a horizontal mapping on a 1° resolution grid, using the objective analysis technique developed by Gandin (1963), as described in Sarmiento et al., (1982) for the dataset *objmap-1*, and the iterative interpolation scheme developed by Barnes (1964) for the dataset *objmap-2*. Finally, we converted the mapped oxygen datasets from neutral density to depth space by using annual mean climatological densities from WOA05. We obtained the third data set by applying an empirical correction to the gridded WOA05 based on in situ GLODAP measurements.

Similar to Key et al., (2004), we adopted two different correlation length scales for the zonal and meridional directions. We adopted constant zonal and meridional length scales of 10 and 20 degrees and 15 and 7 degrees for the *objmap-1* and *objmap-2* datasets respectively. These length scales were chosen among different combinations, and appeared to be best suited to retain the signal from low-oxygen regions while keeping interpolation artifacts acceptably small. The horizontal mapping scheme used to generate the second data set (*objmap-2*) is similar to the one adopted by Garcia et al., (2006) to produce the gridded WOA05. Garcia et al., (2006) adopted a three-iteration scheme with variable correlation length scales, and interpolated a larger number of oxygen measurements averaged by 1° boxes. Our approach uses a smaller sample of the

WOA05measurements, constant correlation length scales, but a higher number (10) of iterations.

The main difference between the mapping procedure adopted in this study and the ones adopted by Key et al., (2004) and Garcia et al., (2006), lies in the choice of neutral density as vertical coordinate for the horizontal maps. A substantial contribution to oxygen variability at a given location and depth on sub-seasonal to interannual timescale is due to vertical and horizontal displacements of density layers due to physical processes ranging from internal waves and eddies to climate-driven variations (Garcia et al., 2005; Deutsch et al., 2011). By choosing neutral density as the vertical coordinate we minimize the effects of density structure changes that would introduce significant oxygen variability in depth space.

For the third data set (*corrected-WOA05*), we apply an empirical correction to the gridded WOA05 oxygen based on in situ measurements from GLODAP. We calculate the corrected oxygen by regressing the GLODAP oxygen onto WOA05 values sampled at the location and month of in situ-measurements, using a linear fit over the full range of oxygen values ($O_2^{corrected} = 1.009\ O_2^{WOA05} - 2.523\ \mathrm{mmol\ m^{-3}}$). This approach allows us to maintain the geographical structure of the gridded WOA05 data set while reducing the biases in the low-oxygen range relative to recent high-quality oxygen measurements.

Figures 3.1b-d shows scatter plots of the oxygen values from the gridded data sets compared to in situ GLODAP measurements. Whereas the WOA05 overestimates in situ measurements in the low-oxygen range, the gridded data sets obtained by objective mapping and by correcting the WOA05 approximate in situ oxygen values to a better degree, and the new datasets scatter more uniformly around the 1:1 lines. Mean oxygen

biases decrease from approximately 6.4 $\mathrm{mmol\,m^{-3}}$ to 3.8 – 4.2 $\mathrm{mmol\,m^{-3}}$. Figures 3.2 and 3.3 show the volumetric distribution of low oxygen waters for the gridded data sets, and the thickness of the suboxic water column ($O_2 < 10\ \mathrm{mmol\,m^{-3}}$). WOA05 shows a substantially lower volume of suboxic waters compared to the new datasets. Relatively more oxygenated waters show similar volumes for all the data sets. The volumes of low oxygen waters from the three main OMZs in the Indian and Pacific Oceans are summarized in Table 3.2. The volume of waters with oxygen below 20 $\mathrm{mmol\,m^{-3}}$ is approximately 1.4 times larger in the new gridded data sets compared to WOA05; the discrepancy increases to about 3 times when water volumes with oxygen below 5 $\mathrm{mmol\,m^{-3}}$ are considered.

The two interpolated data sets generated in this study are in good agreement with each other, but show overall larger suboxic volumes than the corrected WOA05. On a regional basis, the difference is most evident in the South East Tropical Pacific OMZ, where the corrected WOA05 shows a substantially smaller volume of suboxic waters than the data sets obtained by objective analysis. In this region, OMZ volumes from the two objectively mapped datasets are in good agreement with the recent independent assessment by Fuenzalida et al., (2009), based on mapping OMZ upper and lower boundaries. The authors find that the volume of waters with oxygen lower than 20 $\mathrm{mmol\,m^{-3}}$ is between 2.28 and $2.78 \cdot 10^6\ \mathrm{km^3}$, close to our estimate of 2.3 to $2.5 \cdot 10^6\ \mathrm{km^3}$ from the objective mapping results, but somewhat higher than the estimate of $1.9 \cdot 10^6\ \mathrm{km^3}$ from the corrected WOA05.

In concluding, we note that by adopting an interpolation procedure that uses neutral density as a vertical framework we addressed only the variability in oxygen distribution that arises from variability in the density structure of the ocean. Variability related to biological export of organic matter and respiration plays an additional role in controlling seasonal to interannual changes in the position and intensity of OMZ (Deutsch et al., 2011). With the inclusion of high quality measurements from ongoing observational efforts targeted at measuring oxygen near the detection limit within major OMZs, we are optimistic that the biases and uncertainties that characterize current data sets will be further reduced.

3.3 Models of respiration, denitrification and N_2O production

With the revised view of the oxygen distribution in open ocean OMZs, we turn to investigate respiration, denitrification and N_2O production on a global scale. We start from the average estimate of export production from Dunne et al., (2007), and propagate it to the ocean interior by imposing an oxygen-dependent profile of remineralization. We choose the simple and widely used approach of a power law dependence of POC flux with depth, according to the "Martin curve" (Martin et al., 1987):

$$\Phi^{POC}(z) = \Phi_0^{POC}\left(\frac{z}{z_0}\right)^{-b}$$

Here $\Phi^{POC}(z)$ and Φ_0^{POC} are the POC fluxes at depths z and z_0 respectively, and b is the Martin attenuation coefficient. Ocean sinking particles are made up of a heterogeneous mix of mineral and organic components with different physical and chemical properties that spans a continuous spectrum of sizes. The degradation of particles in the water column involves complex and relatively poorly understood physical and biological processes, including dissolution and coalescence, and close interactions with the marine biosphere (Stemman et al., 2004). The Martin curve is based on an empirical fit to observations of POC flux in the open ocean and does not imply any a priori mechanism of particle sinking and degradation. Alternative approaches to the Martin curve have been proposed in recent years, based on mechanistic models of the association of POC with ballast minerals (Armstrong et al., 2002; Klaas and Archer, 2002, Lutz et al., 2002). Dunne et al., (2007) explored a suite of remineralization schemes that include the effect of different ballast fractions, including $CaCO_3$, opal and lithogenic material, and found that adding a ballast component improved the regional patterns of bottom fluxes in the deep ocean compared to observations. While more sophisticated models of particle flux than the Martin curve can be justified on theoretical and observational grounds, they require a larger number of parameters that are poorly constrained, and the use of additional observational data sets to estimate the mineral fractions. Here, we prefer to avoid the additional uncertainty associated with these parameterizations by adopting the simpler empirical Martin curve approach, supported by a large number of observational studies (Berelson, 2001), and we analyze the sensitivity to this reduced set of parameters.

Following Dunne et al., (2007), we assume that the export starts from an average constant depth z_0 = 75 m, a value close to the average 1 % light level usually used as a proxy for the depth of the euphotic zone. Substantial uncertainty exists on the validity of a single remineralization profile for different oceanographic provinces, and on the numerical value of the attenuation coefficient itself (Lutz et al., 2002, Berelson, 2001). A larger number of observations than currently available are needed to detect statistically significant regional variations in particle flux attenuation with depth (Primeau, 2006). However, a growing number of studies show a significant reduction in the attenuation of particulate organic matter fluxes in severely oxygen-depleted regions compared to the rest of the ocean (Devol and Hartnett, 2001, Van Mooy et al., 2002). Early analyses indicated attenuation coefficients in suboxic waters as low as 0.32 (Martin et al., 1987). Recent studies suggest values ranging from $b = 0.36$ to $b = 0.40$ (Harnett and Devol, 2003; Van Mooy et al., 2002).

We adopt a constant attenuation coefficient $b = 0.8$ for oxygenated waters ($O_2 > O_2^{subox}$). This value is smaller than the attenuation coefficient first proposed by Martin et al., (1987) ($b = 0.86$), but is consistent with the synthesis of U.S. JGOFS flux data by Berelson (2001) ($b = 0.82 \pm 0.16$) and with the analysis by Primeau (2006) ($b = 0.70 \pm 0.08$). For suboxic waters ($O_2 < O_2^{subox}$) we reduce the attenuation coefficient to a value $b^{subox} = 0.36$, in agreement with the results by Harnett and Devol (2003) and Van Mooy et al., (2002).

It is not clear at what oxygen concentration the transition to suboxic conditions occurs. Evidence based on the accumulation of nitrite (NO_2^-) suggests that denitrification

is strongest at oxygen concentrations below approximately 2.5 $\mathrm{mmol\,m^{-3}}$ (Morrison et al., 1999; Codispoti et al., 2001; Bulow et al., 2010), whereas the NO_3^- deficit relative to PO_4^{3-} could support values a few $\mathrm{mmol\,m^{-3}}$ higher (Codispoti et al., 2001). Measurements exist suggesting N_2O removal by denitrification at oxygen concentrations up to 40 $\mathrm{mmol\,m^{-3}}$ (Farias et al., 2009). Yet, most evidence indicates that denitrification is strongly inhibited by oxygen concentrations above 5 $\mathrm{mmol\,m^{-3}}$ (Codispoti et al., 2001; Bulow et al., 2010). The occurrence of water column denitrification in the presence of detectable oxygen is puzzling on biochemical and thermodynamical grounds, but could be supported by the existence of anoxic microenvironments within sinking aggregates (Codispoti et al., 2001). In this study, we adopt the value $O_2^{subox} = 4.5\ \mathrm{mmol\,m^{-3}}$, corresponding to approximately 0.1 $\mathrm{ml\,l^{-1}}$, as the threshold for water column denitrification, and we explore the sensitivity to a range of concentration limits. We assume that above the suboxic threshold, respiration uses oxygen as the main oxidant. Furthermore, we assume that below the suboxic limit nitrate becomes the main oxidant, and that nitrogen reduction, including of nitrous oxide, proceeds until molecular nitrogen is formed.

With these assumptions, we calculate the removal of fixed N by denitrification from the convergence of the POC flux within the suboxic water column, assuming a constant stoichiometric ratio $r_{N:C}^{denitr}$. A substantial uncertainty exists in the overall stoichiometry of denitrification. Early studies suggested values for $r_{N:C}^{denitr}$ generally around or below 1. For example, Richards et al., (1965) provide two different denitrification reactions corresponding to $r_{N:C}^{denitr} = 85:106$ and $r_{N:C}^{denitr} = 110:106$ respectively. Higher

values for $r_{N:C}^{denitr}$ have been proposed recently. Van Mooy et al., (2002) suggest $r_{N:C}^{denitr} = 132.4:106$, under the assumption that microbial communities responsible for denitrification preferentially utilize the amino acid component of particles. Here we adopt the stoichiometric ratio $r_{N:C}^{denitr} = 120:106$ of Gruber and Sarmiento (1997).

We estimate the production of nitrous oxide (N_2O) from nitrification, by using the parameterization of Nevison et al., (2003):

$$\frac{\partial N_2O}{\partial t} = \left(\frac{a_1}{O_2} + a_2 \right) \cdot r_{N:C}^{nitrif} \cdot \frac{\partial \Phi^{POC}}{\partial z}$$

Following Nevison et al., (2003), $a_1 = 0.26 \frac{\text{mol } N_2O}{\text{mol N} \cdot \text{mmol } O_2\, \text{m}^{-3}}$, $a_2 = -0.0006 \frac{\text{mol } N_2O}{\text{mol N}}$, $r_{N:C}^{nitrif} = 16:106$. As noted in the introduction, N_2O is an obligate intermediate of denitrification reactions, and is further utilized as the oxidant as denitrification proceeds to reduce nitrogen to the molecular form. It is well established that denitrification in suboxic waters represent a sink of N_2O (Codispoti and Christensen, 1985; Surantharaligam and Sarmiento, 2000). The magnitude of the sink for N_2O produced outside the suboxic region ultimately depends on the exact sensitivity of nitrification and denitrification to the oxygen concentration, and on the magnitude of N_2O fluxes across strong N_2O and O_2 gradients. Due to these uncertainties, we adopt the approach of Nevison et al., (2003) and set the N_2O production term to zero below the suboxic threshold O_2^{subox}.

We assess sedimentary denitrification by applying the metamodel developed by Middleburg et al., (1996). The metamodel is based on a mechanistic diagenetic model of

benthic biogeochemical processes calibrated against global observations, and predicts benthic denitrification as a function of the POC flux at the sediment-water interface. According to the metamodel, sediment denitrification ($\mathrm{Den}_{\mathrm{sed}}$) can be calculated from:

$$\log_{10}\left(\mathrm{Den}_{\mathrm{sed}}\right) = 0.0457 + 0.7662 \cdot \log_{10}\left(\frac{\Phi_{\mathrm{bot\,tom}}^{\mathrm{POC}}}{10}\right) - 0.2350 \cdot \log_{10}\left(\frac{\Phi_{\mathrm{bot\,tom}}^{\mathrm{POC}}}{10}\right)^{2}$$

where $\Phi_{\mathrm{bot\,tom}}^{\mathrm{POC}}$ is the flux of particulate organic carbon ($\mathrm{mmol\,C\ m^{-2} d^{-1}}$) to the sediments.

A summary of the numerical values for the model parameters and the associated uncertainties is presented in Table 4.

3.4 Results

3.4.1 Global and regional estimates

Figures 4.a-d show maps of export, vertically integrated pelagic denitrification, benthic denitrification and vertically integrated N_2O production. Regional and global integrals are summarized in Table 3. The uncertainty was estimated by running a Monte Carlo type sensitivity analysis. Approximately 10,000 sets of parameters were randomly selected assuming a gamma distribution (to prevent non-physical negative values) with mean and standard deviations from the literature (Table 4). The globally integrated POC export from Dunne et al., (2007) is 9.4 ± 3.5 $\mathrm{Pg\,C\,year^{-1}}$. Approximately 7.2 ± 2.7 $\mathrm{Pg\,C\,year^{-1}}$, 77 % of export, is respired in the water column. The remaining 2.2 ± 0.8 $\mathrm{Pg\,C\,year^{-1}}$, reaches the seafloor and is mostly respired in the sediments; only a small part is eventually buried (Dunne et al., 2007). Due to a combination of high productivity and

export, and more limited water column remineralization, shallow depths dominate sedimentary fluxes. Approximately 70% of the POC sedimentation (1.5 $Pg\,C\,year^{-1}$) takes place in shelf regions (defined operationally as bottom depths shallower than 150 m).

We obtain a global N_2O production of 6.2 ± 3.2 $Tg\,N\,year^{-1}$, in agreement with the estimate of 5.8 ± 2.0 $Tg\,N\,year^{-1}$ by Nevison et al., (2003). N_2O sources correlate strongly with the patterns of export production and water column respiration, reflecting N_2O formation as a byproduct of nitrification. N_2O production is further modulated by the oxygen distribution, as evident in the regional estimates in Table 3.

The impact of oxygen distribution on open ocean denitrification is even more dramatic. Our results indicate significant denitrification in the cores of the Pacific and Indian Ocean OMZs, with a global pelagic denitrification of 70 ± 50 $Tg\,N\,year^{-1}$, in agreement with the global estimates of 65 and 70 $Tg\,N\,year^{-1}$ by Gruber (2004) and Deutsch et al., (2004), but about half the 150 $Tg\,N\,year^{-1}$ proposed by Codispoti et al., (2001). The Indian Ocean shows a large fixed nitrogen sink, and is responsible for about 31 $Tg\,N\,year^{-1}$ denitrification, in line with 21 to 34 $Tg\,N\,year^{-1}$ reported by Bange et al., (2005) and 21 ± 7 $Tg\,N\,year^{-1}$ by Howell et al., (1997), but slightly below the estimates of 39 ± 13 and 41 ± 18 $Tg\,N\,year^{-1}$ by Bulow et al., (2010) and Devol et al., (2006). Pelagic denitrification in the Pacific Ocean is 39.1 $Tg\,N\,year^{-1}$, with the Northern and Southern Eastern Tropical Pacific (NETP and SETP) regions accounting for 21.5 and 17.6 $Tg\,N\,year^{-1}$ respectively. The fixed nitrogen sink in the NETP and SETP is similar to the estimates of 22 and 26 $Tg\,N\,year^{-1}$ by Deutsch et al., (2001). We do not see

significant pelagic denitrification in the Atlantic Ocean, where oxygen concentrations are above the suboxic limit almost everywhere in open waters.

While the estimates of open ocean respiration and N_2O production appear particularly robust across the different oxygen data sets used in this study, some discrepancies can be found in the estimates of pelagic denitrification. The corrected WOA05 produces the smallest estimate (approximately 51 $\mathrm{Tg\,N\,year^{-1}}$). The data sets from objective mapping of GLODAP measurement with the Key et al., (2004) and Barnes (1964) schemes (*objmap-1* and *objmap-2*) produce around 72 and 87 $\mathrm{Tg\,N\,year^{-1}}$ respectively. Differences in global open ocean denitrification arise from a combination of different suboxic water volumes (Table 2), and location in the three data sets.

Overall, our analysis stresses the critical importance of capturing the lowest range of the oxygen distribution for estimating pelagic denitrification. When we perform our calculations without correcting the gridded WOA05 for the biases in the suboxic range, we obtain less than 24 $\mathrm{Tg\,N\,year^{-1}}$ of global open ocean denitrification. The denitrification is even smaller if the annual climatological WOA05 dataset is used instead of monthly climatologies (denitrification < 5 $\mathrm{Tg\,N\,year^{-1}}$) due to the biases introduced by time averaging in the low-oxygen regions. In contrast, N_2O production shows a minimal sensitivity to the oxygen data set used, even when the original WOA05 data set is used.

We obtain a global estimate of 198 ± 64 $\mathrm{Tg\,N\,year^{-1}}$ for sedimentary denitrification. The largest share of benthic denitrification occurs in shallow regions, where the POC sedimentary flux is highest. Figures 3.5a-b show the cumulative depth distribution of sedimentary denitrification broken down by basin. Our global estimate of

benthic denitrification is smaller than the estimate by Middleburg et al., (1996), 230-285 $\mathrm{Tg\,N\,year^{-1}}$, with most of the difference originating from deep-ocean regions. Middleburg et al., (1996) obtain approximately 100 $\mathrm{Tg\,N\,year^{-1}}$ denitrification in shelf sediments, similar to our estimate of 124 $\mathrm{Tg\,N\,year^{-1}}$ (Table 3.3). The disagreement is due to a combination of factors. Middleburg et al., (1996) calculate sedimentary POC fluxes as a function of depth alone, whereas we employ a geographically varying dataset based on satellite observations, combined with a model of water column remineralization. The globally integrated sedimentary POC flux from Middleburg et al., (1996) is approximately 3 $\mathrm{Pg\,C\,year^{-1}}$, compared to our estimate of approximately 2 $\mathrm{Pg\,C\,year^{-1}}$. The depth-dependent organic carbon flux parameterization adopted by Middleburg et al., (1996), results in the same sedimentation rate in geographically distant provinces such as continental slopes and mid-depth regions away from continental margins. This is unjustified in the light of the satellite export estimates (Figure 3.4a) and sediment data syntheses (Dunne et al., 2007).

Recent studies pointed out that the model by Middleburg et al., (1996) might overestimate denitrification in coastal and shallow environments (Fennel et al., 2009). Differences could arise from the lack of processes such as sediment transport, re-suspension and respiration in Middleburg et al., (1996)'s model. Additional differences may relate to the lack of explicit representation of riverine organic matter inputs to costal waters. Our denitrification estimate for the North Atlantic shelf (29 $\mathrm{Tg\,N\,year^{-1}}$ for depths shallower than 200 m) is larger than the estimate of 20 $\mathrm{Tg\,N\,year^{-1}}$ by Seitzinger and Giblin (1996), derived from the correlation between benthic denitrification and

water-sediment oxygen fluxes, but is in line with the model assessment of 32.2 $\mathrm{Tg\,N\,year^{-1}}$ by Fennel et al., (2006), which is based on the same oxygen-denitrification relationship. Yet, on a global scale, we obtain less denitrification in the shelves than the 250 $\mathrm{Tg\,N\,year^{-1}}$ proposed by Seitzinger et al., (2006). These persistent differences highlight the difficulty of narrowing the uncertainty to better than ± 30 %, given the available constraints.

3.4.2 Sensitivity and error estimates

The relative simplicity of the remineralization scheme adopted in this study allows us to perform an extensive analysis of the sensitivity of remineralization and N_2O production to the model parameters. We run our remineralization scheme by varying one parameter at a time across a range of values inferred from the literature, while fixing the other parameters to their control values. The sensitivities are calculated as partial derivatives of the globally integrated quantities with respect to the parameter considered. We average the results from the three gridded oxygen data sets to obtain the sensitivities summarized in Table 3.4. Figure 3.6 shows the relative sensitivities of the global estimates of denitrification and N_2O production to changes in the model parameters equal to one standard deviation.

The global export of POC from the surface is the main driver of oceanic remineralization. Changes in Φ_0^{POC} affect pelagic denitrification and N_2O production in a linear way. The depth of export (z_0) is the second factor controlling the flux of POC entering the ocean interior. An increase in z_0 shifts respiration deeper in the water

column and enhances sedimentary fluxes and benthic denitrification. At the same time, water column denitrification and N_2O production increase due to the larger respiration in the subsurface hypoxic and suboxic layers.

In the interior, POC fluxes are controlled by the shape of the Martin curve. An increase in the attenuation coefficient b steepens the remineralization curve and moves respiration shallower. More POC is respired between the surface and the suboxic layers, and less reaches the denitrification region in the core of OMZs, as well as the sediments. The opposite is true for an increase in b^{subox}, which acts to enhance the degradation of POC within the suboxic layers, enhancing water column denitrification.

The suboxic threshold O_2^{subox} has a strong influence on water column denitrification. The impact is less marked on N_2O production, and negligible on sedimentary processes. As O_2^{subox} increases, suboxic waters expand both in area and thickness, enhancing denitrification. We observe an approximately linear dependence of total denitrification on O_2^{subox}, with a sensitivity of 14.4 $\mathrm{Tg\,N\,year^{-1}\,(mmol\,m^{-3})^{-1}}$.

By design, N_2O production shows a non-linear dependence on O_2^{subox}, with a strong intensification for lower values of O_2^{subox} (Nevison et al., 2003). This is related to the inverse dependence of N_2O sources on oxygen concentration. N_2O production increases by approximately 2.3 $\mathrm{Tg\,N\,year^{-1}}$ when O_2^{subox} is reduced from 10 to 2 $\mathrm{mmol\,m^{-3}}$, and by additional 1.7 $\mathrm{Tg\,N\,year^{-1}}$ when O_2^{subox} is reduced between 2 and 0.5 $\mathrm{mmol\,m^{-3}}$. This suggests that the oxygen concentration at which denitrification becomes a dominant sink for N_2O is an important factor controlling the overall N_2O source in the

ocean. Additional uncertainty (~1.7 $\mathrm{Tg\,N\,year^{-1}}$) is associated with the variability of the coefficient a_1 in the parameterization by Nevison et al., (2003).

The contributions of each model parameter to the errors in the final estimates can be obtained by combining the sensitivities with the uncertainties in Table 3.4. After the uncertainties associated with the global POC export, uncertainties in the parameters controlling suboxic processes, O_2^{subox} and b^{subox}, dominate the picture.

3.4.3 Sensitivity to the oxygen state of the ocean

The hypothesis that anthropogenic climate change could lead to a decrease in the ocean oxygen due to ocean warming and increased stratification has been gaining substantial attention over the last decade (Sarmiento et al., 1998; Keeling et al., 2010). Modeling studies predict average global ocean deoxygenation between 2 and 12 $\mathrm{mmol\,m^{-3}}$ over the next century (Keeling et al., 2010). However, recent studies suggest different responses for hypoxic and suboxic waters. While hypoxic volumes are projected to expand, suboxic volumes might in fact decrease (Frölicher et al., 2009; Gnanadesikan et al., 2011). In addition to model results, recent observational syntheses indicate an expansion of major OMZs in the Atlantic and Pacific Ocean during the past 50 years, above the fluctuations of decadal variability (Stramma et al., 2008). Changes in the oxygen content of the ocean and in the extent of OMZs such as the ones recently suggested could have significant impacts on the oceanic nitrogen and carbon cycles and on marine ecosystems.

We investigate the first order effect of changes in the oxygen state of the ocean on water column denitrification and N_2O production by imposing a uniform change in the oxygen distribution (ΔO_2). This approximates a uniform warming or cooling of the ocean, with no change in circulation or ecosystem behavior. The sensitivities to ΔO_2 are shown in Figure 3.7a-b and summarized in Table 3.4. The sharp transition between fully oxic and suboxic conditions at $\Delta O_2 = O_2^{subox}$ results in the reduction of open ocean denitrification to near zero for oxygen increase above O_2^{subox}. Our model shows a nearly linear effect of oxygen changes on open ocean denitrification (Figure 3.7a), with sensitivities between -12 and -14 Tg year^{-1}(mmol m^{-3})$^{-1}$ for $\Delta O_2 < 4$ mmol m^{-3}. The effects of a uniform oxygen decrease on N_2O production are negligible (Figure 3.7b). This is due to two factors. First, our model assumes no net production of N_2O within suboxic waters ($O_2 < O_2^{subox}$). Second, the volume of hypoxic waters increase approximately linearly above the suboxic threshold. Therefore, a uniform decrease in oxygen acts to shift the location of N_2O sources, without altering the relative contribution of waters with different oxygen content. For oxygen changes above 4 mmol m^{-3}, N_2O production starts decreasing at a rate between 0.3 and 0.2 Tg N year^{-1}(mmol m^{-3})$^{-1}$, reflecting the overall reduction of hypoxic waters.

It is important to note that changes in oxygen distribution are unlikely to be geographically uniform as assumed in this sensitivity analysis, and additional physical, biogeochemical and ecological processes (e.g. changes in circulation and productivity, feedbacks between denitrification, nitrogen fixation and export production) are likely to

complicate the response of the nitrogen cycle to oxygen changes (Keeling et al., 2010, Frölicher et al., 2009; Gnanadesikan et al., 2011).

3.5 Discussion and conclusions

Substantial uncertainty still exists regarding the extent of open-ocean OMZs and their impact on nitrogen cycling. We showed that widely used gridded data sets of oxygen distribution have biases in the low oxygen range that lead to an underestimate of the extent of suboxic conditions in the ocean. We account for these biases by generating three data-based gridded maps that combine WOCE era oxygen measurements to produce an updated view of OMZs in line with recent independent estimates. The new gridded maps are used in conjunction with spatially explicit estimates of export production and a simple model of water column remineralization to estimate global denitrification and N_2O production.

We obtain 70 ± 50 $\mathrm{Tg\,N\,year^{-1}}$ of denitrification in the open ocean and 198 ± 64 $\mathrm{Tg\,N\,year^{-1}}$ in the sediments. These values are compatible with the isotopic constraints placed on the ratio of non-fractionating (sedimentary) to fractionating (water column) oceanic denitrification processes (Brandes and Devol, 2002), corrected for the dilution effect of Deutsch et al., (2004). The ratio implied by our estimates, 2.8, is consistent with the value of approximately 2.7 proposed by Deutsch et al., (2004). Our results are close to the lower range of existing estimates in the open ocean (Gruber, 2004; Galloway et al., 2004), and revise the benthic denitrification proposed by Middelburg et al., (1996) down by 1/3 through the use of spatially varying sediment fluxes. Taken together, our estimates

provide independent evidence supporting the idea of a historically-balanced oceanic nitrogen cycle (Gruber, 2004). The N_2O production estimate, 6.2 ± 3.2 $Tg\,N\,year^{-1}$, is in agreement with previous studies, and appears robust with respect to the model parameterizations and oxygen data sets. A sensitivity analysis shows that ocean deoxygenation, could lead to an increase in denitrification of approximately 14 $Tg\,N\,year^{-1}$ per $mmol\,m^{-3}$ of oxygen decrease, while leaving N_2O production relatively unchanged.

The uncertainty in our estimate originates from uncertainties in the export production and oxygen data sets and in the parameterizations of remineralization processes. An accurate depiction of the suboxic range of oceanic oxygen is critical for capturing the magnitude and distribution of water column denitrification, as biases of a few $mmol\,m^{-3}$ can significantly impact the final estimates. There are additional sources of error that we did not directly address in this study. Among others, uncertainty could arise from climate variability in export production and oxygen distribution, and biogeochemical processes such as cycling of dissolved organic matter, active transport by vertically migrating zooplankton, and feedbacks between denitrification, nitrogen fixation and particle export.

The method used in this study relies on propagating the satellite-derived export production from the euphotic zone into the ocean interior using a simple scheme of particle remineralization. Our remineralization parameterization is similar to that used in the current generation of ocean biogeochemistry models. The uncertainties identified in this study show that it is critical that models capture the extent, location, intensity and variability of the major suboxic regions, a challenging task that will require accurate

observations and simulations of both circulation and biogeochemistry of OMZs. Particular attention should be placed on reliable representations of organic matter respiration under hypoxia and suboxia. To this end, we need to expand our quantitative understanding of the biogeochemical processes and thresholds that characterize the transition between oxic, hypoxic and suboxic regimes in the water column. We urge the development of global data sets of oceanic oxygen that focus on the faithful representation of the suboxic range. This will require assembling high quality measurements from the major OMZs and applying mapping procedures that reduce interpolation artifacts to a minimum.

3.6 References

Anderson, L. A., and Sarmiento, J. L., 1994. Redfield ratios of remineralization determined by nutrient data analysis, *Global Biogeochem. Cycles,* 8, 65-80.

Anderson, W., Gnanadesikan, A., Hallberg, R., 2009. Regional impacts of ocean color on tropical Pacific variability, *Ocean Sci.,* 5, 313-327.

Armstrong, R. A., Lee, C. , Hedges, J. I., Honjo, S., Wakeham, S. G., 2002. A new, mechanistic model for organic carbon fluxes in the ocean based on the quantitative association of POC with ballast minerals, *Deep-Sea Res. II,* 49, 219-236.

Bange, H. W., Naqvi, S. W. A., Codispoti, L. A., 2005. The nitrogen cycle in the Arabian Sea, *Prog. Ocean.*, 65, 145-158.

Barnes, S. L., 1964. A technique for maximizing details in numerical weather map analysis, *J. App. Meteor* ., 3, 396-409.

Berelson, W. M., 2001. The flux of particulate organic carbon into the ocean interior: A comparison of four U.S. JGOFS regional studies, *Oceanography,* 14, 59-67.

Brandes, J. A., and Devol, A. H., 2002. A global marine-fixed nitrogen isotopic budget: Implications for Holocene nitrogen cycling, *Glob. Biogeochem. Cycles,* 16, doi:10.1029/2001GB001856.

Brandes, J. A., Devol, A. H., Deutsch, C. A., 2007. New developments in the marine nitrogen cycle, *Chem. Rev*., 107, 577–589.

Bulow, S. E., Rich, J. J., Naik, H. S., Pratihary, A. K., Ward, B., 2010. Denitrification exceeds anammox as a nitrogen loss pathway in the Arabian Sea oxygen minimum zone, *Deep-Sea Res., I* 57, 384-393.

Codispoti, L.A., 2007. An oceanic fixed nitrogen sink exceeding 400 Tg N a^{-1} vs. the concept of homeostasis in the fixed-nitrogen inventory, *Biogeosci*., 4, 233-253.

Codispoti, L. A., and Christensen, J. P., 1985. Nitrification, denitrification and nitrous oxide cycling in the eastern tropical South Pacific Ocean, *Mar. Chem.,* 16, 277–300.

Codispoti, L. A., Brandes, J. A., Christensen, J. P., Devol, A. H., Naqvi, S. W. A., Paerl, H. W., Yoshinari, T., 2001. The oceanic fixed nitrogen and nitrous oxide budgets: Moving targets as we enter the Anthropocene?, *Sci. Mar.,* 65, 85–105.

Deutsch, C., Gruber, N., Key, R. M., Sarmiento, J. L., Ganaschaud, A., 2001. Denitrification and N_2 fixation in the Pacific Ocean, *Global Biogeochem. Cycles,* 15, 483–506.

Deutsch, C., Sigman, D. M., Thunell, T., Meckler, A. N., Haug, G. H., 2004. Isotopic constraints on glacial/interglacial changes in the oceanic nitrogen budget, *Global Biogeochem. Cycles,* 18.

Deutsch, C., Sarmiento, J. L., Sigman, D. M., Gruber, N., Dunne, J. P., 2007. Spatial coupling of nitrogen inputs and losses in the ocean, *Nature,* 445, 163–67, 2007.

Deutsch, C., Brix, H. , Ito, T., Frenzel., H., Thompson, L., 2011. Climate-forced variability of ocean hypoxia, *Science,* 333, 336-339.

Devol A. H., Hartnett, H. E., 2011. Role of the oxygen-deficientzone in transferof organiccarbonto the deep ocean, *Limnol. Oceanogr.*, 46(7), 1684-1690.

Devol, A. H., Uhlenhopp, A. G. , Naqvi, S. W. A., Brandes, J. A., Jayakumar, D. A., Kaik, H., Gaurin, S., Codispoti, L. A., Yoshinari, T., 2006. Denitrification rates and excess nitrogen gas concentrations in the Arabian Sea oxygen deficient zone, *Deep Sea Research I,* 53, 1533–1547.

Dunne, J. P., Armstrong, R. A., Gnanadesikan, A., Sarmiento, J. L., 2005. Empirical and mechanistic models for the particle export ratio, *Global Biogeochem. Cycles,* 19, GB4026, doi:10.1029/2004GB002390.

Dunne, J. P., Sarmiento, J. L., Gnanadesikan, A., 2007. A synthesis of global particle export from the surface ocean and cycling through the ocean interior and on the seafloor, *Global Biogeochem. Cycles*, 21, GB4006, doi:10.1029/2006GB002907.

Farias, L., Castro-Gonzalez, M., Cornejo, M., Charpentier, J., Faundez, J., 2009. Denitrification and nitrous oxide cycling within the upper oxycline of the eastern tropical South Pacific oxygen minimum zone, *Limn. Ocean.,* 54, 132–144.

Fennel, K., Wilkin, J, Levin, J., Moisan, J., O'Reilly, J., Haidvogel, D., 2006. Nitrogen cycling in the Middle Atlantic Bight: results from a three-dimensional model and implications for the North Atlantic nitrogen budget, *Global Biogeochem. Cycles*, 20.

Fennel, K., Brady, D., Di Toro, D., Fulweiler, R. W., Gardner, W. S., Giblin, A., McCarthy, M. J., Rao, A., Seitzinger, S., Thouvenot-Korppoo, M., Tobias, C., 2009. Modeling denitrification in aquatic sediments, *Biogeochemistry,* 93, 159–178.

Frölicher, T. L., Joos, F., Plattner, G.- K., Steinacher, M., Doney, S. C., 2009. Natural variability and anthropogenic trends in oceanic oxygen in a coupled carbon cycle–climate model ensemble, *Global Biogeochem. Cycles*, 23, GB1003, doi:10.1029/2008GB003316.

Fuenzalida, R., Schneider, W., Garcés-Vargas, J., Bravo, L., Lange, C., 2009. Vertical and horizontal extension of the oxygen minimum zone in the eastern South Pacific Ocean, *Deep-Sea Research II,* 56, 992-1003.

Galloway, J. N., Dentener, F. J. , Capone, D., Boyer, E. W., Howarth, R. W., Seitzinger, S. P., Asner, G. P., Cleveland, C. C., Green, P. A., Holland, E. A., Karl, D. M., Michaels, A. F., Porter, J. H., Townsend, A. R., Vorosmarty, C. J., 2004. Nitrogen cycles: past, present and future, *Biogeochemistry*, 70, 153–226.

Gandin, L. S., 1963. Objective Analysis of Meteorological Fields, 286 pp., Hydrometeoizdat, St. Petersburg, Russia.

Garcia, H. E., Boyer, T. P., Levitus, S., Locarnini, R. A., Antonov, J. I., 2005. On the variability of dissolved oxygen and apparent oxygen utilization content for the upper world ocean: 1955 to 1998, *Geophys. Res. Lett.*, doi:10.1029/2004GL021745.

Garcia, H. E., Locarnini, R. A., Boyer, T. P., Antonov, J. I., 2006. World Ocean Atlas 2005, Volume 3: Dissolved oxygen, apparent oxygen utilization, and oxygen saturation, S. Levitus, Ed. NOAA Atlas NESDIS 63, U.S. Government Printing Office, Washington, D.C., 342 pp.

Gruber, N., 2008. The marine nitrogen cycle: Overview of distributions and processes, In: *Nitrogen in the marine environment*, 2nd edition, edited by D. G. Capone, D. A. Bronk, M. R. Mulholland, and E. J. Carpenter, Elsevier, Amsterdam, 1-50.

Gruber, N., Sarmiento, J. L., 1997. Global patterns of marine nitrogen fixation and denitrification, *Global Biogeochem. Cycles*, 11, 235–266.

Gruber, N., Friedlingstein, P., Field, C. B., Valentini, R., Heimann, M., Richey, J. E., Romero-Lankao, P., Schulze, D., Chen, C.-T.A., 2004. The vulnerability of the carbon cycle in the 21st century: An assessment of carbon-climate-human interactions, In: *The Global Carbon Cycle: Integrating Humans, Climate, and the Natural World*, Eds: C. B. Field and M. R. Raupach, Island Press, Washington, D.C., 45-76.

Hartnett, H., Devol, A., 2003, Role of a strong oxygen-deficient zone in the preservation and degradation of organic matter: A carbon budget for the continental margins of

northwest Mexico and Washington State, *Geochimica and Cosmochimica Acta* 67, 247-264.

Howell, E.A., Doney, S. C., Fine, R. A., Olson, D. B., 1997. Geochemical estimates of denitrification in the Arabian Sea and Bay of Bengal during WOCE, *Geophysical Research Letters* 24, 2549.

Keeling, R. F., Kortzinger, A., Gruber, N., 2010. Ocean deoxygenation in a warming world, *Annu. Rev. Mar. Sci*., 2, 463–493.

Key, R. M., Kozyr, A., Sabine, C. L., Lee, K., Wanninkhof, R., Bullister, J. L., Feely, R. A., Millero, F.J., Mordy, C., Peng, T.-H. 2004. A global ocean carbon climatology: results from Global Data Analysis Project (GLODAP), *Global Biogeochem. Cycles,* 18, GB4031. doi:10.1029/2004GB002247.

Klaas, C. and Archer, D., 2002. Association of sinking organic matter with various types of mineral ballast in the deep sea: Implications for the rain ratio, *Global Biogeochem. Cycles*, 16(4), 1116, doi:10.1029/2001GB001765.

Lutz, M., Dunbar, R., Caldeira, K., 2002. Regional variability in the vertical flux of particulate organic carbon in the ocean interior, *Global Biogeochem. Cycles*, 16(3), 1037, doi:10.1029/2000GB001383.

Martin, J. H., Knauer, G. A., Karl, D. M., Broenkow, W. W., 1987. VERTEX: carbon cycling in the northeast Pacific. *Deep-Sea research*, 34, 267-285.

Middelburg, J. J., Soetaert, K., Herman, P. M. J., Heip, C., 1996. Denitrification in marine sediments: a model study, *Global Biogeochem. Cycles*, 10, 661–673.

Morrison, J. M., Codispoti, L. A., Smith, S. L., Wishner, K., Flagg, C., Gardner, W. D., Gaurin, S., Naqvi, S. W. A., Manghnani, V., Prosperie, L., Gundersen, J. S., 1999. The oxygen minimum zone in the Arabian Sea during 1995, *Deep Sea Res. II,* 46, 1903–1931.

Naqvi, S. A., Banse, K., Narvekar, P. V., Postel, J. R., 2010. Are the open-ocean Oxygen Minimum Zones intensifying and expanding?, Proceedings from the 2010 AGU Ocean Sciences Meeting, Portland, OR (USA), 22-26.

Nevison, C., Buttler, J. H., Elkins, J. W., 2003. Global distribution of N_2O and the DN2O-AOU yield in the subsurface ocean, *Global Biogeochem. Cycles*, 17, 1119, doi:10.1029/2003GB002068.

Primeau, F., 2006. On the variability of the exponent in the power law depth dependence of POC flux estimated from sediment traps, *Deep-Sea Res.* I, 53, 1335–1343.

Richards, F.A, 1965. Anoxic basins and fjords, In: *Chemical Oceanography*, eds. Riley J.P., Skirrow G., Academic, New York, 611–645, 1965.

Sarmiento, J. L., Willebrand, J., Hellerman, S., 1982. Objective analysis of tritium observations in the Atlantic Ocean during 1971–1974, Tech. Rep. 1, 19 pp., Ocean Tracer Lab., Princeton, NJ.

Sarmiento J. L, Hughes, T. M. C., Stouffer, R. J., Manabe, S., 1998. Simulated response of the ocean carbon cycle to anthropogenic climate warming, *Nature,* 393:245–49.

Seitzinger, S. P. and Giblin, A. E., 1996. Estimating denitrification in North Atlantic continental shelf sediments, *Biogeochemistry,* 35, 235-260.

Seitzinger, S. P., Harrison, J. A., Bohlke, J. K., Bouwman, A. F., Lowrance, R., Peterson, B., Tobias, C., Van Drecht, G., 2006. Denitrification across landscapes and waterscapes: a synthesis, *Ecol. Appl.,* 16(6), 2064–2090.

Stemman, L., Jackson, G. A., Ianson, D., 2004. A vertical model of particle size distributions and fluxes in the midwater column that includes biological and physical processes—Part I: model formulation, *Deep-Sea Res. I*, 51: 865–884.

Stramma L., Johnson, G. C., Sprintall, J., Mohrholz, V. 2008. Expanding oxygen-minimum zones in the tropical oceans, *Science,* 320:655–58.

Suntharalingam, P., Sarmiento, J. L., 2000. Factors governing the oceanic nitrous oxide distribution: Simulations with an ocean general circulation model, *Global Biogeochem. Cycles,* 14(1), 429–454.

Van Mooy, B. A. S., Keil, R. G., Devol, A. H., 2002. Impact of suboxia on sinking particulate organic carbon: Enhanced carbon flux and preferential degradation of amino acids via denitrification, *Geochim. Cosmochim. Acta,* 66, 457–65.

Table 3.1: Estimates of oceanic nitrogen budgets ($Tg\,N\,year^{-1}$)

	Galloway et al., (2004)	Codispoti (2007)	Gruber (2008)	This study
Pelagic and benthic fixation	121	135	135 ± 50	
River input	48	76	80 ± 15	
Atmospheric deposition	33	30	50 ± 20	
TOTAL SOURCES	202	241	265 ± 55	
Sediment denitrification	206	300	180 ± 50	198 ± 64
Pelagic denitrification	116	150	65 ± 20	70 ± 50
Burial	16	25	25 ± 10	
N_2O production	4	6	4 ± 2	6.2 ± 3.2
TOTAL SINKS	342	481	275 ± 55	
TOTAL BUDGET	-140	-240	-10 ± 80	

Table 3.2: Volume (10^6 km^3) of suboxic waters for the major OMZs in the Indian and Pacific Oceans for two oxygen limits (20 and 5 $mmol\,m^{-3}$). The data sets shown are: gridded WOA05; GLODAP data mapped using the procedure described in Gandin (1963); GLODAP data mapped using the procedure described in Barnes (1994); gridded WOA05 with an empirical linear correction based on GLODAP in situ measurements.

		North Pacific	South Pacific	Indian Ocean	Global
WOA05	O_2<20 $mmol\,m^{-3}$	8.8	1.5	2.6	12.9
Objective mapping 1		11.6	2.3	3.4	17.3
Objective mapping 2		12.0	2.5	3.6	18.1
Corrected WOA05		12.0	1.9	3.2	17.1
WOA05	O2<5 $mmol\,m^{-3}$	0.67	0.04	0.34	1.05
Objective mapping 1		2.37	0.45	0.86	3.68
Objective mapping 2		2.41	0.61	1.11	4.13
Corrected WOA05		1.64	0.13	0.68	2.45

Table 3.3: Regional and global estimates of POC flux to the sediments, pelagic denitrification, benthic denitrification (shelf values for z<150 m in parentheses) and N_2O production. Results are averages obtained by using three oxygen data sets discussed in Section 3.2. Errors were estimated with a Monte Carlo approach as described in Section 3.4.

	POC flux to the sediments ($Pg\ C\ year^{-1}$)	Pelagic denitrification ($Tg\ N\ year^{-1}$)	Benthic denitrification ($Tg\ N\ year^{-1}$)	Pelagic N_2O production ($Tg\ N\ year^{-1}$)
North Pacific	0.51 (0.37)	21.5	46.5 (30.7)	2.05
South Pacific	0.31 (0.22)	17.6	25.9 (17.3)	1.29
Indian Ocean	0.22 (0.13)	31.2	21.1 (11.0)	1.70
North Atlantic	0.54 (0.40)	-	47.0 (29.2)	0.48
South Atlantic	0.27 (0.20)	-	20.8 (13.1)	0.49
Southern Ocean	0.06 (0.01)	-	5.9 (1.6)	0.14
Arctic Ocean	0.27 (0.21)	-	30.6 (21.4)	0.04
Global	2.2 ± 0.8 (1.5)	70 ± 50	198 ± 64 (124)	6.2 ± 3.2

Table 3.4: Sensitivity of the globally integrated pelagic respiration, denitrification and N_2O production to the remineralization model parameters. Results are averages obtained by using the three oxygen data sets described in Section 3.2.

	Mean value and error estimate adopted for this study	Ref.	Sensitivity			
			Benthic POC Flux ($Pg\ yr^{-1}$)	Pelagic Denitrification ($Tg\ yr^{-1}$)	Benthic Denitrification ($Tg\ yr^{-1}$)	N_2O production ($Tg\ yr^{-1}$)
Φ_0^{POC}	$9.4\pm3.5\ Pg\ yr^{-1}$	1	$0.23\ \frac{Pg\ yr^{-1}}{Pg\ yr^{-1}}$	$7.5\ \frac{Tg\ yr^{-1}}{Pg\ yr^{-1}}$	$14.8\ \frac{Tg\ yr^{-1}}{Pg\ yr^{-1}}$	$0.66\ \frac{Tg\ yr^{-1}}{Pg\ yr^{-1}}$
z_0	75±20 m	2	$0.09\ \frac{Pg\ yr^{-1}}{10\ m}$	$7.5\ \frac{Tg\ yr^{-1}}{10\ m}$	$10.3\ \frac{Tg\ yr^{-1}}{10\ m}$	$0.34\ \frac{Tg\ yr^{-1}}{10\ m}$
b	0.8±0.1	3,4,5	$-0.15\ \frac{Pg\ yr^{-1}}{0.1}$	$-5.4\ \frac{Tg\ yr^{-1}}{0.1}$	$-19.3\ \frac{Tg\ yr^{-1}}{0.1}$	$-0.014\ \frac{TgN\ yr^{-1}}{0.1}$
b^{subox}	0.36±0.1	6,7	$-0.02\ \frac{Pg\ yr^{-1}}{0.1}$	$14.5\ \frac{Tg\ yr^{-1}}{0.1}$	$-0.53\ \frac{Tg\ yr^{-1}}{0.1}$	$-0.042\ \frac{TgN\ yr^{-1}}{0.1}$
O_2^{subox}	4.5±2.0 $mmol\ m^{-3}$	8, 9, 10, 11	$-0.002\ \frac{Pg\ yr^{-1}}{mmol\ m^{-3}}$	$14.4\ \frac{Tg\ yr^{-1}}{mmol\ m^{-3}}$	$0.34\ \frac{Tg\ yr^{-1}}{mmol\ m^{-3}}$	$-0.35\ \frac{Tg\ yr^{-1}}{mmol\ m^{-3}}$
$r_{N:C}^{denitr}$	(120:106)±(10:106)	6, 12, 13	-	$5.8\ \frac{Tg\ yr^{-1}}{10:106}$	$16.5\ \frac{Tg\ yr^{-1}}{10:106}$	-
$r_{N:C}^{nitrif}$	(16:106)±(1:106)	14	-	-	-	$0.39\ \frac{TgN\ yr^{-1}}{1:106}$
a_1	0.26±0.06	15	-	-	-	$0.28\ \frac{TgN\ yr^{-1}}{0.01}$
a_2	$-4\cdot10^{-4}\pm10^{-4}$	15	-	-	-	$0.25\ \frac{TgN\ yr^{-1}}{10^{-4}}$
ΔO_2	-		$-0.002\ \frac{Pg\ yr^{-1}}{mmol\ m^{-3}}$	$-13.8\ \frac{Tg\ yr^{-1}}{mmol\ m^{-3}}$	$-0.33\ \frac{Tg\ yr^{-1}}{mmol\ m^{-3}}$	$-0.01\ \frac{Tg\ yr^{-1}}{mmol\ m^{-3}}$

References: 1, Dunne et al., (2007); 2, standard deviation of the 1% light level calculated using the algorithm given in Anderson et al., (2009); 3, Martin et al., (1987); 4, Berelson (2001); 5, Primeau (2006) ; 6, Devol and Hartnett, (2001), 7, Van Mooy et al., (2002); 8, Morrison et al., (1999); 9, Codispoti et al.,

(2001); 10, Bange et al., (2005); 11, Bulow et al., (2010); 12, Gruber and Sarmiento (1997); 13, Richards et al., (1965); 14, Anderson and Sarmiento (1994); 15, Nevison et al., (2003).

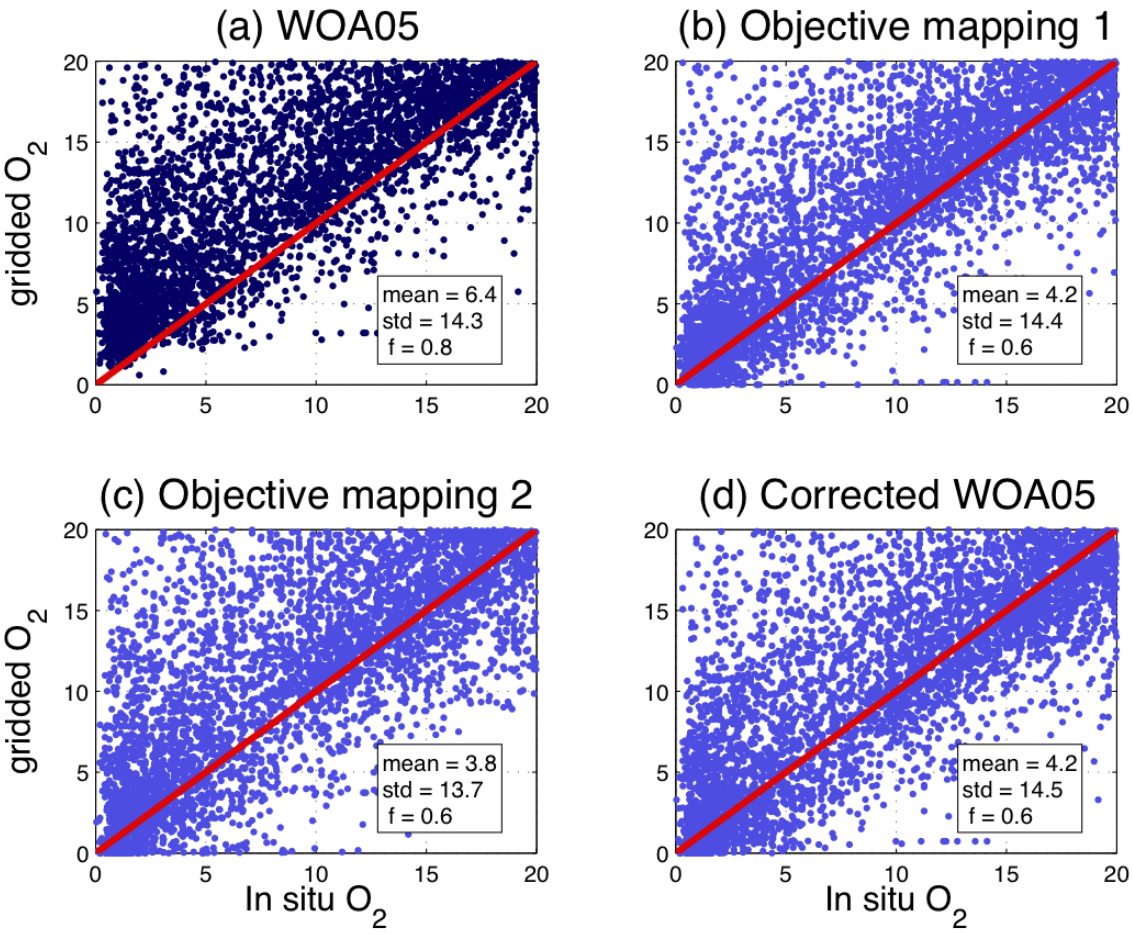


Figure 3.1: Scatter plot of in situ GLODAP vs. gridded oxygen data. The gridded data sets were sampled at the location and month of in situ measurements by using linear interpolation. Only values below 20 $\mathrm{mmol\,m^{-3}}$ are shown. The red line is the 1:1 line. The statistics shown are means and standard deviations of the oxygen biases (gridded minus in situ oxygen) in the hypoxic range ($\mathrm{O_2} < 60\,\mathrm{mmol\,m^{-3}}$), and f is the fraction of data points that fall above the 1:1 line (biases > 0). The data sets shown are: (a) WOA05; (b) objective analysis of GLODAP measurements following the mapping scheme by Gandin (1963); (c) objective analysis of GLODAP measurements following the mapping scheme by Barnes (1964); (d) WOA05 with linear correction based on in situ GLODAP measurements.

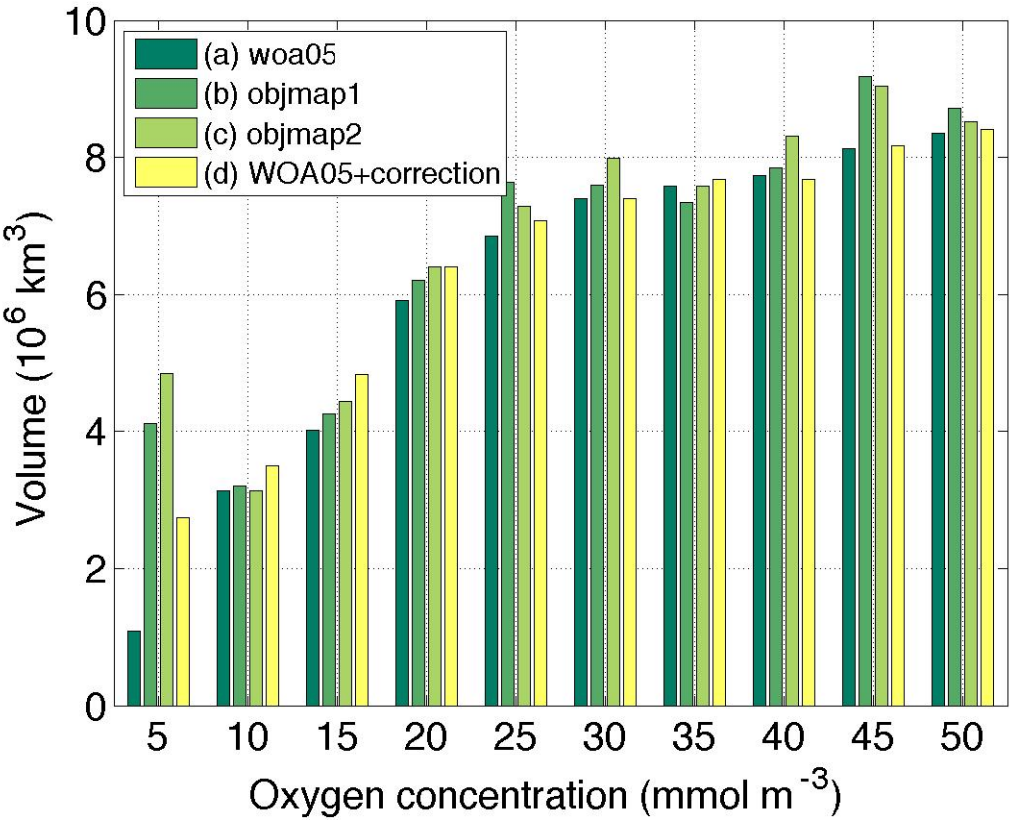


Figure 3.2: Volumetric distribution of oceanic oxygen from different gridded data sets discussed in Section 3.2. Water volumes have been binned according to oxygen concentration in 5 mmol m^{-3} wide bins, starting from 0 mmol m^{-3}. The data sets shown are: (a) WOA05; (b) objective analysis of GLODAP measurements following the mapping scheme by Gandin (1963); (c) objective analysis of GLODAP measurements following the mapping scheme by Barnes (1964); (d) WOA05 with linear correction based on in situ GLODAP measurements.

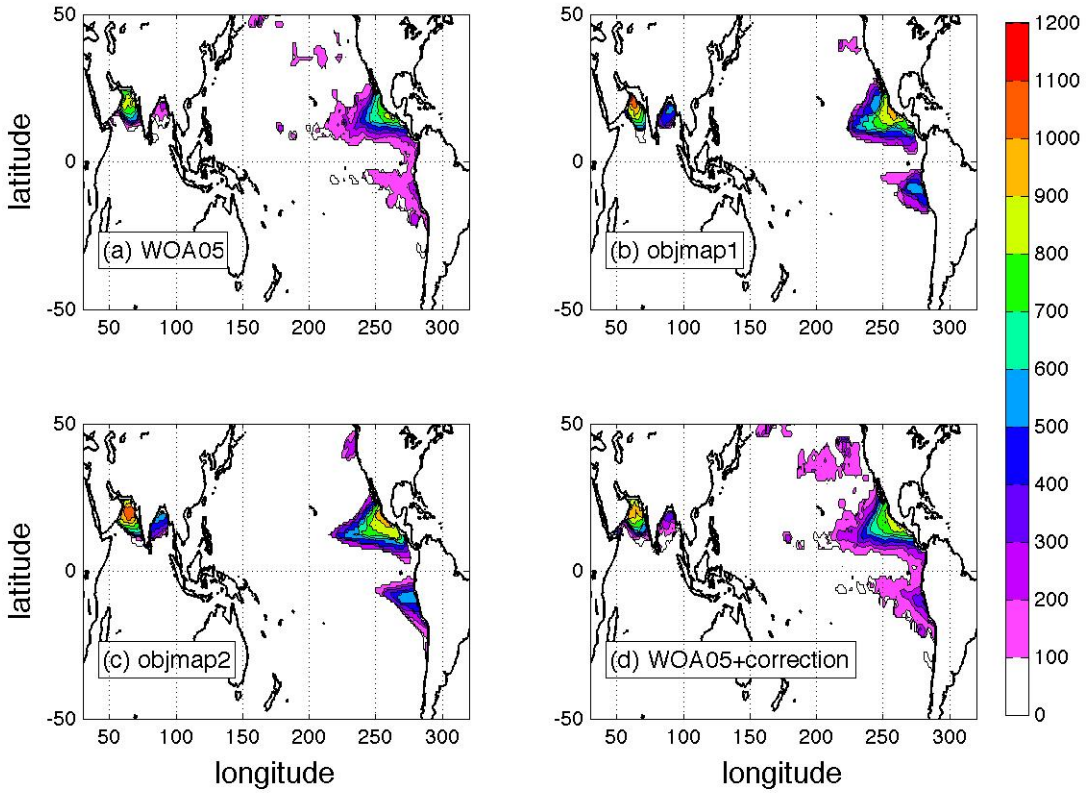


Figure 3.3: Thickness of the water column oxygen lower than 10 mmol m^{-3}. The data sets shown are: (a) monthly WOA05; (b) objective analysis of GLODAP measurements following the mapping scheme by Gandin (1963); (c) objective analysis of GLODAP measurements following the mapping scheme by Barnes (1964); (d) monthly WOA05 with linear correction based on in situ GLODAP measurements.

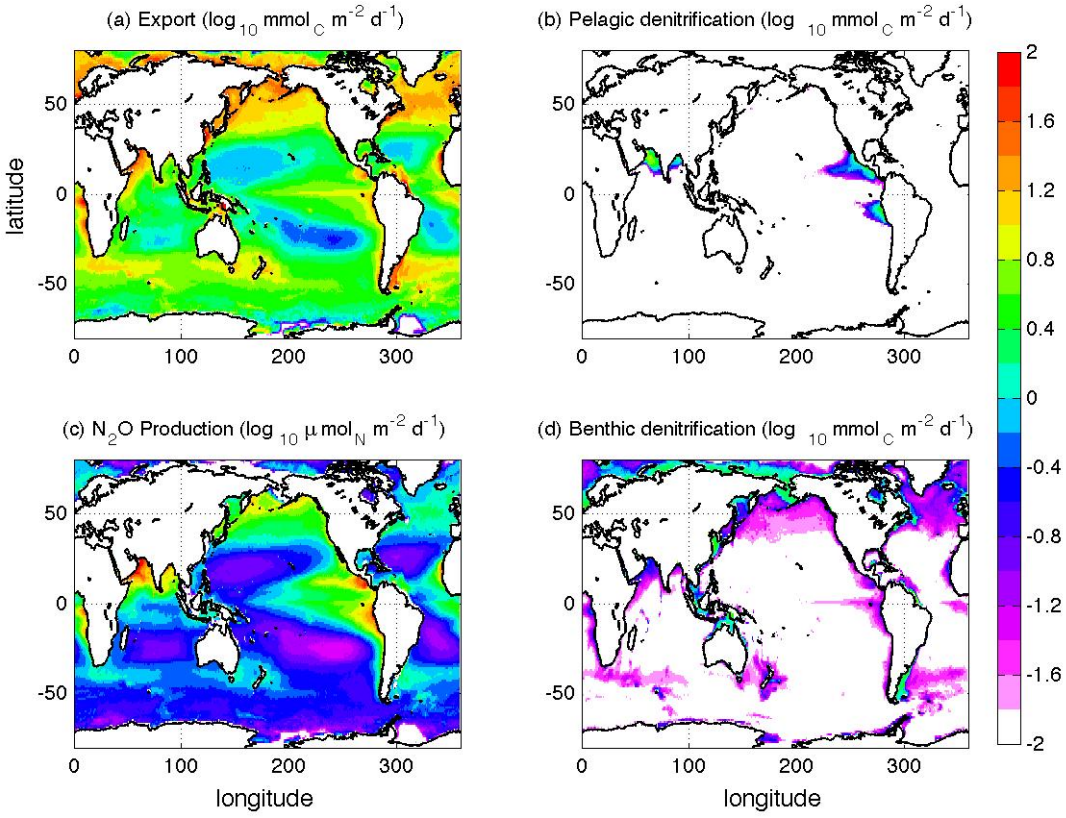


Figure 3.4: (a) export from the euphotic zone from Dunne et al., (2007); (b) vertically integrated pelagic denitrification; (c) vertically integrated N_2O production; (d) benthic denitrification. Contouring is on a $\log_{10}$ scale. Averages from the three oxygen data set described in Section 3.2 are shown.

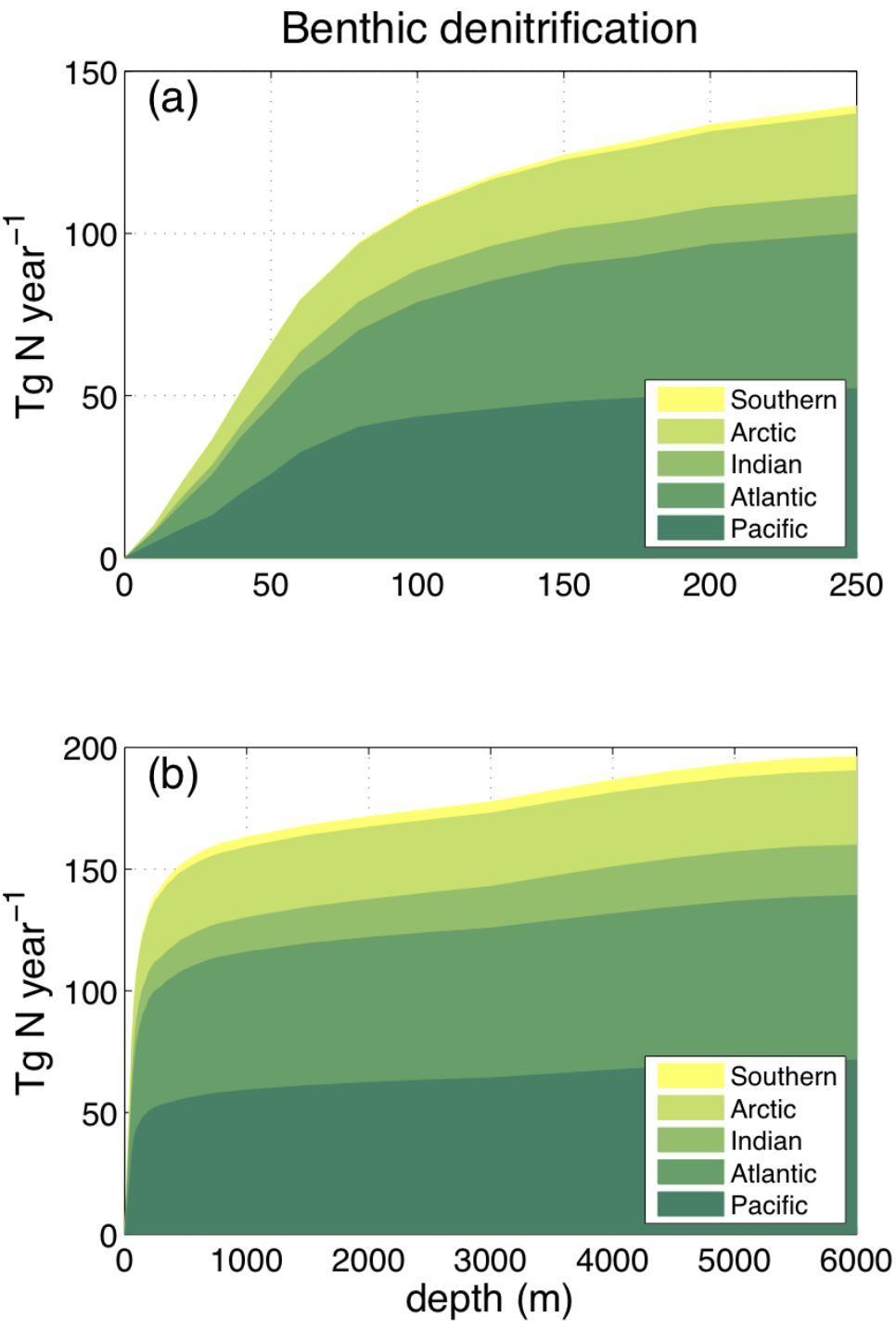


Figure 3.5: Cumulative benthic denitrification integrated from the surface to a given depth, divided by basin. (a) depths between 0 and 250 m; (b) entire water column.

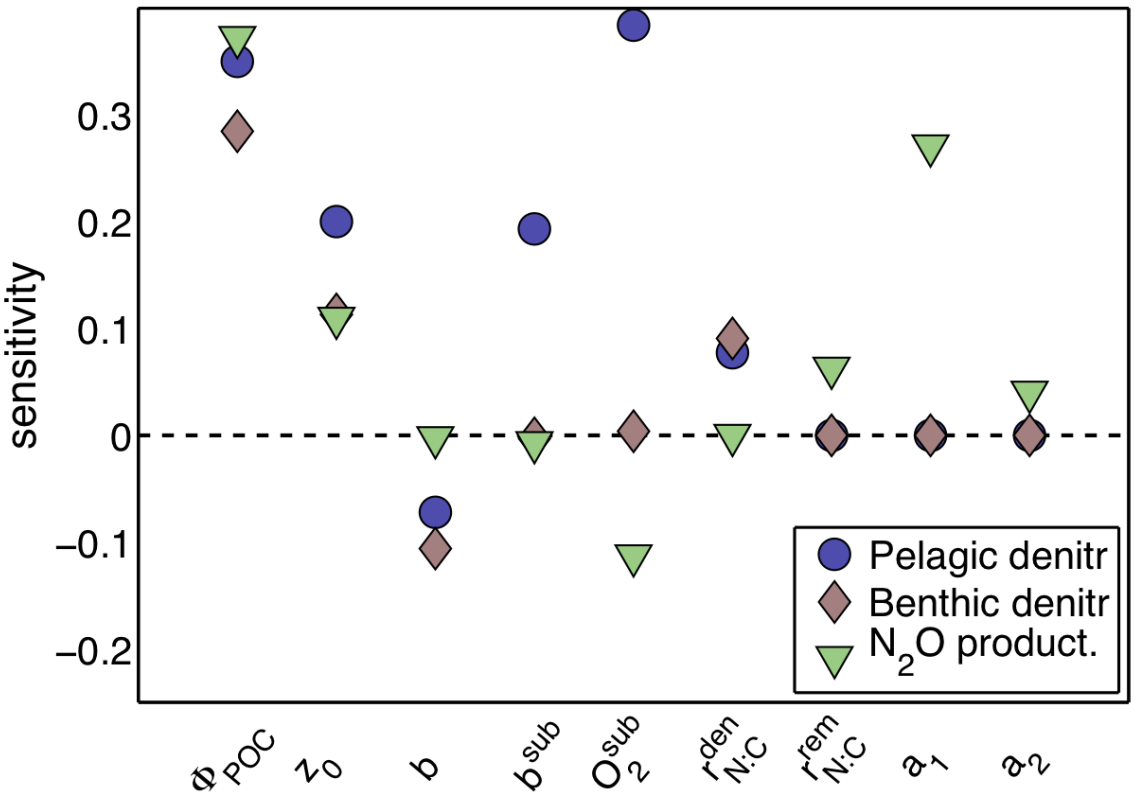


Figure 3.6: Relative sensitivity of pelagic denitrification, benthic denitrification and N_2O production to the model parameters. Sensitivities are calculated as fractional change in the global integrals for a change in each model parameter equal to one standard deviation (see Table 3.4). For example, the sensitivity of pelagic denitrification to changes in POC flux is calculated as: $\frac{\partial Denitr}{\partial \Phi_{POC}} \frac{\Delta \Phi_{POC}}{Denitr}$. Sensitivities equal to 0 indicate no change.

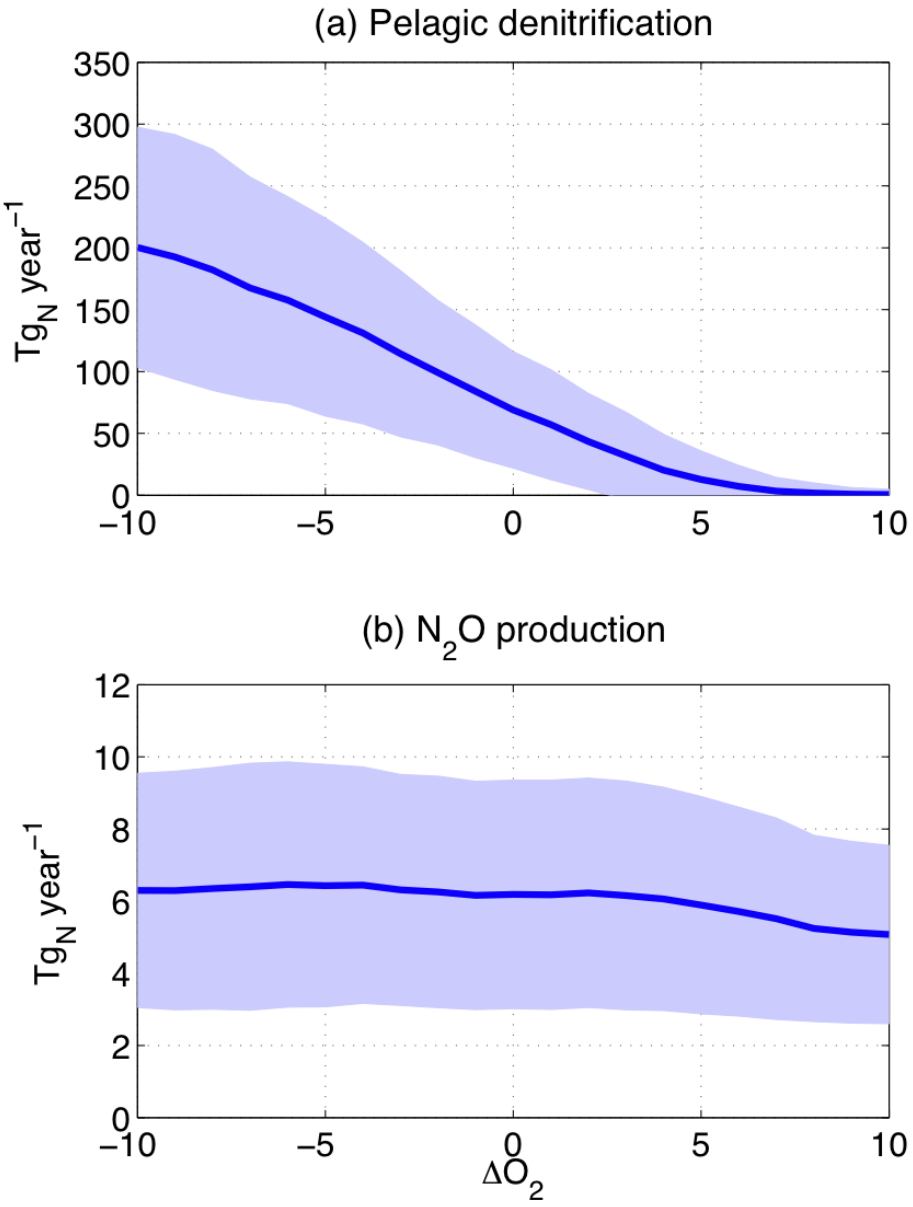


Figure 3.7: Sensitivity of (a) pelagic denitrification and (b) N_2O production to uniform changes (ΔO_2) in the ocean oxygen distribution. The solid line and the shading show the mean and standard deviation from a series of Monte Carlo simulations.

Chapter 4: Zooplankton diel vertical migration: controls and biogeochemical impacts in an ocean ecosystem model

Abstract

Diel vertical migration (DVM) of zooplankton and fish is a fundamental component of the biological pump, but is generally overlooked in global models of the Earth System. We implement a representation of DVM in a size-structured NPZD model and evaluate it against data from three major biomes in the Pacific Ocean. Our model includes: (1) a realistic parameterization of migration dynamics, (2) a representation of the processes that decouple zooplankton feeding and respiration in the water column, and (3) a consistent parameterization of visual predation. The model captures to first order the biomass and nutrient flux partitioning between different trophic levels, and the proportion of migrating zooplankton. We show that realistic migratory populations could sustain active fluxes of between 20 and 40 % of the particle export to the mesopelagic zone, and contribute to up to 50 % of the total respiration within the layers affected by migration with consequences for oxygen, nutrient, and carbon cycling. We highlight the importance

of allowing zooplankton feeding and excretion to vary independently with depth – a process that should be included in global parameterizations of DVM.

4.1 Introduction

Zooplankton and micronecton diel vertical migration (DVM) is ubiquitous in the marine environment. In the most common DVM pattern, the nocturnal migration, organisms descend to depth before sunrise and ascend to the surface at sunset. A variety of taxonomic groups perform DVM, including crustaceans, fish, mollusks, celenterates, ctenophores and chaetognaths (Roe et al., 1984; Saltzmann and Whishner, 1997; Angel and Pugh, 2000; Steinberg et al., 2008).

DVM is believed to originate as a tradeoff between the advantage of feeding in the phytoplankton-rich surface layers and the advantage of residing in the dark layers where grazing from visual predators is inhibited during daytime (Lampert, 1989, Hays, 2003). Substantial variability exists in the patterns of DVM, such as timing, daytime depths and migration velocities (Cohen and Forward Jr., 2009). This variability is related to, among others, intraspecific and interspecific differences, life stage of the migrating organisms, adaptation, and the response to physical and chemical environmental factors, food availability and predatory cues (Cohen and Forward Jr., 2009).

4.1.1 Proximate and ultimate controls on DVM

Light is considered the most important external control on DVM. Additionally, migration could be triggered by chemical or mechanical cues from predators (Cohen and Forward Jr., 2009). Three main hypotheses exist on the role of light in setting the patterns of migration. The isolume hypothesis suggests that migrating organisms tend to cluster

around a preferred light level during daytime. The absolute intensity threshold hypothesis suggests that upward/downward migrations initiate when the light intensity decreases below or increases above specific thresholds. Finally, the rate-of-change hypothesis states that migration is triggered by the relative rate of change in the light intensity and by its direction. Uncertainty exists as to which hypothesis is best suited to explain observed patterns of DVM, and experimental evidence exists that supports each of the three hypotheses (Cohen and Forward Jr., 2009). Different species, populations and ontogenetic stages might in fact differ in their response to light stimuli.

Despite the uncertainties on the proximate controls, and the variability in patterns, the widespread occurrence of DVM strongly supports an adaptive advantage for migrating behavior. The consensus hypothesis is that migration to deep dark waters reduces mortality due to visual predation. This advantage is partially offset by the costs associated with DVM. Among these, the most important are reduced food availability and feeding at depth, metabolic costs due to active swimming, and reduced metabolism at low temperatures, which tend to decrease growth and reproduction rates (Lampert, 1989; Cohen and Forward Jr., 2009).

4.1.2 DVM occurrence and patterns

In situ net sampling and remote sensing by acoustic Doppler current profiler (ADCP) provide complementary information on the occurrence and patterns of DVM. Net-based catches give a detailed picture of the taxonomic composition and biomasses of migrating organisms. ADCP-based observations provide information on the timing,

velocities and depths of migrating scattering layers, usually at high temporal and vertical resolution.

Day-night differences in zooplankton biomass from net sampling indicate widespread occurrence of DVM. Early compilation of tow data from several open ocean regions by Longhurst and Harrison (1988) showed that approximately 20 to 70 % of zooplankton and small nekton performed DVM. Recent studies confirm the prevalence of DVM across a spectrum of oceanographic conditions. The fraction of vertically migrating zooplankton ranges from 2-40 % in the North Atlantic Ocean (Angel end Pugh 2000), to 40-50 % in the subtropical and equatorial Pacific (Saltzmann and Whishner, 1997; Al-Mutairi and Landry, 2001; Steinberg et al., 2008; Decima et al., 2011), 60 % in the subarctic Pacific (Steinberg et al., 2008), and 75 % in the South Eastern subtropical Atlantic (Postel et al., 2007). Several studies indicate increasing migratory fractions for the larger zooplankton and micronekton size classes (Al-Mutairi and Landry, 2001; Steinberg et al., 2008; Decima et al., 2011).

ADCP studies from a variety of locations reveal the occurrence of coherent 50-100 m thick scattering layers, migrating on a daily basis to average depths of between 300-400 m. Some sites show the existence of multiple layers migrating to different depths. For example, acoustic data from the North Atlantic (Heywood, 1996) showed two layers migrating to 50-100 and 300-400 m respectively, with vertical speeds between 2 and 6 cm/s. Similar results in the Arabian Sea showed two migration patterns: a shallower layer of millimeter-scale mesozooplankton migrating to depths of 100-200 m, with a mean velocity of 2 $cm\,s^{-1}$, and a deeper layer of centimeter-scale mictophyd fish and large mesozooplankton migrating to depths of 300-400 m, with a mean velocity of 4

$cm\,s^{-1}$ (Morrison et al., 1999; Luo et al., 2000). The long term ADCP study of Jiang et al. (2007) in the subtropical North Atlantic, showed seasonal modulations of DVM patterns throughout the year, possibly controlled by seasonal cycles of irradiance and surface productivity.

4.1.3 Large-scale impacts of DVM

The widespread occurrence of DVM affects the ecology of the epipelagic and mesopelagic zones, modifying the patterns of grazing, predation, iterspecific and intraspecific interactions. DVM alters the distribution of biogeochemical fluxes of nutrients, carbon and oxygen in the water column. The excretion of dissolved organic and inorganic matter, the production of fecal pellets and the mortality of the migrating organisms at depth add to the sinking of particulate organic matter to form the active component of the biological pump, which ultimately transfers nutrients and carbon from the surface to the ocean interior (Longhurst and Harrison, 1988; Buesseler and Boyd, 2009; Robinson et al., 2010). In addition to active transfer, filter feeding by migrating organisms at depth could divert nutrients from sinking particles to the mesopelagic ecosystem, further enhancing deep respiration.

Longhurst and Harrison (1988) were among the first to focus on the biogeochemical relevance of active transport. By analyzing a compilation of open ocean observations of zooplankton and nekton biomass, and assuming average excretion rates, they suggested that the inclusion of DVM effects could increase export estimates based on particle export by 5 to 100 %. After Longhurst and Harrison's (1988) study, other analyses focused on quantifying the contributions of respiration, excretion, fecal pellet

production and mortality by vertical migrating organisms in a variety of oceanographic regimes (Longhurst et al., 1990; Dam et al., 1995; Zhang and Dam, 1997; Steinberg et al., 2000; Al-Mutairi and Landry, 2001; Schnetzer and Steinberg, 2002; Hannides et al., 2009). Taken together, these studies indicate that DVM could sustain active fluxes up to 10 - 30 % of particle export. The contribution could be higher for nitrogen and phosphate compared to carbon (Steinberg et al., 2002; Hannides et al., 2009).

Active transport by DVM organisms could play an important role in sustaining the metabolic requirements of the mesopelagic ecosystems (Buesseler et al., 2009; Robinson et al., 2010). Recent budget analyses showed that the energy demand of the mesopelagic ecosystem cannot be maintained by particle influxes alone (Burd et al., 2010). For example, the study by Steinberg et al. (2000) showed that the deep bacteria and zooplankton carbon demand at two subtropical and subpolar sites exceeded the convergence of particulate organic matter flux by approximately 5 and 16 times respectively. The authors invoke an external input of organic matter that could be partly met by DVM active transport.

By controlling the inventory of respired nutrients in the ocean, the biological pump regulates the partitioning of carbon between ocean and atmosphere. A stronger biological pump shifts nutrients to the respired pools, increasing the inventory of carbon in the ocean and decreasing it in the atmosphere (Ito and Follows, 2005). A significant component of the biological pump, DVM active transport could ultimately influence the air-sea carbon balance.

The role of the biological pump depends not only on the strength of the export, but also where in the water column carbon and nutrients are released back to the respired

pools. For example, Kwon et al. (2009) showed a high sensitivity of the atmosphere-ocean carbon partitioning to the profile of particle remineralization with depth in a global biogeochemistry model. An increase in the e-folding depth of particle remineralization by 24 m could reduce atmospheric CO_2 by 10-27 ppm by redistributing respired carbon from intermediate to deep waters (Kwon et al., 2009). In contrast with the respiration of sinking detritus, which decreases monotonically with depth (Martin et al., 1987), DVM respiration is enhanced within the layers where migrating organisms reside during daytime. Therefore, DVM fluxes affect the distribution and gradients of nutrients and carbon in a fundamentally different ways from particle remineralization.

The effect of localized respiration could be even more important for oxygen. The daytime migration depth is associated at several locations with minima in oxygen concentrations. It has been suggested that reduced oxygen levels provide a refuge from predators (Steinberg et al., 2008), but it is not clear to what extent respiration by migrating organisms further exacerbates low oxygen conditions. It is possible that DVM itself contributes to establishing the environmental conditions that favor migrating behavior.

Recent studies proposed a direct coupling between DVM and water column physics that could ultimately affect the large-scale ocean circulation. According to this hypothesis, swarms of vertically migrating organisms can induce significant small-scale turbulence by swimming through stratified waters (Dewar et al., 2006). Whether the effect of biologically generated turbulence can induce mixing at levels important on a global scale is still debated. Turbulence generate by centimetre scale or smaller organisms happens belows the Ozmidov scale, over which overturning is limited by

stratification. Therefore organisms could be inefficient in generating mixing (Gregg and Horne, 2009). Yet, the levels of mixing in most of the subsurface ocean below the mixed layer and away from rough bottom topography are extremely small. The possibility that inputs of mechanical energy from the marine biosphere could be comparable in magnitude to the canonical sources of energy for ocean mixing, i.e., winds and tides, cannot yet be discarded (Dewar et al. 2006).

4.1.4 Modeling studies

Relatively few studies have attempted to model the distribution of vertically migrating organisms as a direct response to proximate stimuli such as light, food distribution, and other environmental factors (Andersen and Nival., 1991; Richards et al., 1996; Han and Straskraba, 1998). These studies show that a variety of responses to environmental conditions and stimuli can produce migration patterns that compare realistically with observations. However, the wide range of migrating behaviors, the variability in the responses to environmental factors, and the scarcity of detailed observations, seem to prevent the emergence of a unified framework that could be applied to a wide range DVM patterns (Lampert, 1989; Cohen and Forward Jr., 2009).

4.1.5 Objectives and outline of the chapter

The prevalence of DVM, and its potential for altering water column ecology and biogeochemistry, call for detailed studies of DVM impacts in models of the marine food web aimed at global fisheries and biogeochemical cycles.

Here, we develop a general framework to include DVM in ocean ecosystem models, and we implement it in a size-structured NPZD model that shares a common structure with more complex models currently run at broad regional and global scales.

Our study addresses two fundamental questions: (1) what processes are required to produce a robust representation of migration that can be applied on global scales, and (2) what are the impacts of DVM on the water column ecosystem, biogeochemistry, and biological pump?

To address these questions, we develop a consistent representation of visual predation and a representation of the processes that decouple zooplankton feeding and respiration in the water column. We test the robustness of the model by evaluating it against data from three major biomes in the Pacific Ocean.

The rest of the chapter is organized as follow. Section 4.2 describes the modeling framework, with emphasis on the formulation of vertical migration, the dynamics of zooplankton internal nutrient pools, and visual predation. Section 4.3 describes the set-up for the three sites of model implementation. Section 4.4 describes the results of the simulations, focusing on ecosystem structure, DVM patterns and water column biogeochemistry. Section 4.5 concludes the chapter.

4.2 Modeling framework

We couple a size-structured model of the marine ecosystem that includes a representation of diel vertical migration to a one-dimensional model of the water column.

The philosophy of this study is to maintain a relatively simple representation of basic ecosystem functions across a range of realistic physical settings, and focus the attention on a consistent simulation of DVM processes. The aim is identifying the key aspects that are needed to represent explicit DVM in eulerian size-structured models of the marine food web, of the kind currently developed for use in global Earth System Models. Our approach can be extended to more complex models of the marine ecosystem, and to fully three-dimensional models.

4.2.1 Ecosystem model

We adapt the marine ecosystem model developed by Stock and Dunne (2010) to include vertically migrating organisms. The model by Stock and Dunne (2010) captures the partitioning of productivity and biomass across trophic levels in response to different temperature, nutrient supply and euphotic zone depths, and has been optimized against observational constraints. A schematic of the model, including migrating zooplankton, is shown in Figure 4.1. The model uses 10 state variables representing major functional groups: small and large phytoplankton (SP, LP), small and large zooplankton (SZ, LZ, LMZ), free-living bacteria (B) and three classes of detritus (small labile and semilabile and large detritus, SDL, SDS, LD respectively). The large migrating zooplankton group (LMZ) is modeled following the large zooplankton (LZ). Biomasses are defined in terms of one single limiting nutrient expressed in nitrogen units (N). Constant stoichiometry for other elements is assumed.

All state variables are subject to advection and diffusion from the physical model. Large detritus sinks with a constant velocity of 20 md^{-1}. Vertical migrating organisms

(LMZ) are allowed to move in the water column following the behavioral rules described in Section 4.2.2.

Phytoplankton uptake and growth are parameterized with the photadaptation scheme of Geider et al. (1997). Phytoplankton mortality, zooplankton grazing, bacterial and detritus dynamics follow the formulation of Stock and Dunne (2010).

In order to simulate the impact of DVM on zooplankton physiology and the ecosystem in a realistic way, we introduce two major changes to the model by Stock and Dunne (2010). First, we develop a parameterization to explicitly model internal gut content and metabolite dynamics for large zooplankton (LZ and LMZ), and to include the metabolic costs of swimming. To this end, we subdivide LZ and LMZ into three internal nutrient pools (see schematic in Figure 4.2). This is detailed in section 4.2.3. Second, we develop a parameterization for large zooplankton mortality due to visual predation, as described in section 4.2.4.

4.2.2 Diel vertical migration model

Previous modeling studies have shown that realistic migration patterns can be achieved by different responses to light stimuli (Cohen and Forward Jr., 2009). Here, we assume that DVM is controlled by the absolute intensity of light, and migrating organisms cluster around a preferred isolume during daytime. This hypothesis, supported by experimental evidence, allows for a simple and effective control on the migration patterns. In addition to the light-mediated controls, we include the effects of food availability. The behavior of daily vertical migrators follows a simple set of rules that dictate the direction and velocity of migration. During daytime, zooplankton migrate

towards the preferred isolume (irr^{DVM}). For the control simulation we choose $irr^{DVM} = 10^{-5}\ W\ m^{-2}$, in line with existing observations (e.g. Boden and Kampa, 1967, Roe, 1983). When light is below the preferred irradiance, zooplankton migrate towards the local food maximum. The migration velocity (w^{swim}) is constant everywhere except around the preferred light level and around the food maximum, where it is reduced linearly toward zero, with scales of 50 and 20 m respectively. We set the maximum migration velocity to 3 $\mathrm{cm\,s^{-1}}$, comparable to the average velocity of migrating scattering layers (Heywood, 1996; Luo et al., 2000; Morrison et al., 1999; Jiang et al., 2007).

In the absence of a random swimming component, migrating organisms would accumulate in a single layer with a thickness controlled by the model vertical spacing. To prevent unrealistic model-dependent behavior, we include a biological diffusion term (K_v^{bio}) for the migrating organisms. The additional diffusion is a crude way of parameterizing the effects of fluctuations in the swimming velocities of the migrating organisms. In nature, such fluctuations are related to behavioral and physiological differences between individuals. The magnitude of the biological diffusion can be estimated from observations. Assuming a thickness for the migrating layer on the order of 10 to 100 m, and a migration velocity on the order of 10^{-2} to $10^{-1}\ m\,s^{-1}$, a random swimming diffusion K_v^{bio} on the order of 10^{-1} to $10\ m^2\,s^{-1}$ is required. Here we adopt $K_v^{bio} = 10^{-1}\ m^2\,s^{-1}$.

This simple set of rules allows the formation of a localized coherent layer of migrating organisms that compares realistically with ADCP observations of migrating

scattering layers (e.g. Heywood, 1996; Morrison et al., 1999; Luo et al., 2000). An example of diel migration cycle from the model is shown in Figure 4.3.

4.2.3 Zooplankton internal pool dynamics and costs of swimming

Feeding by migrating organisms at the surface and evacuation and excretion at depth, help decouple particle production and nutrient regeneration from photosynthesis (Buesseler and Boyd, 2009; Robinson et al., 2010). For vertical migration to be effective in altering the flux of particles with depth, the time associated with the gut clearance of migrating organisms must be comparable to or longer than the duration of the vertical migration (approximately 3 hours). This has been observed for the larger components of mesozooplankton and micronekton communities. However, small mesozooplankton, for example several species of copepods, are characterized by gut evacuation times of a few hours or less (Mackas and Bohrer, 1976; Angel and Pugh, 2000). Similar considerations apply for respiratory and excretory fluxes. For these processes to be a relevant source of dissolved nutrients and carbon at depth, the time scale associated with the metabolic utilization of food must also be comparable to, or longer than the migration time scale. Observational evidence shows high levels of respiration extending for up to 24 hours following food ingestion (Hernandez-Leon and Ikeda, 2008). The increment in respiration after feeding originates from the costs of biosynthesis associated with the incorporation of nutrients and carbon into proteins, lipids and polysaccharides forming zooplankton biomass (Hernandez-Leon and Ikeda, 2008).

We decouple evacuation and metabolism from feeding by partitioning large zooplankton biomass (both for LZ and LMZ) into three pools (Figure 4.2): the gut content (Z^{gut}), the metabolic pool (Z^{metab}), and the body biomass (Z^{body}). These pools are connected together and to the dissolved nutrient and detrital pools through the following fluxes (Figure 4.2): (1) ingestion, (2) egestion, (3) assimilation, (4) catabolism, and (5) anabolism. The sum of egestion and assimilation equals gut clearing, and the sum of anabolism and catabolism corresponds to metabolism.

The resulting conservation equations (omitting predatory losses) are:

$$\frac{\partial Z^{gut}}{\partial t} = ingestion - egestion - assimilation$$

$$\frac{\partial Z^{metab}}{\partial t} = assimilation - catabolism - anabolism$$

$$\frac{\partial Z^{body}}{\partial t} = anabolism$$

We parameterize gut clearing with a first order dynamics, equivalent to an exponential decay of gut content in absence of ingestion (Mackas and Bohrer, 1976). We partition clearing into egestion and assimilation components:

$$clearing = egestion + assimilation = k^{clear} \cdot Z^{gut}$$

$$egestion = \gamma^{egest} \cdot k^{clear} \cdot Z^{gut}$$

$$assimilation = (1 - \gamma^{egest}) \cdot k^{clear} \cdot Z^{gut}$$

Here k^{clear} is the temperature dependent gut clearance rate, and γ^{egest} is the fraction of gut clearing that is directed to the detritus pools. We choose a value for k^{clear} of 8.0 d^{-1}, corresponding to an e-folding time scale for gut content of 3 hours at 20ºC (Mackas and Bohrer, 1976).

Similarly, we model metabolism (the sum of catabolism and anabolism) with a first order flux from the metabolic pool:

$$metabolism = catabolism + anabolism = k^{metab} \cdot Z^{metab}$$

Here k^{metab} is the temperature-dependent rate for the utilization of metabolites. We assume a value for k^{metab} equal to 1.0 d^{-1}, implying an e-folding timescale for the metabolic pool of 24 hours, compatible with the results reported by Hernandez-Leon and Ikeda (2008).

Similarly to Stock and Dunne (2010), we divide catabolism into a basal component, assumed to be proportional to biomass, and a component related to the feeding activity:

$$catabolism_{basal} = \mu^{basal} \cdot Z^{body}$$

$$catabolism_{feeding} = \gamma^{catab} \cdot k^{metab} \cdot Z^{metab}$$

Here, μ^{basal} is a temperature dependent basal rate, and γ^{catab} is the fraction of metabolism that is lost to the processes associated with grazing, digesting and assimilating food.

At steady state, clearing and metabolism are both proportional to the ingestion rate. This allows us to choose γ^{egest} and γ^{catab} to maintain, in a steady state sense, the same partitioning of ingestion into egestion and respiration as in Stock and Dunne (2010).

For vertically migrating organisms (LMZ), we add an explicit metabolic cost associated with migratory swimming. We base the formulation on the linear relationship between respiration and swimming velocity proposed by Torres and Childress (1983) to describe respiration rates in euphausiids:

$$catabolism_{swim} = \frac{w^{swim}}{w^{ref}} \mu^{basal} \cdot Z^{body}$$

Here w^{swim} is the average vertical migration velocity, and w^{ref} is a reference velocity used to scale the cost of swimming with respect to basal metabolism. When w^{ref} is equal to w^{swim}, active swimming doubles respiration rates compared to the basal activity. The numerical value of w^{ref} is relatively unconstrained, and can potentially be inferred from observations of zooplankton respiratory rates under different levels of swimming activity. For example, the study by Torres and Childress (1983) suggests values for w^{ref} between approximately 1 and 3 $\mathrm{cm\,s^{-1}}$. This is larger than routine swimming velocities (~1 $\mathrm{cm\,s^{-1}}$), and comparable to active swimming velocities (~3 $\mathrm{cm\,s^{-1}}$). In this study we adopt $w^{ref} = 7$ $\mathrm{cm\,s^{-1}}$ for the control simulations. This value is required to maintain realistic populations of migrating organisms, as discussed in Section 4.2.

Anabolism, corresponding to biomass buildup, is calculated as the difference between metabolism and the three catabolic components:

$$catabolism = catabolism_{feeding} + catabolism_{basal} + catabolism_{swim}$$

$$anabolism = metabolism - catabolism$$

4.2.4 Visual predation

The hypothesis that diel vertical migration evolved as a trade off to reduce losses due to visual predators calls for a consistent model of visual grazing. We derive a functional response for grazing losses based on existing models of visual predation in the marine environment. The functional response combines the effects of prey density and light availability on feeding rates, and is based on the ability of visual predators to encounter, recognize and harvest their prey.

We start with the theoretical model of Aksnes and Giske (1993), based on the Holling disk equation (Holling, 1966). The Holling disk equation relates the maximum feeding rate of a predator to the prey encounter rate and the time spent on searching and handling prey. Here we consider the case of a population of high-order visual predators (HP^v) feeding on large zooplankton (Z=LZ+LMZ). Following the model of Aksnes and Giske (1993), the ingestion rate (I_{HP^v}) of visual predators on zooplankton can be expressed as:

$$I_{HP^v} = \frac{a\,Z}{1 + a\,h\,Z}$$

Here h is the handling time and a is the predator-prey encounter rate (in $m^3 s^{-1}$ units). The encounter rate can be related to the volume of water cruised by the predator as

a function of the cruising velocity (v), the predator visual range (r) and the reactive field angle (θ) to obtain:

$$a = \pi r^2 \sin^2 \theta v$$

The visual range is generally a function of the predator visual system, prey size and contrast and of ambient light levels. Aksens and Utne (1997) developed a prey detection criterion that relates the visual range to the ambient irradiance (irr) based on the neural response of the predators to visual stimuli. The resulting nonlinear equation can be expressed as:

$$r^2 \cdot \exp(c\, r) = T_1 \frac{irr}{K_{irr} + irr}$$

where c is the beam attenuation coefficient, T_1 a predator and prey specific sensitivity parameter, proportional to the prey cross-sectional area and contrast, and K_{irr} the half saturation constant for the light response of predators. For the parameter range encountered in the ocean, a good approximation to the equation is obtained by ignoring the exponential term:

$$r^2 = T_1 \frac{irr}{K_{irr} + irr}$$

This approximation always overestimates the true visual range, and its validity depends on the magnitude of the sensitivity parameter T_1. Over a wide set of values for T_1, the approximate visual range is less than 10 % larger than the true visual range, suggesting that the approximation is good for predator-prey interactions in the marine

ecosystem. By using the approximate visual range, the encounter rate can be related to ambient irradiance:

$$a = a_{\max} \frac{irr}{K_{irr} + irr}$$

where $a_{\max} = \pi T_1 \sin^2 \theta v$

We can now combine the equation for the feeding rate I_{HP^v} with the equation for the encounter rate a to obtain:

$$I_{HP^v} = \frac{a_{\max}\, irr\, Z}{K_{irr} + irr\left(1 + a_{\max}\, h\, Z\right)}$$

By setting $K_Z^v = \left(a_{\max}\, h\right)^{-1}$ and $I_{HP^v}^{\max} = h^{-1}$, the equation can be rewritten as:

$$I_{HP^v} = I_{HP^v}^{\max} \frac{Z}{K_Z^v + Z_Z} \cdot \frac{irr}{\frac{K_Z^v}{K_Z^v + Z} K_{irr} + irr}$$

This equation combines the dependence of the feeding rate on irradiance and prey density in a single expression controlled by three parameters (K_Z^v, K_{irr} and $I_{HP^v}^{\max}$). The same equation can be adapted to non-visual predators by dropping the light dependence (setting $K_{irr} = 0$), to obtain a classical Holling disk equation for non visual predators (HP^{nv}):

$$I_{HP^{nv}} = I_{HP^v}^{\max} \frac{Z}{K_Z^{nv} + Z}$$

We implement visual and non-visual predatory losses for both large zooplankton and migrating organisms. Following Stock and Dunne, (2010) we assume that the

biomass of high order predators (HP) is proportional to the prey biomass and we allow for two separate contributions from visual and non-visual predators. The ingestion rate of HP on the available prey (Z) is given by:

$$I_{HP} = I_{HP^{nv}}^{\max} \frac{Z}{K_Z^{nv} + Z} + I_{HP^{v}}^{\max} \frac{Z}{K_Z^{v} + Z} \cdot \frac{irr}{\frac{K_Z^{v}}{K_Z^{v} + Z} \cdot K_{irr} + irr}$$

Here $I_{HP^{nv}}$ and $I_{HP^{v}}$ are the maximum feeding rates of visual and non-visual predators. As a further simplification we assume that the half saturation constants for prey density dependence are of the same magnitude, that is, $K_Z^{nv} \approx K_Z^{v} = K_Z$. Under this approximation, supported by observational constraints (Sørnes and Aksnes, 2004), the feeding rate of high-order predators can be simplified to:

$$I_{HP} = I_{HP}^{\max} \cdot f_{HP} = I_{HP}^{\max} \cdot \frac{Z}{K_Z + Z} \cdot \left[\left(1 - \alpha^{v}\right) + \alpha^{v} \frac{irr}{\left(\frac{K_Z}{K_Z + Z}\right) \cdot K_{irr} + irr} \right]$$

Here, $I_{HP}^{\max} = I_{HP^{nv}}^{\max} + I_{HP^{v}}^{\max}$ is the maximum feeding rate of all high order predators, and $\alpha^{v} = I_{HP^{v}}^{\max} / I_{HP}^{\max}$ is the relative contribution from visual predators.

For this study, we adopt $I_{HP}^{\max}$ and K_Z values from Stock and Dunne, (2010). Limited data exist to constrain the numerical values for K_{irr} and α^{v} in the open ocean. Handling times and encounter rates for a variety of visual and tactile predators suggest feeding rates for visual predators at least one order of magnitude larger than for non-visual predators, and similar half saturation constants (Sørnes and Aksnes 2004). Measurements of the feeding rate of the coastal fish *Gobiusculus Flavescens* indicates a

half saturation constant for the light response $K_{irr} = 0.8 \frac{\mu E}{m^2 s}$, or approximately 1.7 10^{-1} $\mathrm{W\,m^{-2}}$ (Sornes and Aksnes, 2004). For the control runs, we adopt $\alpha^v = 0.9$, and $K_{irr} = 10^{-2}$ $\mathrm{W\,m^{-2}}$. The smaller K_{irr} value compared to the study by Sornes and Aksnes (2004), allows for a deeper influence of visual predation in the open ocean.

A plot of the dependence of the limitation factor f_{HP} on local irradiance and prey concentration is shown in Figure 4.4. At low prey concentrations the ingestion decreases to zero. At low irradiances the light dependent term decreases to zero, and non-visual predation dominates. At high irradiances, the light-dependence term quickly saturates to 1, and the prey density dependence dominates.

A sensitivity study of the response of migrating zooplankton to changes in the visual predation parameters α^v and K_{irr} is discussed in Section 4.4.4.

4.3 Model set-up

We couple the ecosystem model with a one-dimensional physical model implemented along a gradient of oceanographic conditions in the North Pacific Ocean, including the subpolar gyre, the subtropical gyre and the eastern equatorial Pacific. We choose three sites for which numerous observations are available: station K2 (161°E, 47°N, Buesseler et al., 2008), station ALOHA (158°W, 22.5°N, Karl et al., 1996), and one of the EQPAC sites of the US JGOFS process study (140°W, 0°N, Murray et al., 1995). The locations of model implementation are shown in Figure 4.5.

Our objective is to test the robustness of the model against observations for a range of biomes, from warm-water oligotrophic to cold and warm-water mesotrophic ecosystems, covering a range of productivities and biomass partitioning across trophic levels.

4.3.1 One-dimensional model implementation

The physical model is a 1-dimensional mixed layer/ocean interior model based on a Mellor-Yamada turbulence closure scheme (Kearny et al. *manuscript in preparation*). The model is forced with surface winds, air temperatures and short wave irradiances from a reanalysis-based climatology (CORE, Griffies et al., 2009, Figure 4.6). We modulate the mean climatological short-wave irradiance by a latitude and time-dependent daily light cycle.

The closure scheme generates a turbulent diffusion profile, which is added to a background diffusion k_v^{bkg}. It is not clear whether a single background diffusion is best suited to represent subsurface mixing in different ocean regions. In this study, we opted for using different levels of background diffusion at the three sites in order to achieve more realistic simulations of nutrient inputs and productivities. This approach helps reduce problems due to the lack of a fully 3-dimensional circulation. We set k_v^{bkg} to $3.0 \cdot 10^{-5}$, $8.0 \cdot 10^{-5}$ and $5.0 \cdot 10^{-5}\ m^2 s^{-1}$ at K2, ALOHA and EQPAC respectively.

We include a restoring term for temperature and salinity to represent unresolved physical processes related to the three-dimensional circulation, and to prevent unrealistic drift from observed physical conditions. We restore temperature and salinity to monthly climatological profiles from the World Ocean Atlas, with a timescale of 90 days.

Additionally, we include a weak restoring with a 5-year timescale to climatological nitrate for the dissolved nutrient (N), in order to prevent long-term subsurface drifts due to nutrient trapping.

The numerical values of the parameters controlling DVM-related processes are shown in Table 4.1. The numerical values of all other ecosystem parameters have been drawn from the optimization study by Stock and Dunne, (2010).

We solve the model equations on a uniform grid with 5 m vertical resolution, using a forward in time (Euler) integration with a time step of 1 hour, sufficient to resolve details of vertical migrations. Additional tests showed good agreement between solutions obtained with finer vertical grids and smaller time steps.

4.3.2 Overview of the study sites

The three location of model implementation span a range of different temperatures, seasonality, nutrient supply, productivities and biomasses. Table 4.2 summarizes a set of ecosystem diagnostics for the three sites.

Station K2 is a cold-water mesotrophic site. A shallow halocline limits deep wintertime mixing to approximately 80-120 m in winter (Harrison et al., 1999). Surface nutrients peak in winter at the time of deepest mixing and drop in summer as the mixed layer shallows to 20-40 m, but never show a complete depletion.

The nutrient drawdown is associated with a phytoplankton bloom. Picoplankton (size class < 2 μm) are overall the largest contributors to chlorophyll and productivity (Liu et al., 2004). Large diatoms (> 20 μm) become important during blooms, and contribute to the relatively high level of particle export both directly and by sustaining the

mesozooplankton population (Boyd et al., 2008). Mesozooplankton are generally abundant and appear to perform significant diel vertical migrations to mean depths of between 200 and 400 m (Steinberg et al., 2008).

Ocean station ALOHA is characterized by warm-water oligotrophic conditions. Wintertime mixed layers deepen to 80-100 m in winter, but fail to reach the nutricline. Nutrients are always depleted near the surface, and springtime phytoplankton blooms are not observed.

Measurements show low chlorophyll and limited seasonality (O'Brien et al., 2002; Brix et al., 2006, Buesseler et al., 2007). Picophytoplankton dominate over larger autotrophs. Low productivities sustain a microbial loop with high nutrient recycling and limited export (Brix et al., 2006; Buesseler et al., 2007). Approximately 40 % of mesozooplankton perform diel vertical migrations to mean depths between of 400 and 700 m (Al-Mutahiri and Landry, 2001; Steinberg et al. 2008). The proportion of migrating zooplankton increases to more than 70 % for size classes larger than 2000 μm.

The EQPAC site supports a warm-water mesotrophic ecosystem. Surface nutrients are never completely depleted (Lindley et al., 1995, Barber et al., 1996), and little seasonality is observed. Most variability is associated with the passage of equatorial waves and with ENSO dynamics (Kessler and McPhaden, 1995, Iriarte et al., 1995; Pennington et al., 2006).

Contrarily to other productive regions, small phytoplankton assemblages (pico- and nanoplankton) dominate at EQPAC (Lindley et al., 1995; Pennington et al., 2006). This favors the regeneration loop and limits particle export (Buesseler et al. 1995). Mesozooplankton are abundant and contribute to particle cycling through the production

of fecal pellets (Dam et al., 1995, Decima et al., 2011). Between 35 and 40 % of all mesozooplankton are involved in DVM. The proportion increases to more than 70 % for size classes larger than 2000 μm (Decima et al., 2011).

4.4 Model results

4.4.1 Water column physics and general ecosystem properties

Figure 4.7 compares the model seasonal cycles of temperature, mixed layer and euphotic zone depths to observed climatologies. In addition, the depth of the $10^{-5}\,\mathrm{W\,m^{-2}}$ isolume is shown. The model produces realistic simulations of water column physics at the three sites. Temperature shows seasonal cycles comparable to observations. Mixed layer depth shows a strong seasonal cycle at K2, where it deepens to more than 100 m in winter, and as shallow as 20 m at the peak of summer stratification. Seasonality is present, albeit less strong, at both ALOHA and EQPAC.

Table 4.2 summarizes the main ecosystem diagnostics for the simulations, and Figure 4.8 shows the annual cycle of vertically integrated biomasses. Overall, the model is in good agreement with the observational estimates, both in term of productivities and biomasses.

At K2, net primary production (NPP) is in the range suggested by observations. Euphotic zone depth (calculated as the depth at which NPP becomes zero) is deeper than suggested by some studies (Boyd et al., 2008). Chlorophyll and phytoplankton biomass are approximately 30 – 40 % higher than observed. This might reflect the deeper euphotic

zone depth used to calculate the integral diagnostics in Table 4.2. Large phytoplankton account on average for 1/3 of primary producers, and become dominant during the springtime bloom. The fraction of vertically migrating large zooplankton, 65 % is similar to the observed 60 % (size classes > 350 μm, Steinberg et al., 2008). Particle export fluxes are close to the high range of observations.

At ALOHA, euphotic zone depth, net primary production, chlorophyll, phytoplankton and zooplankton biomasses are close to observations. Little seasonality is present. The fraction of large phytoplankton, 26 %, is slightly higher than observed. Migrating zooplankton compose approximately 33 % of large zooplankton, less than suggested by some studies (e.g. 40 %, Steinberg et al., 2008). Particle export is in line with observations.

At EQPAC, euphotic zone depth, chlorophyll, phytoplankton and zooplankton biomasses are in the observed range. Net primary production is less than observed at the equator, but similar to the productivity of the surrounding band (Chavez et al., 1996; Landry et al., 2011). Similar to observations, the modeled ecosystem shows negligible seasonal variations. The proportion of phytoplankton in the large size classes, 20 %, is close to existing estimates (19 – 26 %, Taylor et al., 2011; Stock and Dunne, 2010). The fraction of large migrating zooplankton, 69 %, is substantially higher than suggested by measurements. For example Decima et al., (2011) show that approximately 40 % of mesozooplankton larger than 500 μm perform DVM. On the other hand, the proportion increases to 68 % for size classes larger than 2000 μm. Particle export fluxes are in line with observations.

4.4.2 DVM patterns

The assumption that migrating organisms cluster around a preferred isolume during daytime allows the model to capture some of the differences in the migration patterns at K2 and ALOHA. Observations show that migrating zooplankton cluster at approximately 200 – 400 m depth at K2, and 400-600 m depth at ALOHA (Steinberg et al., 2008). The offset in the migration depth at the two locations is approximately 200 m. In the models, due to the different surface chlorophyll concentrations and irradiance cycles, the preferred isolume (10^{-5} W m^{-2}) is located on average around 250 – 350 m at K2, and around 400 – 450 m at ALOHA. Different sensitivities to light, and the influence of other environmental factors, including temperature and oxygen, could account for the remaining difference in migration depth between the model simulations and observations.

The partitioning of large zooplankton between migrating and non-migrating groups is realistic at both K2 and ALOHA. However, the model fails to capture the observed proportion of migrating zooplankton at EQPAC. At this location, migratory zooplankton are almost twice more abundant than observed. This appears to be true for a range of parameters, as shown in the following sensitivity analysis.

4.4.3 Sensitivity of DVM to the model parameters

We explore the sensitivity to the parameters that control the partitioning of large zooplankton between migrating and non-migrating groups. To this end, we run a set of simulations where we vary the parameters over a range of possible values. We focus the analysis on the visual predation fraction (α^v), the costs of swimming (w^{ref}), the preferred

isolume (irr^{DVM}) and the half saturation constant for the light response (K_{irr}). Substantial uncertainty exists in these parameters. The values adopted for the control runs (summarized in Table 4.1) arise from a combination of informed guesses based on published studies, and from analyses of the sensitivity studies.

The results of the sensitivity studies are shown in Figure 4.9. Most of the impacts involve the higher trophic levels, specifically large zooplankton biomass and the partitioning between migrating and non-migrating organisms. This in turns has a moderate impact on other aspects of the ecosystem such as the partitioning between large and small phytoplankton.

As the fraction of predation from high-order visual predators (α^{v}) increases, DVM becomes an increasingly important mechanism to escape predation. This in turn increases the proportion of large migrating zooplankton. The response is similar at the three model locations. When all predatory losses are due to visual grazing, migratory zooplankton account for more than 90 % of large zooplankton at K2 and EQPAC, and 50 % at ALOHA. On the opposite side of the spectrum, even in absence of visual predation, a non-negligible fraction of migrating organisms is able to survive. When all predatory losses are due non-visual predators, the proportion of large migrating zooplankton decreases to 25 – 30 % at K2 and EQPAC, and 14 % at ALOHA.

The study by Torres and Childress (1983), based on measurements respiration in euphausiids, suggests w^{ref} values around 2 – 3 $\mathrm{cm\,s^{-1}}$. We find that this range supports realistic migrating fractions at EQPAC and K2, where the costs of swimming become negligible above $w^{ref} \approx 4$ $\mathrm{cm\,s^{-1}}$, but not at ALOHA, where w^{ref} values around 7 $\mathrm{cm\,s^{-1}}$

or larger are required. At ALOHA, basal metabolic rates are close in value to ingestion rates, due to the low availability of food sources (Stock and Dunne, 2010). Therefore, even a small relative increase in metabolism, for example due to migratory costs, can induce the collapse of the migrating zooplankton population.

The preferred isolume (irr^{DVM}) has a moderate effect on the proportion of migrating zooplankton. Isolumes between 10^{-6} and 10^{-5} $\mathrm{W\,m^{-2}}$ determine maximum fractions of migrating zooplankton. Deepening of the isolumes result in relatively small changes in the migrating fractions (10 – 40 %). A larger reduction (40 – 50 %) takes place as the preferred isolumes rise into the surface layers affected by visual predation.

A substantial uncertainty exists in the value of the half saturation constant for the light response of visual predators (K_{irr}). Overall, we find a limited sensitivity of the fraction of migrating organisms to this parameter.

4.4.4 Biogeochemical impacts of DVM

At steady state, the export of organic matter is balanced by physical inputs of nutrients into the euphotic zone. Sinking particles are the major export pathway out of the surface layers (Buesseler and Boyd, 2009). Additional export mechanisms include downward advection and diffusion of non-sinking detritus, and the active transport by migrating zooplankton.

We quantify the relevance of the different export pathways at the three model sites. We define net community production (NCP) as the total biomass exported from the euphotic zone. We further break down NCP into contributions from sinking particles, DVM active transport, and mixing of non-sinking detritus and other functional groups out

of the euphotic zone. This allows us to calculate classical ratios such as the *e-ratio* and *pe-ratio* (the ratios between total export and particle export and NPP), and define a *dvm-ratio* and *dom-ratio* (the ratios between active transport and export of non-sinking organic matter and NPP). The results are summarized in Table 4.3. The seasonal cycle of the export terms is shown in Figure 4.10. All locations appear to be in steady state over the seasonal cycle. Overall, high levels of export characterize the subarctic ecosystem, with approximately 40 % of NPP leaving the surface over the seasonal cycle. In comparison, the two warm water sites show high levels of nutrient recycling, and exports limited to approximately 10 % of net primary production. At the three sites sinking particles dominate the export. Active transport by DVM and detrainment of non-sinking detritus show similar contributions, ranging from approximately 1 – 3 % of NPP at ALOHA and EQPAC, to 7 – 9 % at K2. Seasonality is strongest at K2. Here, surface nutrients are replenished during the winter months, when mixed layers are deepest. At this time the export is dominated by mixing of detritus and other non-sinking biomass out of the euphotic zone. Conversely, export by particulate matter and DVM dominates in spring, at the time of phytoplankton blooms.

The fate of export varies significantly with the process involved. Ultimately, the majority of export is respired in the mesopelagic zone. However, the partitioning of respiratory fluxes in the water column varies with the process considered. Figure 4.11 shows respiratory and excretory sources of dissolved carbon in the mesopelagic zone, as well as the production of detritus at depth. Respiration of non-sinking detritus is limited to the upper layers and becomes negligible below 150 – 200 m depth. Remineralization of sinking particles represents a major term at all depths, except around the migration

depth, where zooplankton excretion and respiration become the main sources of dissolved nutrients and carbon. Here, DVM export is returned to the dissolved pools within a narrow layer (100 – 200 m thick), where migratory zooplankton increase respiration by approximately 80, 100 and 40 % at K2, EQPAC, and ALOHA respectively. In addition, DVM organisms contribute to the local production of particles via fecal pellet production and losses to high-order predators.

Filter feeding by migrating zooplankton at depth can fuel additional nutrients and carbon from sinking particles to the dissolved pools. Whereas a number of taxa are known to feed on particles at depth (Steinberg et al., 2008), it is not clear to what extent migrating zooplankton adopt this strategy. Evidence exists suggesting that migrating zooplankton mostly feed in the surface layers at night, and leave the mesopelagic zone with empty guts (Longhurst et al., 1989).

We tested the model response to filter feeding behavior by increasing particle availability to large zooplankton from 0 to 50 %. This change has minor effects on ecosystem structure and euphotic zone fluxes, but is able to alter mesopelagic respiration patterns. The ratios of zooplankton to detritus respiration around the migration depth increase to approximately 120 % at K2 ad EQPAC, and 50 % at ALOHA. Overall, the effect is stronger at K2 where a large standing stock of detritus is present.

We compare the importance of active (DVM) versus passive (sinking POM) exports by considering the ratios between these fluxes at 150 m depth, adopted here as upper boundary of the mesopelagic domain. We explore the importance of decoupling zooplankton feeding, egestion and excretion by explicitly representing gut passage and assimilated pools dynamics. To this end, we run 3 sets of simulations where we turn off

gut and metabolic pool dynamics. Additionally, we run a 4th set of simulations where we force the fraction of migrating zooplankton to match observations (60, 40, and 40 % at K2, ALOHA and EQPAC respectively, see Table 4.2). This is done by pooling together the LZ and LMZ groups and partitioning them according to the observed fraction before the onset of each migration. This method relaxes the full ecological consistency of the control runs, and allows us to prescribe the proportion between migrating and non-migrating zooplankton. This has negligible effects on NPP and NCP. Most changes involve POC and DVM exports.

The results from the 4 additional sets of simulations and from the control runs are summarized in Table 4.4. When no internal pools are considered, egestion and excretion occur at the same time of feeding. In this case, the only losses at depth are basal catabolism and predatory losses. This leads to an underestimate of active fluxes by a factor between 2.5 and 4 compared to the full model. The inclusion of either gut content or metabolic pool dynamics decouples feeding and losses, and results in a substantial increase in the deep export. The inclusion of gut passage and assimilated pool dynamics appears to have similar impacts on export when considered separately.`

Results from the runs with prescribed migrating fractions are similar to the control runs at K2 and ALOHA. This is not surprising given that the models achieve realistic proportions of migrating zooplankton at these two sites. At EQPAC, where the proportion of migrating zooplankton is reduced to approximately 2/3, the ratio between active transport and particle export decreases from 0.44 to 0.18. This reduction is due to a simultaneous increase in the *pe-ratio* (from 0.07 to 0.08) and decrease in the *dvm-ratio* (from 0.03 to 0.015). These changes reflect not only a different proportion of migrating

organisms, but also an increase in the large phytoplankton fraction (from 0.19 to 0.30), and an overall decrease of large zooplankton biomass (from 83 to 63 $\mathrm{mmolC\,m^{-2}d^{-1}}$).

4.5 Discussion and conclusions

We developed a framework to represent explicit diel vertical migrations in size-structured models of the marine food web, aimed at global ecosystem and biogeochemical studies. This required building parameterizations to include processes such as visual predation, zooplankton gut passage and assimilated pool dynamics, and a realistic representation of migratory behavior.

We tested the model against observations from a meridional gradient of oceanographic conditions in the North Pacific Ocean, comprising a warm and a cold water mesotrophic ecosystem, and a warm water oligotrophic ecosystem.

The model is able to capture basic observed ecological patterns, including productivity, nutrient flux and biomass partitioning between the different trophic levels. A single set of parameters can approximate to first order the proportion of migrating versus non-migrating zooplankton. However, regional biases remain. A formal optimization of the parameters that control DVM against observations could help resolve regional discrepancies.

The proportion of migrating zooplankton appears to be controlled in the models by the ecosystem productivity. Highly productive systems are able to support larger migratory populations. The isolume hypothesis can explain bulk differences in migration depths at the model sites. It is possible that variables not considered in this study play a

significant role in controlling migratory patterns. These could include regional adaptations, as well as additional environmental factors, for example oxygen concentration.

Among the parameters controlling DVM, the fraction of grazing due to visual predation and the metabolic costs of swimming appear to have the largest influence on the proportion of migrating zooplankton. The energy requirements of DVM have a stronger impact in the oligotrophic gyre compared to more productive sites. Matching the migratory biomass at the oligotrophic site requires a reduction of the costs of swimming between 3 and 4 times the values suggested by observations of euphausiids (Torres and Childress, 1983). This result mirrors the reduction in basal metabolic rates invoked by Stock and Dunne (2010) to capture mesozooplankton patterns in extremely low-productivity environments.

We also investigate the impacts of DVM on water column biogeochemistry in the models. Active transport by migrating zooplankton contributes between 1/3 and 1/6 of total export from the euphotic zone, and is comparable to the export due to dissolved organic matter. This proportion increases when considering exports to the mesopelagic zone, here assumed below 150 m depth. Realistic migratory populations could sustain active fluxes between 20 and 40 % the particle export to the deep layers.

The fate of the active transport differs from particle remineralization. Whereas the respiration of sinking detritus decreases with depth, respiration by migrating organisms is concentrated in a 150 – 200 m thick layer around the daytime migration depth. Here, respiratory and excretory fluxes account for up to 50% of the total sources of dissolved carbon and nutrients. Filter feeding at depth, a largely unconstrained process, could

increase this proportion by retaining sinking particles and fuelling nutrients to the dissolved pools (Steinberg et al., 2008).

In order to capture the full impact of active transport in the mesopelagic zone, it is important that zooplankton egestion and excretion be decoupled from feeding in the water column. We addressed this process by including gut passage and assimilated nutrient dynamics. The inclusion of these mechanisms increases respiratory fluxes at depth by up to 4 times compared to the case where no decoupling is considered.

These results suggest that active transport can influence the local patterns of nutrient regeneration and oxygen consumption. Due to the oxygen sensitivity of several migrating taxa (e.g. Wishner et al., 1998), changes in oxygen could in turn feedback onto the migration patterns themselves. Large predators such as fish are often characterized by low tolerance to reduced oxygen concentrations compared to migrating zooplankton (Gray et al., 2002), and daytime migration depths could be modulated in several regions by the presence of oxygen minima (Steinberg et al., 2008). The possibility that respiration by DVM organisms contributes to the formation and maintenance of oxygen minima deserves further attention.

Modeling studies have highlighted the dependence of air-sea carbon partitioning on the strength of the biological carbon pump, and on the distribution of respiratory processes in the water column (Ito and follows, 2005; Kwon et al., 2009). DVM active transport is fundamentally different from particle export in that it focuses its effect in a localized and relatively shallow region of the water column. It is important to establish the global effect of DVM-related export on the global carbon cycle, and to what extent it differs from other export mechanisms.

As an expression of upper trophic level processes, DVM is particularly susceptible to changes due to both natural and anthropogenic variability. Changes in primary productivity, temperature, oxygen content, as well as trophic-web shifts induced by fisheries, have the potential to alter the patterns of DVM. These responses should be investigated in a qualitative and quantitative way.

Fully coupled three-dimensional simulations of the ocean ecosystem and biogeochemistry including explicit or implicit representations of DVM should be used to address these questions. Our study highlights the importance of resolving processes usually overlooked in global simulations, and serves as a starting point for developing DVM parameterizations in state-of-art models of the Earth-System.

4.6 References

Al-Mutairi, H., Landry, M. R., 2001. Active export of carbon and nitrogen by diel migrant zooplankton at Station ALOHA. *Deep-Sea Research II,* 48, 2083–2103.

Andersen, V., Nival, P., 1991. A model of diel vertical migration of zooplankton based on euphausiids. *Journal of Marine Research,* 49, 153–175.

Angel, M. V., Pugh, P. R., 2000. Quantification of diel vertical migration by micronektonic taxa in the northeast Atlantic. *Hydrobiologia,* 440, 161-179.

Aksnes, D. L, Giske, J., 1993. A theoretical model of aquatic visual feeding. Ec*ological modeling,* 67, 233-250.

Aksens, D. L., Utne, A. C., 1997. A revised model of visual range in fish. *Sarsia,* 82, 137-147.

Barber, R.T., Sanderson, M.P., Lindley, S.T., Chai, F., Newton, J., Trees, C.C., Foley, D.G., Chavez, F.P., 1996. Primary productivity and its regulation in the equatorial Pacific during and following the 1991–1992 El Nin*o. Deep- Sea Research II 43 (4–6), 933–969.

Boden, B. P., and Kampa, E. M., 1967. The influence of natural light on the vertical migrations of an animal community in the sea. *Aspects of marine zoology.* Edit, by N. B. Marshall, 15-26. Academic Press, London, 270 pp.

Boyd, P. W., Gall, M. P., Silver, M. W., Bidigare, R. R., Bishop, J. K. B., 2008. Quantifying the surface–subsurface biogeochemical coupling during the VERTIGO ALOHA and K2 studies. *Deep-Sea Research II,* 55: 1594-1604.

Brix, H., Gruber, N., Karl, D. M., Bates, N. R., 2006. On the relationships between primary, net community, and export production in subtropical gyres. *Deep-Sea Research II,* 53, 698–717.

Buesseler, K. O., Boyd, P. W., 2009. Shedding light on processes that control particle export and flux attenuation in the twilight zone of the open ocean. *Limnol. Oceanogr.*, 54(4), 1210–1232.

Buesseller K. O., Andrews, J. A., Hartman, M. C., Belastock, R., Chai, F., 1995. Regional estimates of the export flux of particulate organic carbon derived from thoruium-234 during the JGOFS EqPac program. *Deep-Sea Research II*, 42, 717-804.

Buesseler, K. O., Lamborg, C. H., Boyd, P. W., Lam, P.J., Trull, T. W., Bidigare, R. R., Bishop, J. K. B., Casciotti, K. L., Dehairs, F., Elskens, M., Honda, M., Karl, D. M., Siegel, D. A., Silver, M. W., Steinberg, D. K., Valdes, J., Van Mooy, B., Wilson, S., 2007. Revisiting carbon flux through the ocean's twilight zone. *Science,* 316, 567–570.

Buesseler, K. O., Trull, T. W., Steinberg, D. K., Silver, M. W., Siegel, D.A., Saitoh, S.-I., Lamborg, C. H., Lam, P. J., Karl, D. M., Jiao, N. Z., Honda, M. C., Elskens, M., Dehairs, F., Brown, S. L., Boyd, P. W., Bishop, J. K. B., Bidigare, R. R.,

2008. VERTIGO (VERtical Transport In The Global Ocean): A study of particle sources and flux attenuation in the north pacific. *Deep-Sea Research II,* 55: 1594-1604.

Burd, A. B., Hansell, D.A., Steinberg, D. K., Anderson, T.R., Aristegui, J., Baltar, F., Beaupre, S. R., Buesseler, K. O., De Hairs, F., Jackson, G. A., Kadko, D. C., Koppelmann, R., Lampitt, R. S., Nagata, T., Reinthaler, T., Robinson, C., Robison, B. H., Tamburini, C., Tanaka, T., 2010. The imbalance between geochemical and biochemical indicators of meso- and bathypelagic biological activity: What the @#! is wrong with present calculations of carbon budgets? *Deep-Sea Res. II,* 57 (16), 1557–1571.

Cohen, J. H., Forward Jr., R. B., 2009. Zooplankton diel vertical migration: a review of proximate control. *Oceanography and Marine Biology: An Annual Review* 47, 77-110.

Dam, H. G., Zhang, X., Butler, M., Roman, M. R., 1995. Mesozooplankton grazing and metabolism at the equator in the central Pacific: Implications for carbon and nitrogen fluxes. *Deep-Sea Res. II*, 42: 735-756.

Decima, M., Landry, M. R., Rykaczewski, R., 2011. Broad-scale patterns in mesozooplankton biomass and grazing in the Eastern Equatorial Pacific. *Deep-Sea Res. II,* 58 (3–4), 387–399.

Dewar, W. K., R. J. Bingham, R. L. Iverson, D. P. Nowacek, L. C. St. Laurent, P. H. Wiebe, 2006. Does the marine biosphere mix the ocean? *Journal of Marine Research*, 64, 541–561.

Dore, J. E., Letelier, R. M., Church, M. J., Lukas, R., Karl, D. M, 2008. Summer phytoplankton blooms in the oligotrophic North Pacific Subtropical Gyre: Historical perspective and recent observations. *Progress in Oceanography,* 76, 2–38.

Elskens, M., Brion, N., Buesseler, K. O., Van Mooy, B. A. S., Boyd, P., Dehairs, F., Savoyes, N., Baeyens, W., 2008. Primary, new and export production in the NW Pacific Subarctic Gyre during the VERTIGO K2 experiments. *Deep-Sea Res. II,* 55, 1594-1604.

Geider, R. J., MacIntyre, H. L., Kana, T. M., 1997. Dynamic model of phytoplankton growth and acclimation: Response of the balanced growth rate and chlorophyll a to carbon ratio to light, nutri- ent limitation and temperature, *Mar. Ecol. Prog. Ser.,* 148, 187- 201.

Gray, J. S., Wu, R. S., Or, Y. Y., 2002. Effects of hypoxia and organic enrichment on the coastal marine environment. *Mar. Ecol. Prog. Ser*., 238, 249–279.

Gregg, M., and Horne, J. K., Turbulence, acoustic backscatter and pelagic nekton in Monterey Bay. *Journal Phys. Ocean*., 39, 1097-1114.

Griffies, S. M., Biastoch, A., Böning, C., Bryan, F., Danabasoglu, G., Chassignet, E. P., England, M. H., Gerdes, R., Haak, H., Hallberg, R. W., Hazeleger, W., Jungclaus, J., Large, W. G., Madec, G., Pirani, A., Samuels, B. L., Scheinert, M., Sen Gupta, A., Severijns, C. A., Simmons, H. L., Treguier, A. M., Winton, M., Yeager, S., Yin, J., 2009: Coordinated Ocean-ice Reference Experiments (COREs). *Ocean Modelling*, 26, 1–46.

Han, B.- P., and Straškraba, M., 1998. Modeling patterns of zooplankton diel vertical migration. *Journal of Plankton Research,* 20, 1463–1487.

Hannides, C. C. S., Landry, M.R., Benitez-Nelson, C. R., Styles, R. M., Montoya, J. P., Karl, D. M., 2009. Export stoichiometry and migrant-mediated flux of phosphorus in the North Pacific Subtropical Gyre. *Deep-Sea Research I,* 56, 73–88.

Harrison, P. J., Boyd, P. W., Varela, D. E., Takeda, S., Shiomoto, A., Odate, T., 1999. Comparison of factors controlling phytoplankton productivity in the NE and NW subarctic Pacific gyres. *Progress in Oceanography,* 43, 205–234.

Hays, G. C, 2003. A review of the adaptive significance and ecosystem consequences of zooplankton diel vertical migrations. *Hydrobiologia,* 503, 163–170.

Hernandez-Leon, S., T. Ikeda, 2008. Zooplankto respiration. In: Respiration in aquatic ecosystems, 57-82, Oxford University Press.

Heywood, K. J., 1996. Diel vertical migration of zooplankton in the Northeast Atlantic. *Journal of Plankton Research,* 18, 163–184.

Holling, C. S., 1966. The functional response of invertebrate predators to prey density. *Memoirs of the Entomological Society of Canada,* 48, 1–86.

Honda, M. C., Kawakama, H., Sasaoka, K., Watanabe, S., Dickey, T., 2006. Quick transport of primary produced organic carbon in the ocean interior. *Geophysical Research Letters,* 33, L16603.

Iriarte, J. L., Fryxell, G. A., 1995. Micro-phytoplankton at the equatorial Pacific (1401W) during the JGOFS EqPac time series studies: March to April 1992. *Deep-Sea Research II,* 42, 559–584.

Iriarte J. L. and G. A. Fryxell, 1995. Micro-phytoplankton at the equatorial Pacific (140ºW) during the JGOFS EqPac times series studies: March-April and October 1992. *Deep-Sea Research II*, 42, 559-584.

Jiang, S., Dickey, T. D., Steinberg, D. K., Madin, L. P., 2007. Temporal variability of zooplankton biomass from ADCP backscatter time series data at the Bermuda Testbed Mooring site. *Deep-Sea Research I,* 54, 608–636.

Karl, D. M., Christian, J. R., Dore, J. E., Hebel, D. V., Letelier, R. M., Tupas, L. M., Winn, C. D., 1996. Seasonal and interannual variability in primary production and particle flux at Station ALOHA. *Deep-Sea Research II,* 43, 539–568.

Kessler, W. S., Mc Phaden ,M. J., 1995. The 1991–1993 El Nino in the central Pacific. *Deep-Sea Research II,* 42, 295–333.

Lampert, W., 1989. The Adaptive Significance of Diel Vertical Migration of Zooplankton. Functional Ecology, 3, 21-27.

Landry, M. R., Al-Mutairi, H., Selph, K. E., Christensen, S., Nunnery, S., 2001. Seasonal patterns of mesozooplankton abundance and biomass at Station ALOHA. *Deep-Sea Research II,* 48 (8–9), 2037–2061.

Lindley S. T., Bidigare, R. R., Barber, R. T., 1995. Phytoplankton photosynthesis parameters along 140ºW in the equatorial Pacific. *Deep-Sea Research II,* 42.

Longhurst, A. R., Harrison, W.G., 1988. Vertical nitrogen flux from the oceanic photic zone by diel migrant zooplankton and nekton. *Deep-Sea Research I,* 35, 881–889.

Longhurst, A.R., and Harrison, W.G., 1988. Vertical nitrogen flux from the oceanic photic zone by diel migrant zooplankton and nekton. *Deep-Sea Research I,* 35, 881–889.

Luo, J., Ortner, P. B., Forcucci, D., Cummings, S. R., 2000. Diel vertical migration of zooplankton and mesopelagic fish in the Arabian Sea. *Deep-Sea Research Part II,* 47 (7–8), 1451–1473.

Mackas, D., Bohrer, R., 1976. Fluorescence analysis of zooplankton gut contents and an investigation of diel feeding patterns. *J. exp. mar. Biol. Ecol.*, 25, 77-85.

Morrison, J. M., Codispoti, L. A., Smith, S. L., Wishner, K., Flagg, C., Gardner, W. D., Gaurin, S., Naqvi, S. W. A., Manghnani, V., Prosperie, L., and Gundersen, J. S.,

1999. The oxygen minimum zone in the Arabian Sea during 1995, *Deep Sea Res. II* 46, 1903–1931.

Murray, J. W., Johnson, E., Garside, C., 1995. A US JGOFS process study in the equatorial Pacific (EqPac): introduction. *Deep-Sea Research II,* 42, 275–293.

O'Brien, T. D., Murphy, P. P., Conkright, M. E., Boyer, T. P., Antonov, J. I., Baranova, O. K., Garcia, H. E., Gelfeld, R., Johnson, D., Locarnini, R. A., Smolyar, I., Stephens, C., 2002. World Ocean Database 2001, Volume 7: Temporal Distribution of Chlorophyll and Plankton Data. S. Levitus, Ed., NOAA Atlas NESDIS 48, U.S. Government Printing Office, Wash., D.C., 219 pp., CD-ROMs.

Pennington, J. T., Mahoney, K. L., Kuwahara, V. S., Kolber, D. D., Calienes, R., Chavez, F.P., 2006. Primary production in the eastern tropical Pacific: a review. *Progress in Oceanography,* 69 (2–4), 285–317.

Postel L., da Silva, A. J., Mohrholz, V., Lass, H.- U., 2007. Zooplankton biomass variability off Angola and Namibia investigated by a lowered ADCP and net sampling. *Journal of Marine Systems,* 68, 143–166.

Richards, S. A., Possingham, H. P., Noye, J. 1996. Diel vertical migration: modelling light-mediated mechanisms. *Journal of Plankton Research,* 18, 2199–2222.

Roe, H. S. J., Badcock, M. V. J., Domanski, P., James, P. T., Pugh, P. R., Thurston, M. H., 1984. The Diel Migrations and Distributions within a Mesopelagic Community in the North East Atlantic. *Prog. Oceanog.,* 13, 245-268.

Robinson, C., Steinberg, D. K., Anderson, T. R., Aristegui, J., Carlson, C. A., Frost, J. R., Ghiglione, J.- F., Hernandez-Leon, S., Jackson, G. A., Koppelmann, R., Queguiner, B., Ragueneau, O., Rassoulzadegan, F., Robison, B. H., Tamburini, C., Tanaka, T., Wishner, K. F., Zhang, J., 2010. Mesopelagic zone ecology and biogeochemistry – a synthesis. Deep-*Sea Research II,* 57: 1504-1518.

Roman, M. R., Dam, H. G., Gauzens, A. L., Urban-Rich, J., Foley, D. G., Dickey, T. D., 1995. Zooplankton variability on the equator at 140ºW during the JGOFS EQPAC study. *Deep Sea Research, Part II*, 42: 673-693.

Saltzman, J., Wishner, K. F., 1997. Zooplankton ecology in the eastern tropical Pacific oxygen minimum zone above a seamount: 1. General trends. D*eep-Sea Research I,* 44, 907–930.

Sørnes, T. A., D. L. Aksnes, 2004. Predation efficiency in visual and tactile zooplanktivores. *Limnol. Oceanogr.*, 49(1), 2004, 69–75.

Steinberg, D. K, Carlson, C. A., Bates, N. R., Goldthwait, S. A., Madin, L. P., Michaels, A. F., 2000. Zooplankton vertical migration and the active transport of dissolved organic and inorganic carbon in the Sargasso Sea. *Deep-Sea Res. I,* 47: 137–158.

Steinberg, D. K., Cope, J. S., Wilson, S. E., Kobari, T., 2008. A comparison of mesopelagic zooplankton community structure in the subtropical and subarctic Pacific Ocean. *Deep-Sea Research II,* 55: 1594-1604.

Stock, C., J. P. Dunne, 2010. Controls on the ratio of mesozooplankton production to primary production in marine ecosystems. *Deep-Sea Research I,* 57 (2010) 95–112.

Taylor A. G., M. R. Landry, K. E. Selph, E. J. Yang, 2011. Biomass, size structure and depth distributions of the microbial community in the eastern equatorial Pacific. *Deep-Sea Research II,* 58, 342–357.

Torres, J. J., and Childress, J. J. 1983. Relationship of oxygen consumption to swimming speed in Euphausia pacifica. 1. Effects of temperature and pressure. *Marine Biology*, 74, 79–86.

Wishner, K., Gowingb, M. M., Gelfmana, C. 1998. Mesozooplankton biomass in the upper 1000 m in the Arabian Sea: overall seasonal and geographic patterns, and relationship to oxygen gradients. *Deep Sea Research II,* 45, 2405-2432.

Table 4.1: Parameters controlling the processes associated with DVM in the model. See sections 4.2.2, 4.2.3 and 4.2.4 for details.

Symbol	Description	Value	Reference
irr^{DVM}	Preferred isolume	$10^{-5}\ W\ m^{-2}$	*(1,2)*
w^{swim}	Migration velocity	$3\ \mathrm{cm\,s^{-1}}$	*(3,4,5)*
K_v^{bio}	Zooplankton biological diffusion	$10^{-1}\ m^2\ s^{-1}$	*(6)*
k^{clear}	Gut clearance rate	$3\ \mathrm{h^{-1}}$	*(7)*
k^{metab}	Assimilated pool utilization rate	$24\ \mathrm{h^{-1}}$	*(8)*
w^{ref}	Reference velocity to scale the costs of swimming	$7\ \mathrm{cm\,s^{-1}}$	*(9)*
α^v	Visual predation fraction	0.9	*(9)*
K_{irr}	Half saturation response for light limitation	$10^{-2}\ \mathrm{W\,m^{-2}}$	*(9)*

(1) Boden and Kampa, (1967); (2) Roe, (1983); (3) Heywood, (1996); (4) Morrison et al., (1999); (5) Luo et al., (2000); (6) see section 4.2.2; (7) Mackas and Bohrer, (1976); (8) Hernandez-Leon and Ikeda (2008); (9) relatively unconstrained parameters, see the discussion in sections 4.2.2 and 4.2.3, and the sensitivity analyses in section 4.2.

Table 4.2: Ecosystem diagnostics for the three model implementation sites. For each site the first column shows observational values, the second column model results. The variables shown are: Z_{EUPH}=euphotic zone depth, NPP=net primary production, CHL=chlorophyll, SP+LP=total phytoplankton biomass, LP:SP+LP=fraction of large phytoplankton, C:CHL=Carbon to chlorophyll ratio, SZ=microzooplankton biomass, LZ+LMZ=mesozooplankton biomass, LMZ:LZ+LMZ=fraction of diel vertical migrating mesozooplantkon, POC FLUX=particulate organic carbon export from the euphotic zone, PE-RATIO=ratio between POC export and NPP at the base of the euphotic zone. Values are integral over the euphotic zone.

	K2		ALOHA		EQPAC	
Z_{EUPH} (m)	37 *(1)* 48-58 *(2)*	75	100-125 *(2,13)*	111	95 *(17)*	96
NPP ($mmolC\,m^{-2}d^{-1}$)	25-40 *(3,4)* 30-44 *(5,23)* 63 *(6)* 19-167 *(2)*	37	15-18 *(13,23)* 14 *(14)* 28 *(3)*	22	72 ± 8 *(18)* 95 ± 7 *(19)* 77 ± 27 *(20)* 108 *(23)*	67
CHL ($mg\,m^{-2}$)	25-28 *(3,7)* 29 ± 3 *(1)*	39	14-16 *(7)* 6-12 *(14)*	13	24 *(7)* 24 ± 6 *(17)* 22 *(20)*	23
SP+LP ($mmolC\,m^{-2}$)	~80-145 *(8,9)*	180	110 *(15)* ~90 *(8)*	74	114 ± 25 *(17)* 164 ± 36 *(20)* ~130 *(8)*	117
LP:SP+LP	< 0.4 *(10)* >0.25 *(11)*	0.36	~0.2 *(2,11)*	0.23	0.26 *(11)* 0.19 ± 0.7 *(17)*	0.19
C:CHL	60 *(11)*	55	~70 *(11)*	69	64 ± 15 *(17)*	62
SZ ($mmolC\,m^{-2}$)	-	61	-	39	31 ± 10 *(17)*	44
LZ+LMZ ($mmolC\,m^{-2}$)	150 *(12)*	153	25-29.5 *(12, 16)*	25	83 ± 7 *(21)*	76
LMZ:LZ+LMZ	0.6 *(12)*	0.61	~0.4 *(12,16)*	0.30	0.4 *(21)*	0.67
POC FLUX ($mmolC\,m^{-2}d^{-1}$)	3.3-11.1 *(13,23)*	8.5	1.8-2.0 *(13)* 1.0 *(14)* 1.3 *(23)*	1.4	3-5 *(22)* 2.2 *(23)*	4.8
PE-RATIO	0.11-0.25 *(13, 23)*	0.23	0.11-0.13 *(13)* 0.07 *(14, 23)*	0.06	0.05-0.10 *(22)* 0.02 *(23)*	0.07

(1) Harrison et al. (1999). Summertime euphotic zone depth and chlorophyll in the Western Subarctic Gyre of the Pacific Ocean.

(2) Boyd et al. (2008). Euphotic zone depths defined by NPP > 0. K2 productivity is the annual range in the WSG from several studies. LP:LP+SP values between 0.1 and 0.3 at ALOHA are taken from Figure 1.

(3) Dunne et al. (2007). Annual means from satellite based estimates. Values at K2 assume a euphotic zone depth of 55 m for integrated chlorophyll.

(4) Honda et al. (2006). Annual mean NPP from satellite based estimates.

(5) Elsksens et al. (2008). NPP values after a summer bloom at K2.

(6) Shiomoto et al. (1998). Summertime NPP for the Western Subarctic Gyre of the Pacific Ocean.

(7) Annual average chlorophyll concentrations from WOA01 (O'Brien et al., 2001) integrated over the euphotic zone.

(8) Biomasses estimates from the annual mean Chl, assuming an average Chl:C of 60 (Stock and Dunne 2010, supplementary information).

(9) The lower value is calculated from the SP biomass estimate from Zhan et al. (2008), 55 $mmol C\, m^{-2}$, assuming LP:LP+SP fraction equal to 0.3 (references 10 and 11).

(10) Liu et al. (2004): fraction of SP (picophytoplankton) from a compilation of studies for the WSG. Note that nanoplankton contributes substantially – therefore SP fraction could be larger than accounted by picophytoplankton alone.

(11) Stock and Dunne (2010), supplementary information. The LP:LP+SP fraction from line P in the eastern subarctic gyre is reported instead of K2. This is likely to be an underestimate for K2.

(12) Steinberg et al. (2008). Total mesozooplankton biomass (size > 330 μm) from 0-150 m at night. Migratory fraction was estimated from night-day biomass difference.

(13) Buesseler et al. (2007). Two summer surveys at both K2 and ALOHA. At K2 one survey follows a summertime bloom.

(14) Brix et al. (2006). Annual climatological NPP and clorophyll.

(15) Karl et al. (2001). The study reports total phytoplanktonic biomass. Partitioning between LP and SP is estimated assuming 20% of biomass is in the LP size range (references 2, 11).

(16) Al-Mutahiri and Landry (2001). Mesozooplankton biomass in the upper 150 m. DVM fraction increases to more than 0.6 for size classes larger than 2000 μm.

(17) Taylor et al., (2011). Chlorophyll and biomasses integrated over the euphotic zone. SP includes both nano and picophytoplankton. SZ includes all heterotrophic flagellates and ciliates.

(18) Landry et al. (2011). Biomasses averaged between 4ºN-4ºS, 110ºW-140ºW from two 2004-2005 cruises.

(19) Barber et al. (1996). NPP between 1ºS and 1ºN from two 1992 surveys during and after a major El Nino event.

(20) Chavez et al. (1996). NPP average between 5ºS-5ºN from two 1992 surveys between 95ºW-170ºW. Photosynthetic biomass and chlorophyll are the average of climatological values and the two 1992 surveys, assuming a euphotic zone depth of 110 m.

(21) Decima et al. (2011). Total mesozooplankton biomass (size > 500 μm) in the euphotic zone. The migratory fraction is estimated as night-day difference.

(22) Buesseler et al. (1995). POC fluxes at the equator from two 1992 surveys. Values decrease to approximately 2 mmolC/m2/d for the region between 4ºN-4ºS.

(23) Buesseler and Boyd (2009). Compilation and review of existing estimates of NPP and POC fluxes.

Table 4.3: Net primary production (NPP), net community production (NCP), POC flux from the euphotic zone, export due to DVM, export due to other processes, *e-ratio* (NCP/NPP), *pe-ratio* (POC FLUX/NPP), *dvm-ratio* (DVM flux/NPP) and *dom-ratio* (Non-sinking biomass export/NPP). Units for production and fluxes are $mmol C\, m^{-2} d^{-1}$.

	K2	ALOHA	EQPAC
NPP	36.7	22.4	67.5
NCP	14.6	1.9	7.0
POC flux	8.5	1.4	4.7
DVM flux	2.7	0.2	1.9
DOM fluxes	3.4	0.3	0.4
e-ratio	0.39	0.09	0.10
pe-ratio	0.23	0.06	0.07
dvm-ratio	0.07	0.01	0.03
dom-ratio	0.09	0.01	0.01

Table 4.4: Ratio between DVM and POC exports at 150 m depth. 1st row: model without the internal pool dynamics; 2nd row: model with gut pool dynamics only; 3d row: model with metabolic pool dynamics only; 4th row: model with both gut and metabolic pool dynamics; 5th row: model with both gut and metabolic pool dynamics and with migrating zooplankton fraction forced to match observations (see Table 1).

	K2	ALOHA	EQPAC
No internal dynamics	0.08	0.07	0.16
Gut pool dynamics only	0.29	0.15	0.34
Metabolic pool dynamics only	0.19	0.13	0.34
Control runs - Gut and metabolic pool dynamics	0.31	0.17	0.44
Prescribed migrating fraction	0.38	0.22	0.18

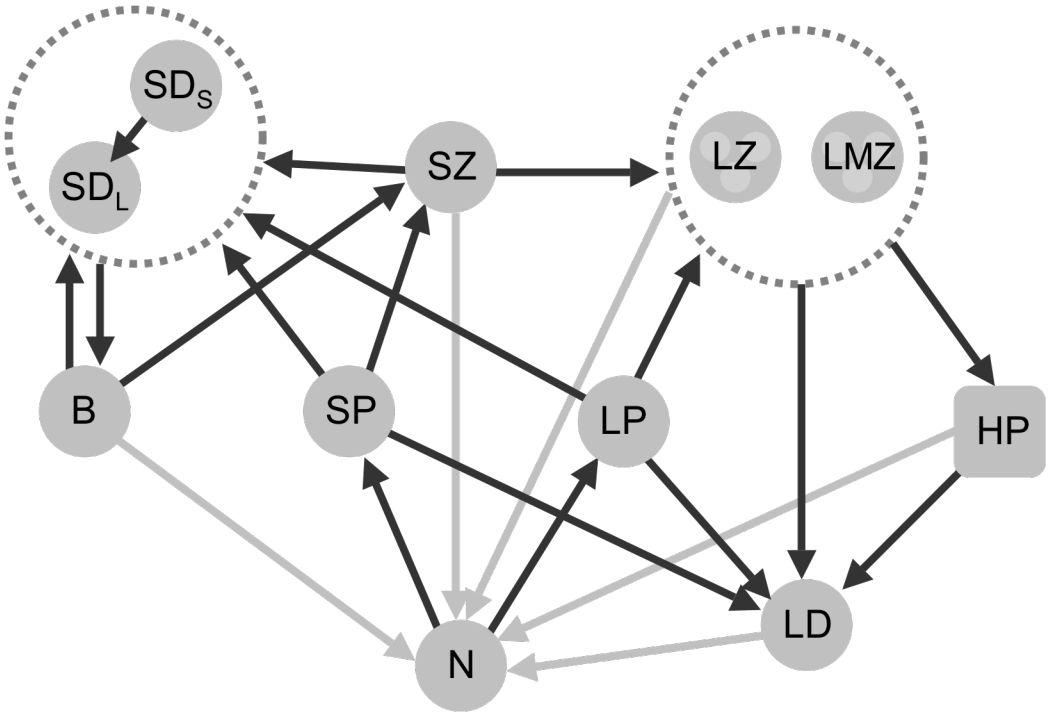


Figure 4.1: Ecosystem model structure. There are 10 main state variables (grey circles): SP= small phytoplankton, LP=large phytoplankton, SZ=small zooplankton, LZ=large zooplankton, LMZ= large migrating zooplankton, B=bacteria, SD_L=labile small detritus, SD_S=semilabile small detritus, N=limiting nutrient. HP=higher order predators that are not resolved explicitly. The dashed circle around small detritus components represents the combine small detrital pool. The circle around large zooplankton components rapresents the combined large zooplankton pool. Both LZ and LMZ groups are composed by three internal pools as described in section 4.2.3, and schematized in Figure 4.2. Adapted from Stock and Dunne (2010).

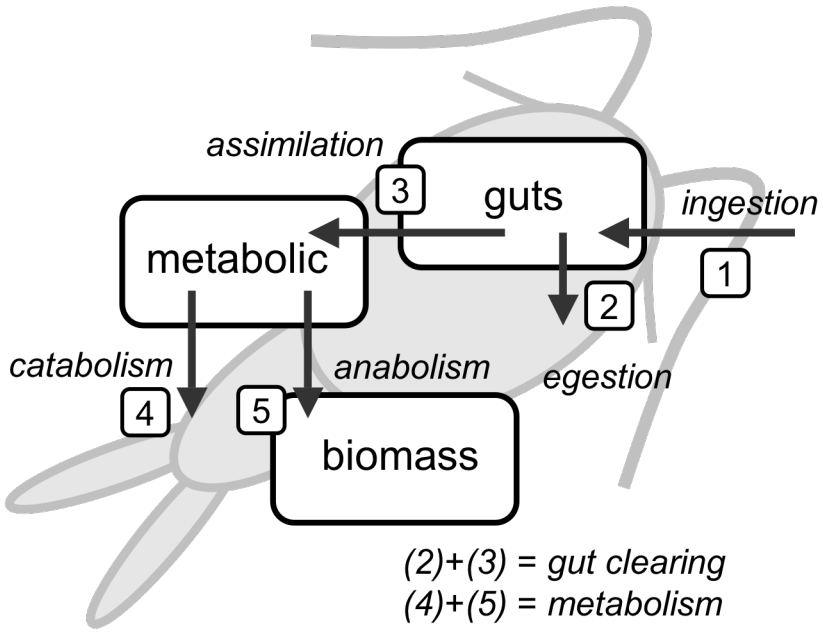


Figure 4.2: Schematic of the three nutrient pools (rectangles) that compose large zooplankton (LZ) and vertically migrating zooplankton (LMZ) biomass, and the metabolic pathways that connect them (arrows). The numbers correspond to the following metabolic pathways: (1) ingestion, (2) egestion, (3) assimilation, (4) catabolism and (5) anabolism. See section 2.3 for details on the formulation of these fluxes

.

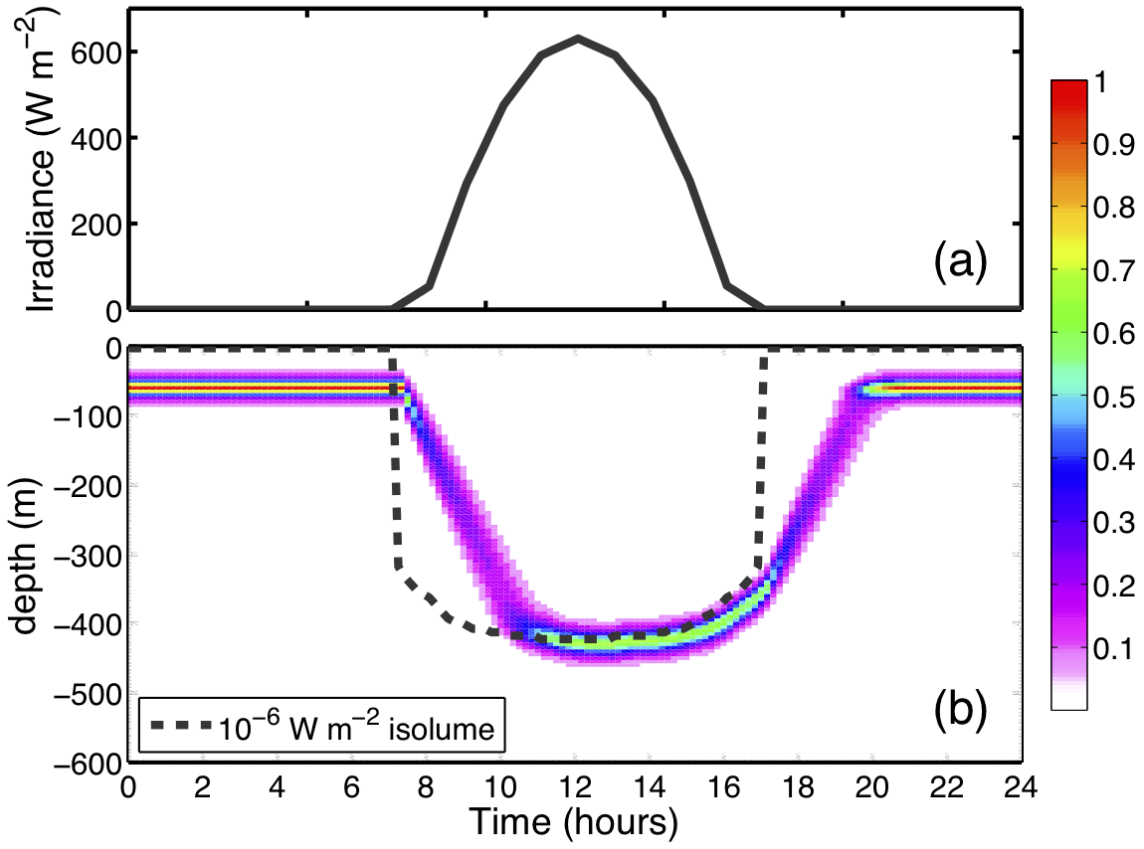


Figure 4.3: Example of (a) daily cycle in surface irradiance and (b) large migrating zooplankton (LMZ, colour) and depth of the $10^{-5}\,\mathrm{W m^{-2}}$ isolume (dot-dashed black line). Irradiance and model output are shown for January at station ALOHA in the subtropical Pacific Ocean (158°W, 22.5°). LMZ biomass has been rescaled between 0 and 1 for plotting reasons.

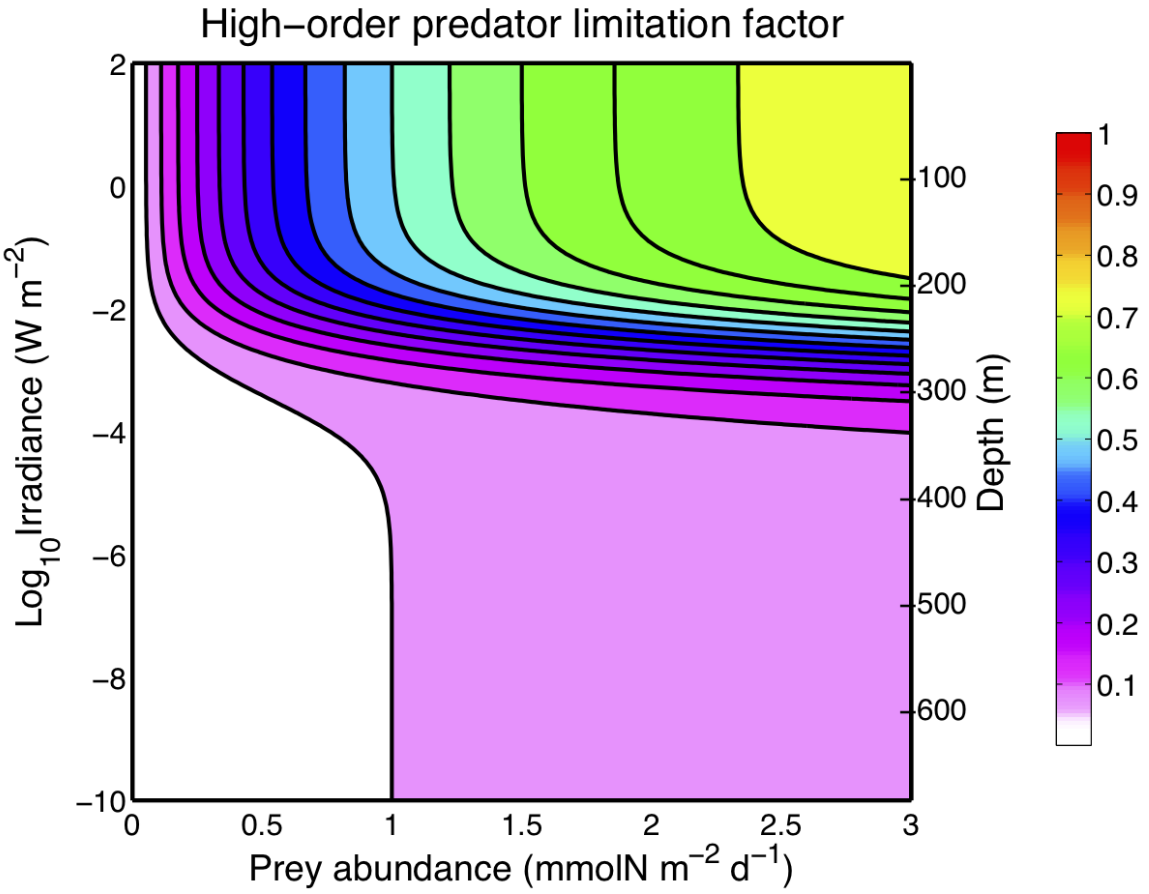


Figure 4.4: Light-dependent limitation factor for the ingestion rate of high order predators (f_{HP}^{Z}). The x-axis shows prey concentration ($\mathrm{mmolN\,m^{-3}}$). The left y-axis shows the local irradiance ($\mathrm{W\,m^{-2}}$). On the the right y-axis we converted the local irradiance to equivalent depth, assuming a surface irradiance of 200 $\mathrm{W\,m^{-2}}$ and water column conditions for the subtropical Pacific Ocean. The parameters used for the plot are: $K_Z = 1.0\ \mathrm{mmolN\,m^{-3}}$, $K_{irr} = 10^{-2}\ \mathrm{W\,m^{-2}}$, $\alpha^v = 0.9$. See section 2.4 for details.

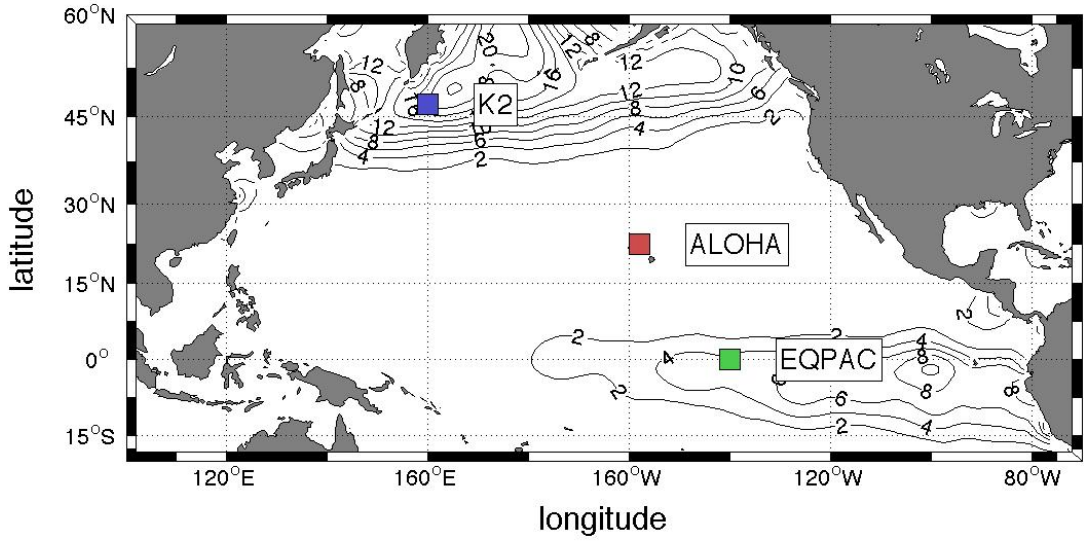


Figure 4.5: Locations of model implementation. Station coordinates are: K2, 161°E, 47°N; ALOHA, 158°W, 22.5°; EQPAC, 140°W, 0°N. Contours show mean surface nitrate concentration from the World Ocean Atlas.

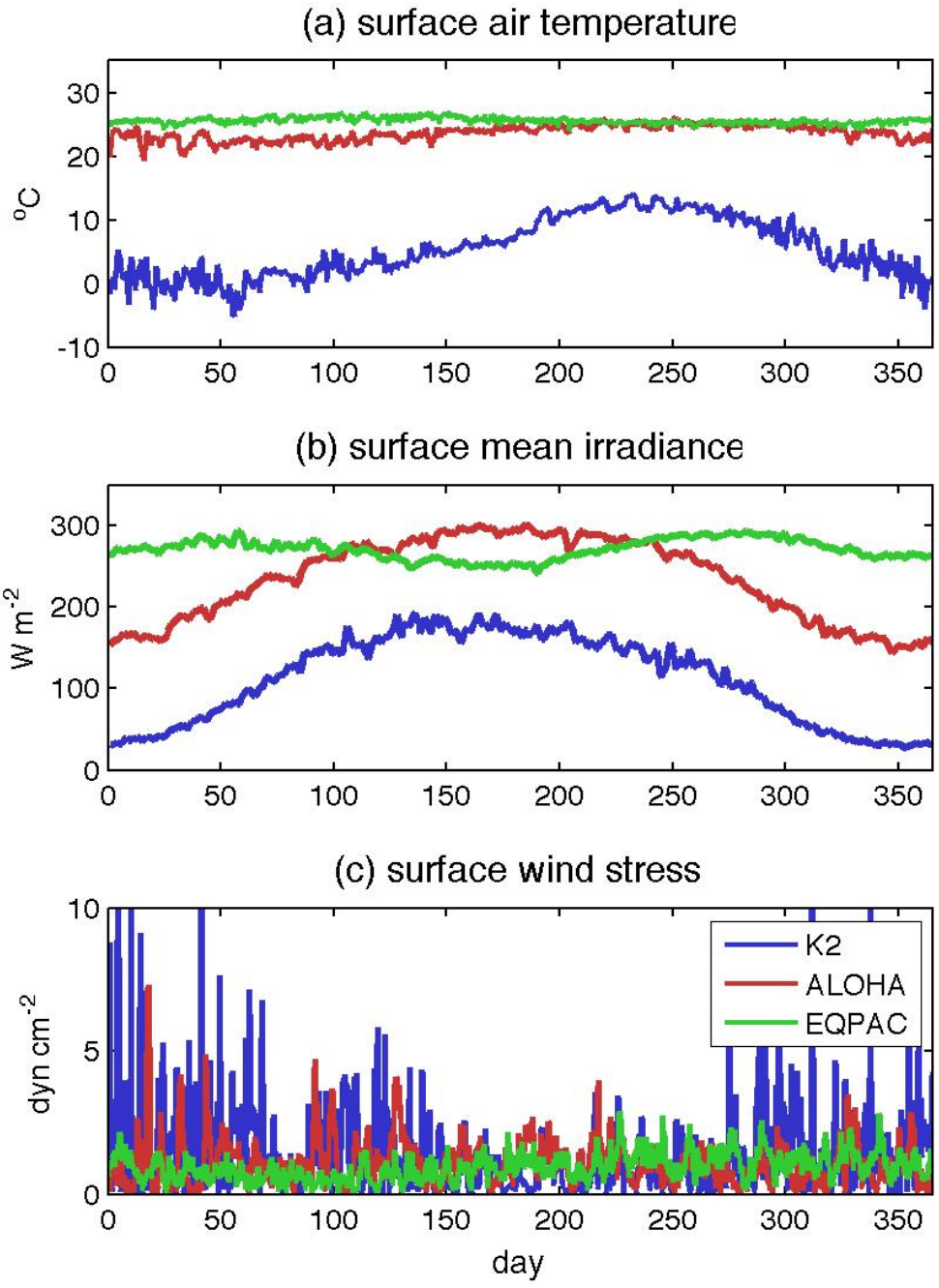


Figure 4.6: Surface forcings for the three locations of model implementations. (a) Surface air temperature (ºC); (b) daily mean shortwave irradiance at the surface ($W\ m^{-2}$); (c) surface wind stress ($dyn\ cm^{-2}$).

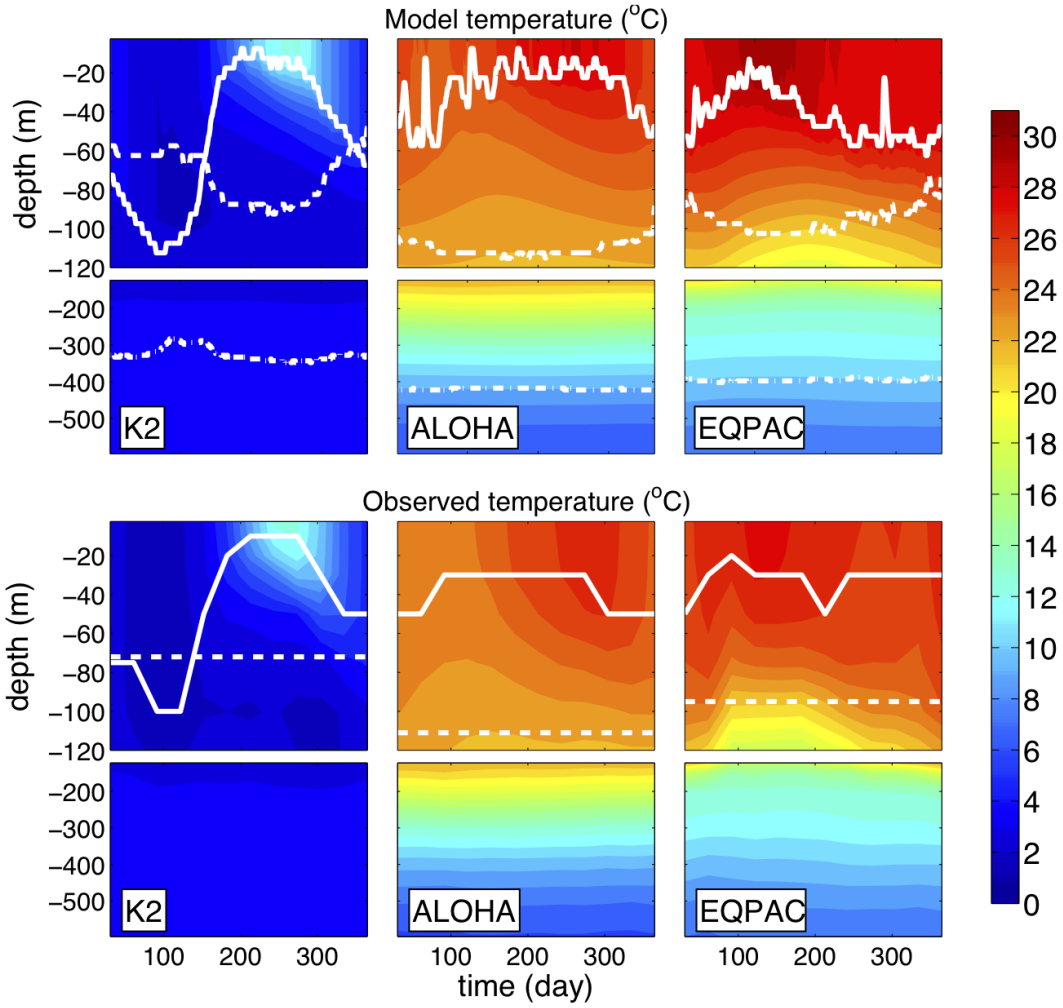


Figure 4.7: Upper panel: modeled annual cycle of temperature (colour), mixed layer depth (solid white line), euphotic zone depth (dashed white line), and depth of the $10^{-5}\,\mathrm{W\,m^{-2}}$ isolume (dot-dashed white line) for the three locations of model implementation. Lower panel: climatological annual cycle of temperature (colour) and mixed layer depth (solid white line) from the World Ocean Atlas, and mean euphotic zone depth (see Table 1 for references). Mixed layer depths are calculated with a 0.125 $\mathrm{kg\,m^{-3}}$ density difference criterion

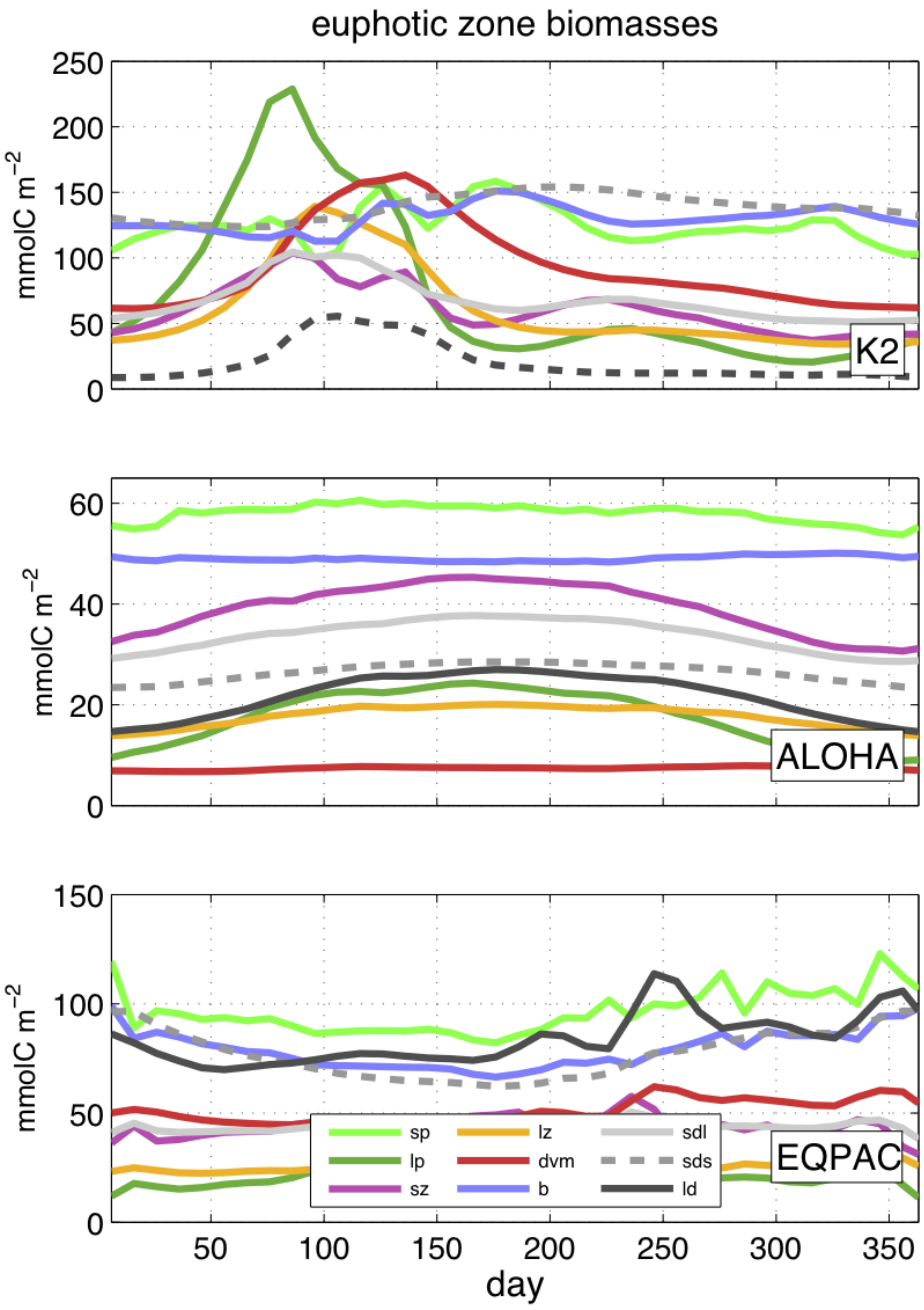


Figure 4.8: Annual cycle of vertically integrated biomasses (0 - 600 m) for the three model locations. Biomasses have been converted to carbon units using a stoichiometric ratio of 106/16. Detritus biomasses indicated with a dashed line have been scaled to 10% of the original value to fit in the figure.

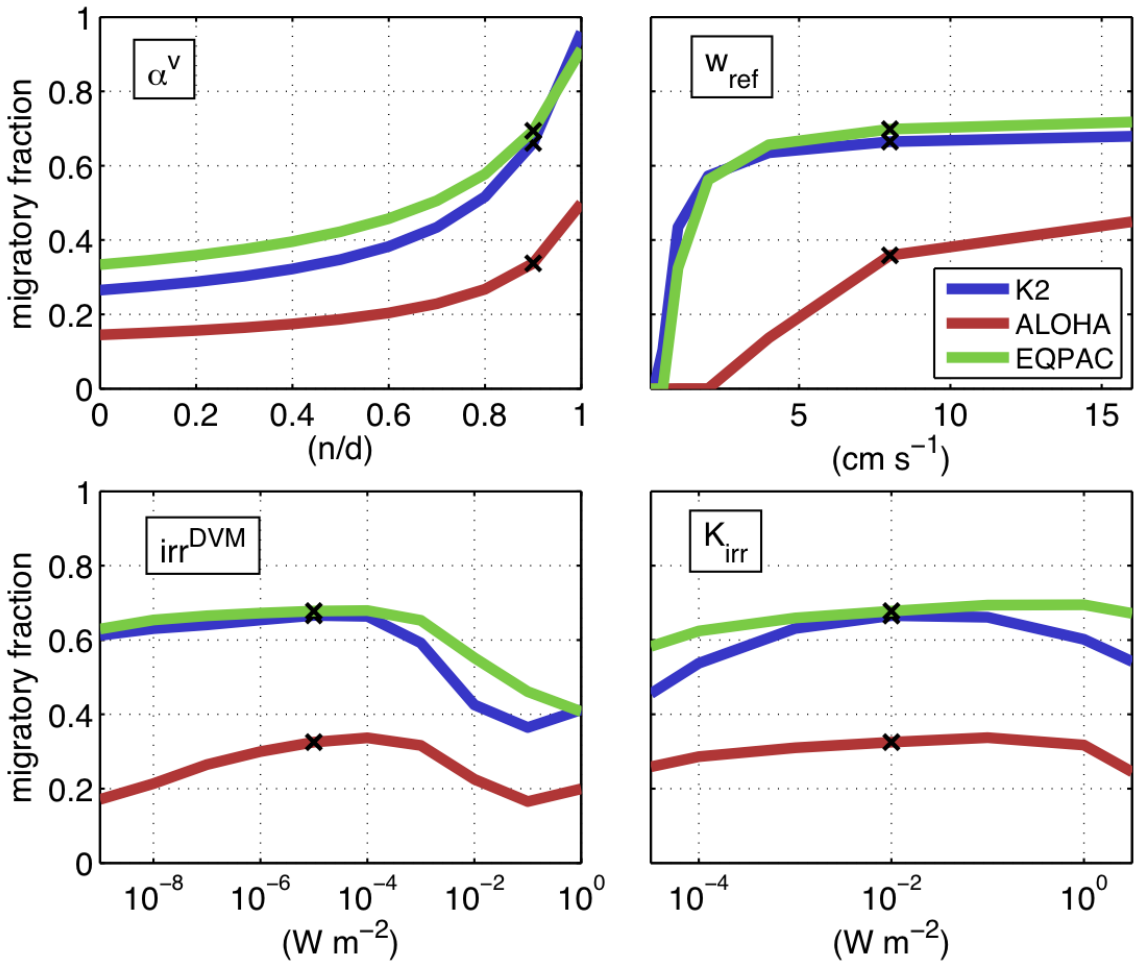


Figure 4.9: Sensitivity of the fraction of migrating zooplankton LMZ/(LMZ+LZ) to parameters controlling visual predation and DVM. Crosses indicate the values of the control runs. The parameters are: α^{v}, visual predation fraction; w^{ref}, velocity scale controlling the cost of swimming; irr^{DVM} preferred isolume, K_{irr}, half saturation constant for the light response of visual predators. See sections 2.2-2.4 for details.

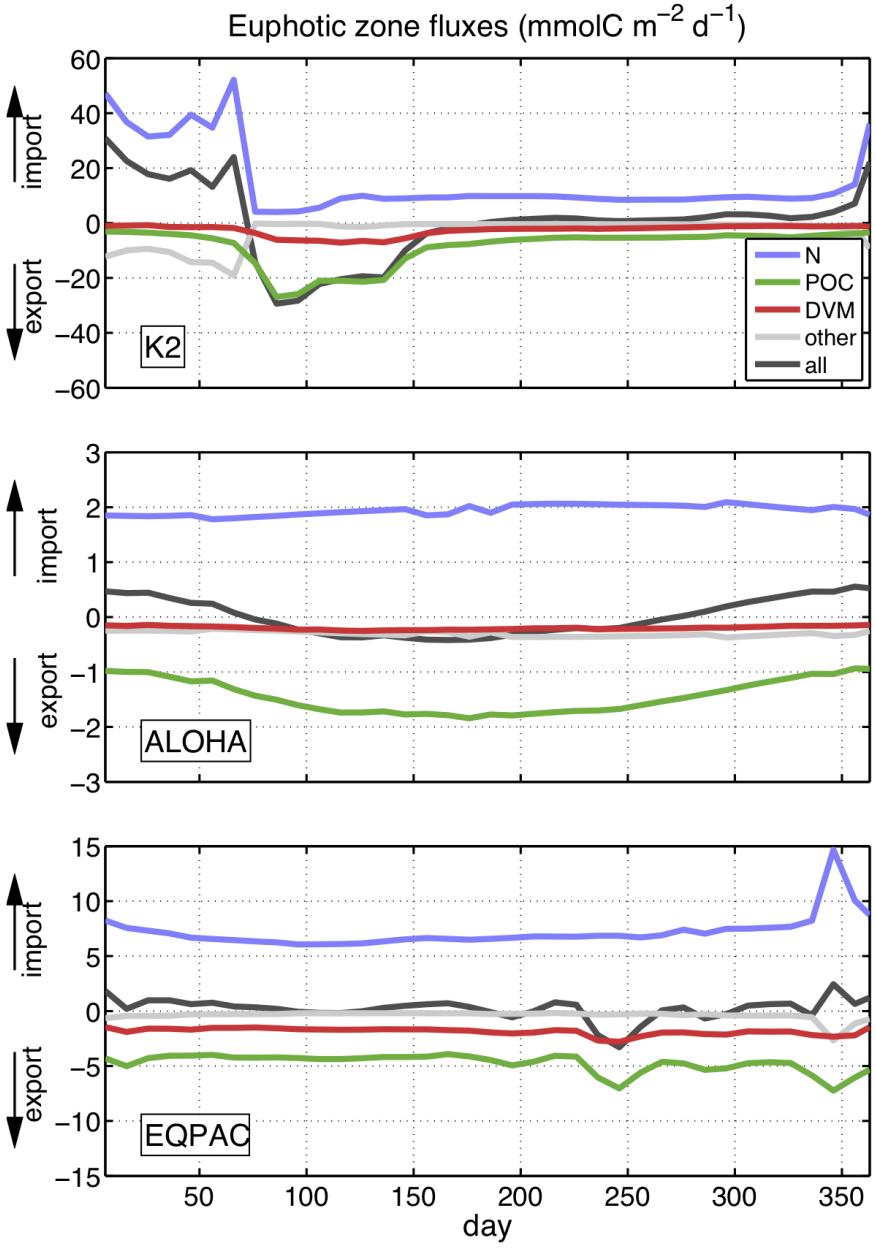


Figure 4.10: Annual cycle of carbon fluxes ($\mathrm{mmol\,C\,m^{-2}d^{-1}}$) into the euphotic zone. Positive numbers indicate imports to the euphotic zone, negative number exports. Blue: N import due to physical processes and nutrient restoring, converted to carbon units by using a stoichiometric ratio equal to 106/16. Green: large sinking detritus (LD) export. Red: export due to DVM of large zooplankton (LMZ). Grey: all other sources of export, including downward diffusion of biomass for other functional groups. Black: net import/exports.

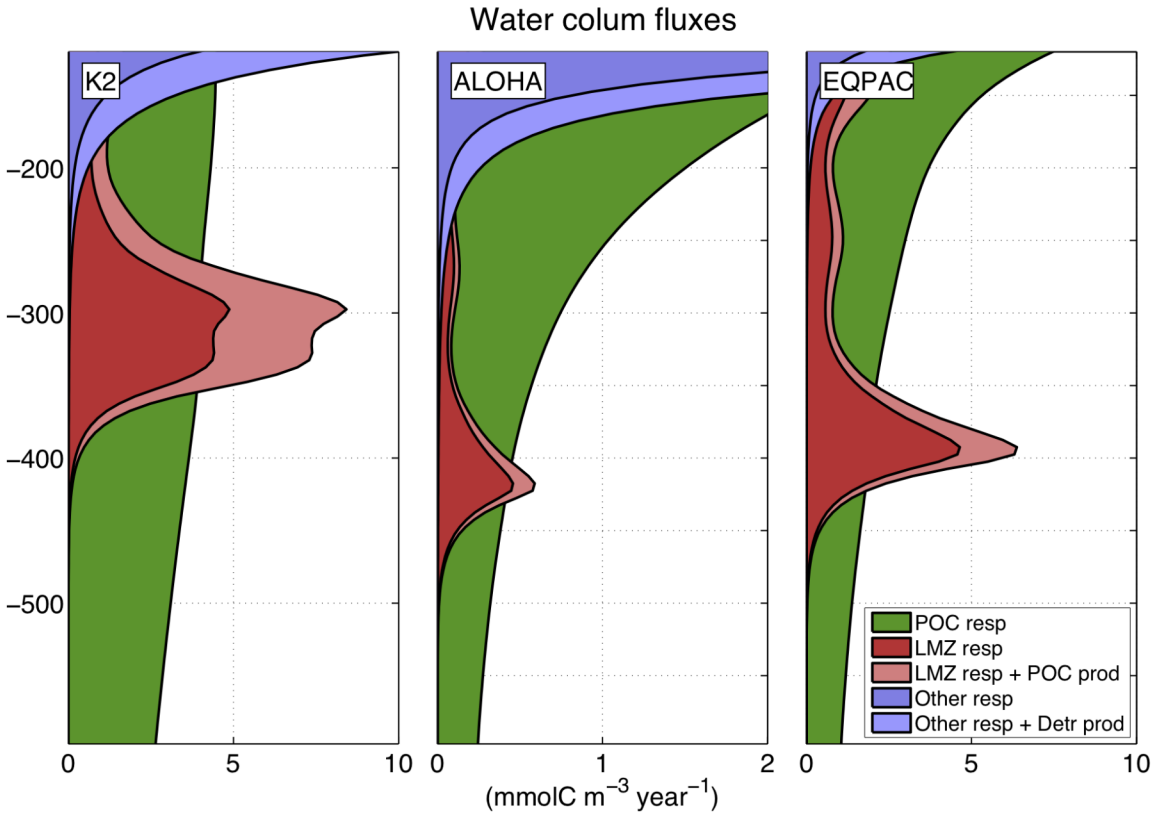


Figure 4.11: Annual mean respiratory/excretory fluxes and detritus production ($\mathrm{mmol\,C\,m^{-3}year^{-1}}$) in the mesopelagic zone. The green curve shows detritus respiration. The red curves show fluxes from the migrating zooplankton pool (LMZ) to the dissolved nutrient and small detritus (dark red) and large detritus (light red) pools. The blue curves show fluxes from all other state variables to the dissolved and small detritus (dark blue) and large detritus (light blue) pools.